Scaling Dispersion Processes in Surcharged Manholes

Shing-Tak Douglas Lau

This thesis is submitted in partial fulfilment of the requirements for the Degree of Doctor of Philosophy

University of Sheffield

Department of Civil and Structural Engineering

December 2007

THESIS CONTAINS

VIDEO

CD

DVD

TAPE CASSETTE

DECLARATION

I declare that the work in this thesis has been composed by myself and no portion of the work has been submitted in support of an application for another degree or qualification of this or any other university or other institute of learning. The work has been my own except where indicated and all quotations have been distinguished by quotation marks and the sources of information have been acknowledged.

Scaling Dispersion Processes in Surcharged Manholes

Shing-Tak Douglas Lau

ABSTRACT

Urban drainage network models are increasingly used in the water industry for hydraulic and water quality simulation. These models require inputs for energy loss and mixing coefficients to make predictions of head loss and the transport of solutes or dissolved substances across hydraulic structures, such as sewer pipes and manholes. Laboratory-derived head loss and mixing coefficients for manholes may be used in urban drainage modelling. However, the applicability of the laboratory-scale derived parameters to full scale structures in the urban drainage system, i.e. scalability of these parameters, is not clearly understood.

The overall aim of the research is to derive generic scaling methodologies to describe the impact of physical scale of manholes on the hydraulic and mixing processes using laboratory- and CFD-based analyses.

A 1:3.67 scale model of an 800 mm internal diameter manhole (the prototype) studied by Guymer et al. (2005) has been constructed in the laboratory. Laboratory experiments were conducted to measure head loss and solute dispersion in the scale model. The solute dispersion results were analysed using advection dispersion equation (ADE) and aggregated dead zone (ADZ) models and comparisons of the results with the prototype experimental data were made. The cumulative temporal concentration profiles (CTCPs) for the scale model were also compared with the prototype profiles. However, analysis of the laboratory-derived data failed to quantitatively identify the scale effects because the recorded data of the two manholes was not directly comparable.

Computational fluid dynamics (CFD) was used to investigate the effects of scale in the surcharged manhole. A thorough validation study was conducted to provide confidence in the CFD model predictions. A standard modelling protocol for manhole simulations was developed through the validation study.

Three differently sized manholes were created using CFD. The scale effects on the flow field, energy loss and solute transport characteristics were investigated. The findings of the study suggest that scale effects exist in the three manholes; however, the degree of the effects is very small. The scale effects were attributable to the dissimilarity in Reynolds number and that led to different characteristic of the jet in the manhole. Methodologies to scale the hydraulic and solute transport processes in surcharged manholes have been presented.

DEDICATION

This thesis is dedicated to the memory of my grandmother.

ACKNOWLEDGEMENTS

TABLE OF CONTENTS

LIST OF FIGURES

xii

xvi

LIST OF TABLES

NOTATION

Roman

A	cross sectional area
A_t	storage zone cross sectional area
B	mass balance ratio
$\bar{c}$	time average concentration
C	concentration
C_d	downstream concentration
C_L	time scale constant
C_t	storage zone solute concentration
C_u	upstream concentration
d_p	particle diameter
D	manhole internal diameter
D_p	upstream pipe internal diameter or manhole delivery pipe internal diameter
D_n	nozzle diameter
e_m	molecular mass diffusivity
e_{ti}	turbulent mass diffusivity in the i direction
F_D	drag force
F_t	fluorescence at t °C
F_x	other forces such as Brownian force
Fr	Froude number
g	gravitational acceleration
h	width of the scanning light sheet
k	turbulent kinetic energy
K	longitudinal dispersion coefficient
K_L	energy loss coefficient
K_s	storage exchange coefficient
K_{sp}	energy loss coefficient of a smooth pipe
l	length scale
L_e	eddy length scale
p	static pressure
Q	discharge
r	pipe radius
Re	Reynolds number
Re_p	Reynolds number of a particle
s	surcharge
S	surcharge ratio
Sc_t	turbulent Schmidt number
$\overline{S_{ij}}$	main strain rate
t	time
t_c	solution temperature

t_n	volumetric travel time i.e. volume over discharge
$\bar{t}$	travel time
$\bar{t_i}$	time at the centroid of the tracer at profile i
T	residence time
T_L	fluid Lagrangian integral time
u	fluid velocity
u_p	particle velocity
u'	fluid fluctuating velocity
u^*	shear velocity
U	mean velocity of a flow
U_o	velocity in the jet core
V	volume
X	distance
ΔH	head loss across manhole
Δp	water level difference between manometers

Greek

α	ADZ parameter, describe dispersion
χ	integration time
δ	ADZ parameter, describe advection
ε	turbulent dissipation rate
γ	a measure of pipe friction
η	Kolmogorov length scale
λ_L	length scale factor
λ_Q	discharge scale factor
μ	dynamic viscosity of a fluid
μ_t	turbulent or eddy viscosity
ν	kinematic viscosity of a fluid
ν_t	turbulent kinematic viscosity
θ	turbulent velocity scale
ρ	fluid density
ρ_p	density of a particle
σ^2	temporal variance of a profile
τ	reach time delay
τ_p	particle relaxation time
τ_e	characteristic lifetime of eddy
$\tau_{xx, uu, zz}$	Reynolds normal stresses
$\tau_{xy, uz, xz}$	Reynolds shear stresses
υ	Kolmogorov time scale

ABBREVIATIONS

ADE	Advection Diffusion Equation
ADZ	Aggregated Dead Zone
CFD	Computational Fluid Dynamics
CHP	Central Horizontal Plane
CRTD	Cumulative Retention Time Distribution
CSO	Combined Sewer Overflow
CTCP	Cumulative Temporal Concentration Profile
CVP	Central Vertical Plane
DF	Dispersive Fraction
DNS	Direct Numerical Simulation
ID	Internal Diameter
LES	Large Eddy Simulation
LIF	Laser Induced Fluorescence
LVP	Left Vertical Plane
MSHP	Mid-Surcharge Horizontal Plane
NS	Navier Stokes
OD	Outer Diameter
OTIS	One-Dimensional Transport with Inflow and Storage Model
PIV	Particle Image Velocimetry
RANS	Reynolds Averaged Navier Stokes
RNG	Renormalisation Group
RSM	Reynolds Stress Model
RTD	Retention Time Distribution
RVP	Right Vertical Plane
TCP	Temporal Concentration Profile

1 Introduction

1.1 Background

Urban areas generally make use of underground sewer systems to collect wastewater and sometimes surface runoff. The systems convey the sewage downstream for treatment or disposal to natural watercourses after primary treatment. A complete sewer system generally consists of pipe networks, manholes, combined sewer overflows (CSOs), online or offline storage tanks and a wastewater treatment plant. All of these components work as a whole and form a complex network system.

Greater environmental concern and the need to improve the effectiveness of urban drainage networks have led to the use of numerical models. These models attempt to describe the operation and response, to any proposed change, of both the contributing system and receiving environment. The consequence of accidental spillages, intermittent discharges and time-dependent changes in the concentration of pollutants in the networks can also be predicted by these models. Using the predicted results, measures can be undertaken to reduce the amount of pollution to the natural environment. Mark *et al.* (1998) provided examples of practical applications of these numerical models.

Commercial computational analysis software, such as the US EPA's (United States Environmental Protection Agency) Storm Water Management Model (SWMM), Hydroworks (now InfoWorks) (Herath *et al.*, 1999) and MOUSE TRAP (DHI, 2000), has been developed for modelling complex urban drainage networks. Urban drainage network models are increasingly used in the current water industry for hydraulic and water quality simulation. The models employ fundamental hydraulic theory and water quality models to predict pressure loss and the transport process of sediments or soluble pollutants.

Urban drainage models require inputs for energy loss coefficients and mixing parameters (such as travel time and dispersion parameters) to make predictions of head loss and the transport of solutes or dissolved substances across hydraulic structures, such as sewer pipes and manholes. The estimation of energy loss and mixing coefficients for sewer pipes may be straightforward, as they are a function of friction and shear effects (Guymer *et al.*, 2005). Extensive laboratory-based research has been conducted on the head loss and mixing at surcharged manholes and a wide range of geometrical configurations has been studied, such as manholes with different 'manhole diameter to pipe diameter' ratios; step manholes and manholes with pipe direction change (Bo Pederson and Mark, 1990; Dennis, 2000; Guymer *et al.*, 2005; Howarth and Saul,

1984; Lindvall, 1984; Saiyudthong, 2004). Coefficient values for energy loss and mixing were derived from these laboratory-scale models and they could potentially be used in urban drainage modelling.

However, there is some uncertainty regarding the applicability of laboratory-scale derived coefficients to full scale structures in the urban drainage system. At present, the scalability of these coefficients for manholes is not clearly understood. The results obtained from the laboratory-based experiments may not truly represent the real behaviour of the full scale structures due to possible scale effects. The aim of this study is therefore to investigate the impact of physical scale on the hydraulic and solute transport characteristics at surcharged manholes. Laboratory- and computational fluid dynamic (CFD)-based studies are used for the investigation.

CFD is increasingly used in the water industry. It has a significant benefit over laboratory-based studies in that once a numerical model has been validated it may be used to examine the impact of changes to the geometry or flowrate with comparative ease. The numerical technique has been adopted to simulate the flow and transport of solutes or sediments through a variety of urban drainage structures, including manholes (Asztely and Lyngfelt, 1996; Dennis, 2000), storage tanks (Stovin, 1996), sewer grit traps (Buxton, 2003) and CSOs (Harwood, 1999). However, there is a lack of validation case data corresponding to manhole simulations. This study therefore collects new experimental flow field and tracer data to validate the CFD manhole models, and proposes a modelling protocol for manhole simulations.

1.2 Aims and Objectives

The overall aim of the research is to derive generic scaling methodologies to describe the impact of physical scale of manholes on the hydraulic and mixing processes using laboratory- and CFD-based analyses. This research work was undertaken based on an 800 mm internal diameter (ID) manhole studied by Guymer *et al.* (2005). A scale model of the 800 mm ID manhole (prototype) was constructed in the laboratory as well as studied in CFD. A standard modelling protocol for manhole simulations was developed based on the validation of the scale manhole CFD models.

To achieve the overall aim of the research, the following objectives were defined:

- Investigate the scale effects on the mixing characteristics by collecting a new set of laboratory tracer data from the scale manhole model and comparing the new dataset with the recorded data of the prototype (laboratory-based study);

- Establish a standard modelling protocol for manhole simulations through thorough parametric studies for CFD model set-up parameters and rigorous validation of the flow field and solute transport predictions; flow field validation data is collected from flow visualisation experiments;

- Examine the scale effects through studying the hydraulic and solute transport characteristics of a number of virtual manhole models at different scales (one configuration) created using the standard modelling procedure established in the previous stage (CFD-based study).

1.3 Structure of the Thesis

The thesis comprises eight chapters. Chapter 1 (this chapter) is the introduction to the thesis describing the background, aims and objectives of the research.

In Chapter 2, a review of the relevant literature and theory is presented. The review covers fundamental hydraulic principles (Section 2.2) and a general overview of sewerage systems in the UK (Section 2.3). The concept of longitudinal dispersion and the governing equations for solute transport models, with specific reference to the advection dispersion equation (ADE) and aggregated dead zone (ADZ) model, are introduced in Section 2.4. A review of previous manhole research is provided in Section 2.5. Section 2.6 outlines the governing equations for flow field and solute transport models used in the CFD-based study. The numerical techniques for solving these numerical equations and previous applications of CFD in modelling hydraulic structures are also considered in Section 2.6. Section 2.7 discusses the measurement techniques considered in the laboratory experiments of this research.

Chapter 3 describes the laboratory configurations and instrumentation used in the laboratory experiments for the scale manhole model. The chapter also highlights the methodology of data collection and data analysis for the pressure measurements and dye traces collected in the laboratory work. Further data analysis of the dye traces using the ADE and ADZ models and interpretation of the results are covered in Chapter 4. Comparisons of the derived model parameters and the temporal concentration profiles between the scale manhole and the prototype model are made to analyse the scale effects.

The laboratory flow visualisation experiments for the scale manhole model using the laser induced fluorescence (LIF) and particle image velocimetry (PIV) techniques are highlighted in Chapter 5. The methodology of the experiments and the associated data analysis are introduced.

The feasibility and detailed study of CFD manhole simulations are considered in Chapter 6. The feasibility study examines the possibility of using CFD to replicate the flow field and solute transport characteristics in manholes (Section 6.2). In the detailed CFD simulation study (Section 6.3), parametric tests for grid density, spatial discretisation scheme, turbulence model and solute transport model are undertaken. The validation of the flow field and solute transport predictions for the manhole models against the measured data is also highlighted in Section 6.3. The standard modelling procedure for manhole simulations is presented in Section 6.4.

Chapter 7 describes the generation of the virtual manhole models and investigates the scale effects on flow field, energy loss and solute transport characteristics. Methodologies for scaling flow field, energy loss and mixing processes in surcharged manholes are also proposed.

The overall conclusions of the study and suggestions for further work are presented in Chapter 8.

2 Literature Review and Theory
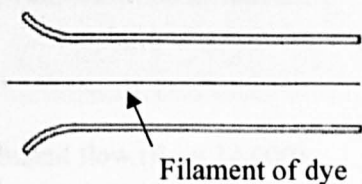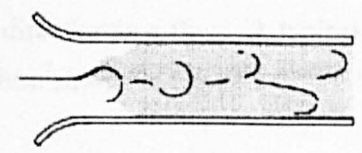
2.1 Introduction

The aim of this chapter is to review the literature and theory relevant to this research. Section 2.2 introduces fundamental hydraulic principles; Section 2.3 presents a brief introduction to sewerage systems in the UK. The concept of longitudinal dispersion and the governing equations for solute transport models, with specific reference to the advection dispersion equation (ADE) and aggregated dead zone (ADZ) models, are highlighted in Section 2.4. Previous research on head loss and mixing across surcharged manholes is reviewed in Section 2.5. The computational fluid dynamics (CFD) technique, which has been used in this study to model the flow and mixing within manholes, is highlighted in Section 2.6. In Section 2.7, the experimental techniques employed in this study are introduced; and a summary is presented in the last section.

2.2 Fundamental Hydraulic Principles

2.2.1 Laminar and Turbulent Flows

The distinction between laminar and turbulent flows was shown scientifically by Reynolds in 1883. Reynolds designed an experiment in which a filament of dye was injected into a flow of water. The flow of water passed through a glass tube so that observations could be made. Reynolds discovered three distinct phases of flow as discharge increased:

1. Laminar flow (very low discharge)	- The fluid may be considered to flow in discrete layers and in an orderly manner with no mixing	

Filament of dye

2. Transitional flow	- Some degree of unsteadiness becomes apparent

3. Turbulent flow (very high discharge)	- The fluid incorporates an eddying or mixing action and is characterised by continuous fluctuations in velocity and direction

Reynolds's experiments revealed that the onset of turbulence was a function of fluid velocity, viscosity and a typical length scale. This led to the formation of the dimensionless Reynolds number (Re), which represents the ratio of inertia force of a fluid over fluid viscosity:

$$Re = \frac{\rho u l}{\mu} = \frac{u l}{v}$$ 2.1

where:

l	is a length scale
u	is the fluid velocity
μ	is the dynamic viscosity of the fluid, $= v / \rho$
ρ	is the fluid density

The onset of turbulence tends to occur within a predictable range of Re values (Chadwick and Morfett, 1998). For example, in pipe flows, when the pipe diameter is used as the length scale, laminar flows normally exist when the Re value is smaller than 2,000 (Figure 2.1a); transitional flows exist in the range of Re values between 2,000 and 4,000; and turbulent flows are normally found when the Re value is greater than 4,000 (Figure 2.1b). Note that these values should be regarded as a rough guide because in some experiments, laminar flows have been detected for a Re value greater than 4,000.
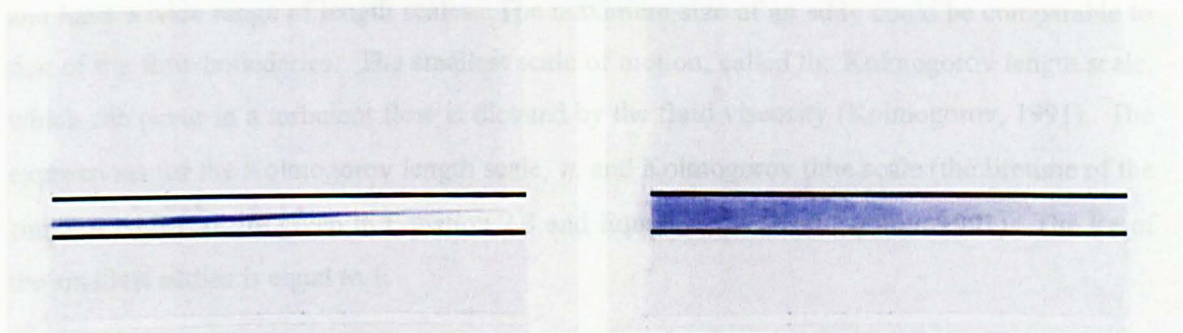
(a) – Laminar flow (Re = 470)   (b) – Turbulent flow (Re = 14,000)

Figure 2.1 – Laminar and turbulent flows in a pipe

2.2.1.1 General Description of Turbulent Flows

Laminar flows may be visualised as a purely frictional action between adjacent fluid layers (Figure 2.1a). In turbulent flows, this orderly behaviour breaks down due to the existence of turbulent eddies which cause random fluctuations in velocity and direction in a flow. A typical point velocity measurement in a turbulent flow might exhibit the form shown in Figure 2.2.
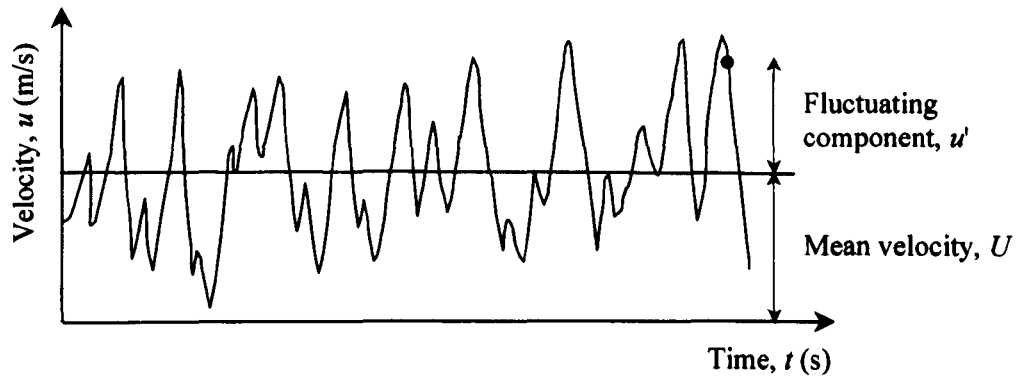
Figure 2.2 – A typical one point measurement from a turbulent flow

The time series profile of the one point velocity measurement shows that the velocity randomly fluctuates about the mean velocity of a flow. The velocity in Figure 2.2, $u(t)$, can be decomposed into a steady mean value, U, with a fluctuating component $u'(t)$, and expressed in the form below:

$$u(t) = U + u'(t)$$ 2.2

The nature of turbulence is demonstrated by rotational flow structures. These structures, called turbulent eddies, are characterised by a length scale and time scale, referred to as the eddy characteristic size and the eddy lifetime respectively. Turbulent eddies are three-dimensional and have a wide range of length scales. The maximum size of an eddy could be comparable to that of the flow boundaries. The smallest scale of motion, called the Kolmogorov length scale, which can occur in a turbulent flow is dictated by the fluid viscosity (Kolmogorov, 1991). The expressions for the Kolmogorov length scale, η, and Kolmogorov time scale (the lifetime of the smallest eddy), υ, are given in Equation 2.3 and Equation 2.4 (Kolmogorov, 1991). The Re of the smallest eddies is equal to 1.

$$\eta = \left(\frac{v^3}{\varepsilon} \right)^{0.25}$$ 2.3

$$\upsilon = (v\varepsilon)^{0.25}$$ 2.4

where:

ε is the turbulent dissipation rate

v is the kinematic viscosity of the fluid

The generation and dissipation of turbulent eddies involves the following processes: the largest turbulent eddies interact with and extract energy from the mean flow by a process called vortex stretching. The larger scale eddies then break down to smaller eddies and the angular momentum of the larger eddies is transferred to smaller eddies. The energy transfer process,

called the energy cascade, continues until the viscous forces become dominant. Work is performed against the action of viscous stresses, so the energy associated with the rotational motion of the smallest eddies is dissipated and converted into thermal internal energy, i.e. energy loss.

The structure of the largest eddies is highly anisotropic (directional) and flow-dependent due to their strong interactions with the mean flow. At high mean flow Reynolds numbers, the smallest eddies in a turbulent flow are isotropic due to the action of viscosity. This concept is important in the development of turbulence models, as described in Section 2.6.4.

2.2.2 Froude Number

Froude number (Fr), derived by Froude in 1868, is a non-dimensional group that describes the relationship between the inertial force of a fluid and the gravitational force exerted on the fluid (Equation 2.5). The physical significance of Fr in water engineering arises from the fact that it also represents the ratio of water velocity over the wave velocity of the fluid.

$$Fr = \frac{u}{\sqrt{gl}}$$
2.5

where:

l is a length scale

g is the gravitational acceleration

u is the fluid velocity

In open channel flows, Fr is used to define the regime of the flow, either sub-critical or super-critical. Sub-critical flows occur when Fr is smaller than 1; and super-critical flows exist when Fr is greater than 1. When Fr is close to one, the flow conditions tend to become unstable, resulting in wave formations. Since a complete description of open channel flow is beyond the scope of this research, further details may be found in Chadwick and Morfett (1998). Fr is introduced here because it was used as the principles of scaling for the manholes studied.

2.3 Sewerage Systems

A sewerage system refers to a whole infrastructure system including pipes, manholes, pumping stations, combined sewer overflows (CSOs), online or offline storage tanks and so on (Butler and Davies, 2000). The system is designed for the conveyance of surface runoff and wastewater, from its point of origin, to wastewater treatment works (WwTWs) or natural watercourses after primary treatment. In the UK, two types of conventional sewerage system are commonly implemented in urban areas. They are combined systems, in which wastewater and stormwater

flows are carried in the same pipe or network; and separate systems, in which the two types of flow are kept in separate pipes or networks. A hybrid system, i.e. a partially separate system, is also common in the UK.

Combined systems were historically used for urban drainage in UK cities. During dry weather, the system carries only foul sewage from industrial and domestic sources. In the event of a storm, the flow in the system increases dramatically in response to the addition of stormwater. Increasing urbanisation, which is associated with increased levels of impermeable surface, results in a high volume of surface runoff going into the drainage system during storms. This leads to two technical problems in this type of sewerage system. It is not economically feasible to provide capacity for the maximum flow during storm events in the whole pipe network, as only a small proportion of the capacity is used most of the time. It is also not possible to provide capacity in WwTWs to treat all the sewage during storms. To prevent internal flooding from these combined systems due to insufficient capacity in the network and WwTWs, CSOs were introduced to divert excessive flows (overflows) directly to a natural watercourse. It was anticipated that overflows would occur in times of rainfall and that the overflowing sewage would be sufficiently diluted with clean surface water before it was discharged to a natural watercourse. However, storm flows can be highly polluted, especially early in the storm when the increased flow flushes the sewers. This has led to unsatisfactory discharges from CSOs which introduce detrimental effects on the water quality of the receiving watercourse. A schematic plan of a combined sewerage system is provided in Figure 2.3.
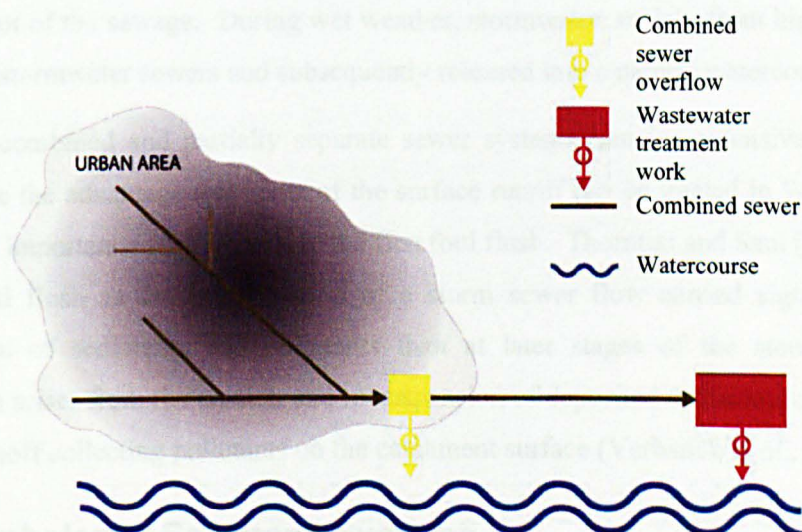
Figure 2.3 – Typical layout of a combined sewerage system (after Butler and Davies, 2000)

Most of the sewerage systems that have been constructed in the UK since 1945 comprise separate sewers (Butler and Davies, 2000). The concept of this system is to convey foul and

stormwater flows using separate pipes such that foul sewage is treated in WwTWs at all times and stormwater, which should not be mixed with wastewater, is discharged to a watercourse at a convenient point (Figure 2.4). The immediate advantage of this system over combined system is the absence of CSO. However, this concept may be too ideal in reality because perfect separation of the flows is not possible. Firstly, there is no guarantee that polluted flow is only carried in wastewater pipes. Urban storm runoff is generally contaminated to some degree. Secondly, rainfall can possibly infiltrate into wastewater pipes.
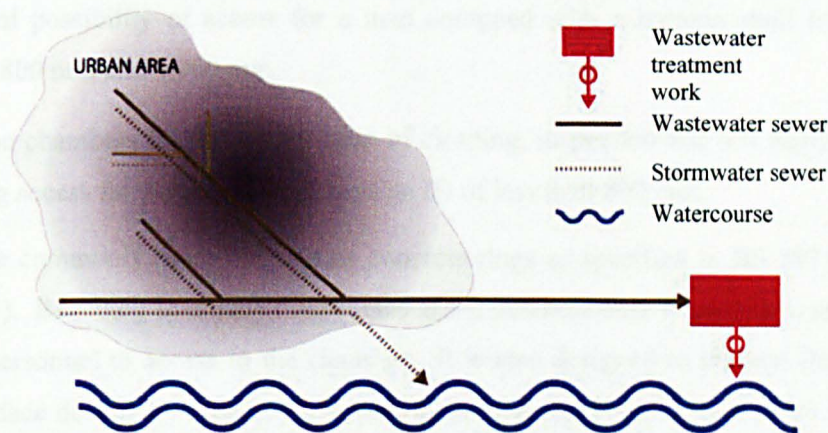
Figure 2.4 – Typical layout of a separate sewerage system (after Butler and Davies, 2000)

A partially separate sewerage system operates in a similar fashion to a combined system. The surface runoff from household (roofs and gardens) is conveyed in wastewater sewers to promote the movement of the sewage. During wet weather, stormwater, mainly from highway drainage, is carried in stormwater sewers and subsequently released into a natural watercourse.

The use of combined and partially separate sewer systems remains extensive. In fact, such systems have the advantage that some of the surface runoff can be treated in WwTWs. This is of particular importance with regards to the first foul flush. Thornton and Saul (1986) described the first foul flush as the initial period of a storm sewer flow carried significantly higher concentration of sediments and pollutants than at later stages of the storm event. This phenomenon arises from the erosion and re-suspension of deposited sediments on the sewer bed and from runoff collecting pollutants on the catchment surface (Verbanck *et al.*, 1994).

2.3.1 Manholes in Sewerage Systems

Manholes are a major component of sewerage systems. They are provided at changes in flow direction, pipe slope, diameter and elevation; at major junctions with other sewers and every 90 m (BS EN 752-3:1997). The primary function of a manhole is to allow human access to the sewer for the purposes of inspection, cleaning, maintenance and repair. The size and shape of a

manhole are dependent upon these functions in association with the construction materials and local geography. BS EN 476:1997 provides some guidelines for the nominal dimensions of a manhole or inspection chamber:

- Manholes for all maintenance works with access for personnel shall have an internal diameter (ID) of 1,000 mm or greater, or a nominal size for rectangular sections of 750 mm x 1,200 mm

- Manholes for the introduction of cleaning equipment, inspection and test equipment with occasional possibility of access for a man equipped with a harness shall have an ID of between 800 mm and 1,000 mm.

- Inspection chambers for the introduction of cleaning, inspection and test equipment but not providing access for personnel shall have an ID of less than 800 mm.

Manholes are commonly made of pre-cast concrete rings as specified in BS 5911 (Butler and Davies, 2000). Benching is usually constructed at the manhole base to provide a secure and flat surface for personnel to access to the chamber. It is also designed to prevent flooding on the benching surface during dry weather flow conditions and deposition of sediments and solids on the surface. A typical sewer manhole is illustrated in Figure 2.5a.

In situations where a high level sewer is connected to a lower level sewer, it is more economical to construct drop manhole or back-drop manhole than increasing the gradient of the incoming drain (Woolley, 1988). A drop manhole incorporates a vertical drop within the manhole and a ramp in the benching is provided to guide the sewage flow from a higher level sewer to a lower sewer. According to BS 8301:1985, drop manholes shall be used when the difference in the invert level between the sewers is smaller than 0.68 m. Otherwise, a backdrop manhole should be considered. It consists of a vertical shaft placed close to the outside of the manhole wall, connecting the two sewers (Figure 2.5b). This construction design protects personnel entering the chamber and eliminates nuisance created by solids splashed onto the walls (Hammer, 2003).

(a) – Sewer manhole (b) – Backdrop manhole
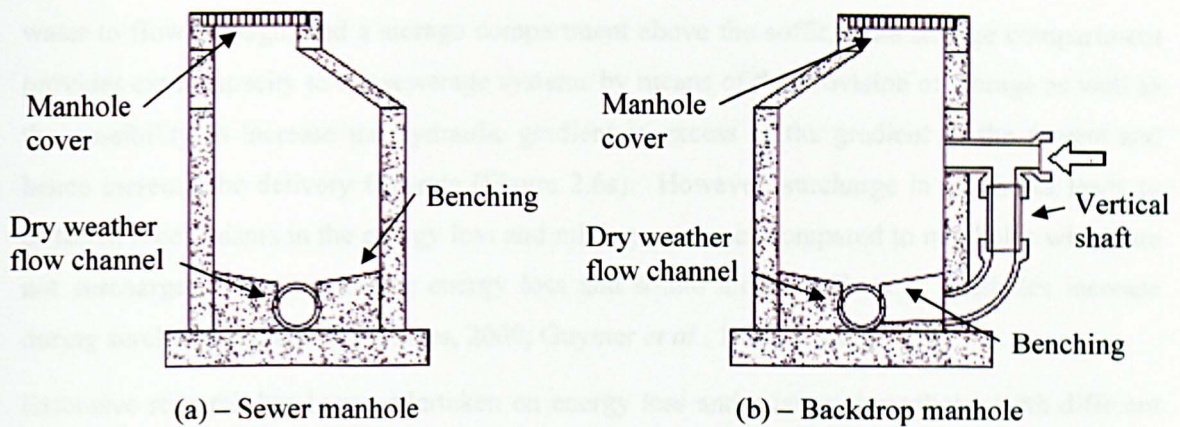
Figure 2.5 – Typical Manholes

2.3.1.1 Surcharge in Manholes

Sewerage systems operate under surcharged conditions, i.e. pipe-full flows under pressurised conditions, relatively frequently. This is because the design return periods of storms used for their design are short, such as one year, and in some storm events, the amount of sewage, exceeds the designed capacity of the sewerage systems (Archer *et al.*, 1978). Reed (1983) suggested two possibilities in which the sewerage systems would become surcharged (Figure 2.6). It occurs when the discharge along the pipe is greater than the just-full capacity at the pipe gradient (Figure 2.6a); or when the downstream drainage component imposes a backwater effect (Figure 2.6b).
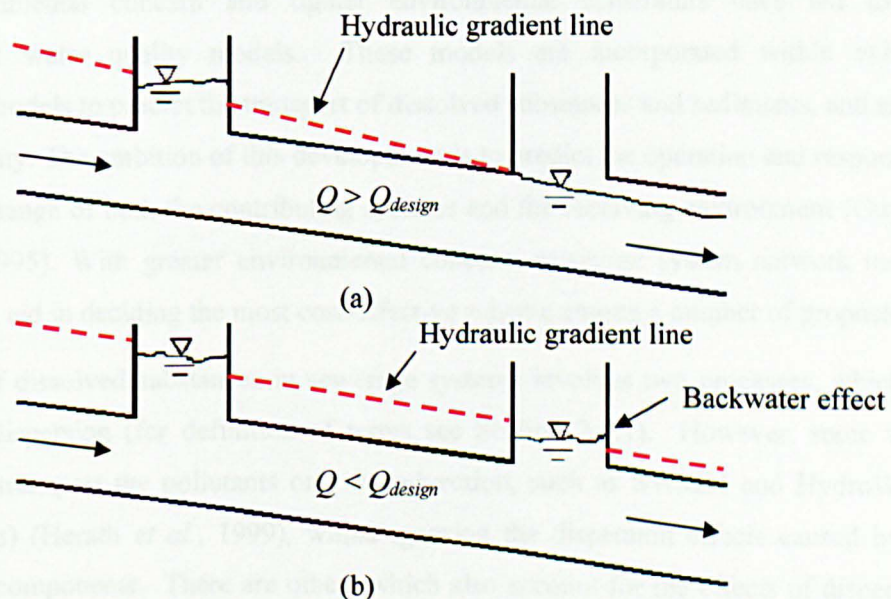
Figure 2.6 – Conditions leading to surcharge in sewerage systems (after Reed, 1983)

During surcharged conditions, the water level in the manhole rises above the soffit level of the inlet sewer. A surcharged manhole can be seen to comprise two portions: a portion that allows

water to flow through; and a storage compartment above the soffit. The storage compartment provides extra capacity to the sewerage systems by means of the provision of storage as well as the possibility to increase the hydraulic gradient in excess of the gradient of the sewers and hence increase the delivery flowrate (Figure 2.6a). However, surcharge in manholes leads to different mechanisms in the energy loss and mixing processes compared to manholes which are not surcharged. In general, the energy loss and solute mixing effects at manholes increase during surcharge (Butler and Davies, 2000; Guymer *et al.*, 1998; Reed, 1983).

Extensive research has been undertaken on energy loss and mixing at manholes with different discharge and surcharge conditions as well as manhole configurations, such as manhole diameter to pipe diameter ratio, change in direction and pipe elevation level. A review of these studies is provided in Section 2.5.

2.3.2 Sewerage System Modelling

The first hydraulic computer models to describe the hydraulics of sewerage systems emerged in the 1970s. The two earliest models were Storm Water Management Model (SWMM), developed by the US EPA (United States Environmental Protection Agency), and Wallingford Storm Sewer Package (WASSP), developed by Hydraulic Research Wallingford. The aims of these models were to provide insights into the hydrodynamic performance of existing drainage networks and to plan sewer rehabilitation and new systems.

Greater environmental concern and tighter environmental constraints have led to the development of water quality models. These models are incorporated within existing hydrodynamic models to predict the transport of dissolved substances and sediments, and assess sewer flow quality. The ambition of this development is to predict the operation and response to any proposed change of both the contributing systems and the receiving environment (Guymer and O'Brien, 1995). With greater environmental concern, sewerage system network models become a useful aid in deciding the most cost-effective scheme among a number of proposals.

The transport of dissolved substances in sewerage systems involves two processes, which are advection and dispersion (for definition of terms see Section 2.4.1). However, some water quality models transport the pollutants only by advection, such as SWMM and HydroWorks (now InfoWorks) (Herath *et al.*, 1999), whilst ignoring the dispersion effects caused by the urban drainage components. There are others which also account for the effects of dispersion, such as MOUSE TRAP (DHI, 2000). The prediction of advection and dispersion of pollutants in these water quality models uses the advection dispersion equation (ADE) shown in Equation 2.7. The models which transport pollutants only by advection also use Equation 2.7 but with the omission of the dispersion term (the first term on the right hand side of Equation 2.7).

To use water quality models to predict the transport of pollutants in a drainage system requires inputs for mixing coefficients. Different values of the coefficient may be defined for different system components. However, at present, there is limited knowledge regarding appropriate values for the parameters (Lau *et al.*, 2008).

Mark *et al.* (1996) demonstrated an example of the use of the water quality model to predict the transport of industry loadings in a sewer network of Ljubljana (Slovenia) under dry weather flow conditions. Their work considered conservative pollutants and therefore the complex biological and chemical processes of the pollutants during transport in the sewers could be neglected. The final calibrated model provided good simulations of the selected pollutant (ammonium) concentration, including temporal variations at several locations within the system.

The current water quality models are regularly used for research proposes. However, their application as a management tool is restricted by the cost of collecting reliable calibration data (Ahyerre *et al.*, 1998). Without calibration, these models with the default parameter values are likely to make erroneous predictions. There are a number of practical problems associated with modelling water quality in sewers. They are a lack of knowledge regarding the biological and chemical processes of pollutants in sewers; uncertainty on the input and calibration data; and difficulty in calibration (Ahyerre *et al.*, 1998). Further research is required to make improvements in the modelling approach and to develop better understanding of the water quality processes and pollution transport mechanisms before water quality models could become a reliable and accurate engineering tool. Nevertheless, there are extensive advantages of using water quality models in the water engineering industry. In particular, it could assist with improved management and operation of the network leading to a reduction of pollutant loading to receiving watercourses.

2.4 Longitudinal Dispersion

2.4.1 Introduction

Longitudinal dispersion can be interpreted as the net longitudinal spreading of solutes resulting from differential advective velocities and transverse mixing (Green *et al.*, 1994). There are three principle processes involved in longitudinal dispersion:

1. Differential advection - The mixing is caused by the variations in velocity over the cross section of a flow;

2. Turbulent diffusion - Turbulence in a flow leads to spreading of a solute;

3. Molecular diffusion - The mixing results from the random Brownian motion.

In natural rivers and pipe flows, and without the effects of dead zones and bends, differential advection usually dominates the mixing process. The differential velocity profile tends to smear the solute with greater distance in the transverse and longitudinal directions. An example of solute dispersion in rivers is shown in Figure 2.7. A vertically-mixed tracer is injected uniformly over the depth. After some distance of travelling, at time t_1, the tracer disperses as a result of differential advection and turbulent diffusion. The parabolic profile of the tracer results from differential advection, in which the tracer travels relatively slower near the solid boundary but quicker near the surface. Turbulent diffusion results in further spreading of the tracer giving variations in the thickness of the profile. The dispersion process in pipe flows is similar to this example.
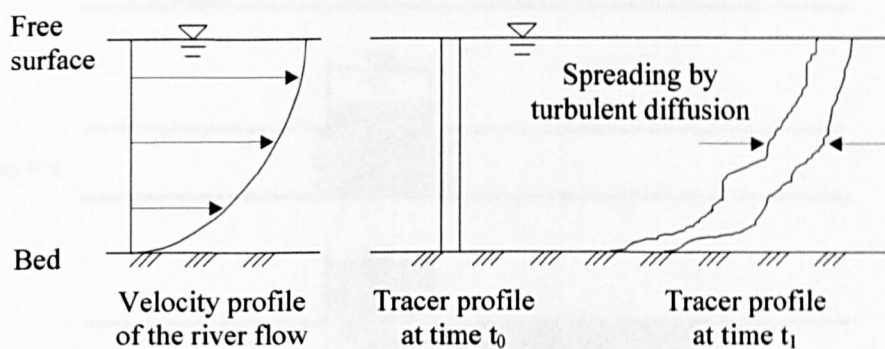
Figure 2.7 - Example of the combined effects of differential advection and turbulent diffusion on solute transport in a river flow (after Rutherford, 1994)

2.4.2 Dead Zones

A dead zone can be defined as a region in the flow with zero or relatively low velocity compared with that in the main flow. Dead zones are usually found in regions where water is stagnant or in recirculation zones. In natural rivers, because of geometrical irregularity, dead zones are a fairly common feature. Dead zones also exist in sewerage systems; for example, significant change in geometrical shape at surcharged manholes provides an extraneous volume for dynamic storage of sewage. Since manholes form one of the major components in urban drainage, the aggregated effects of the extraneous storage on mixing cannot be under-estimated.

Dead zones have a significant impact on the overall mixing process. In contrast to the differential advection dispersion which gradually spreads the solute, a dead zone can instantly attenuate the peak concentration of a solute travelling through the dead zone by a considerable amount. Figure 2.8 shows an example of dead zone effects at a surcharged manhole. At time = t_0, the tracer disperses longitudinally due to differential advection; at time = t_1, some of the tracer is entrained in the dead zone of the manhole and some form of mixing takes place in the storage volume; as the majority of the tracer has passed the manhole, the tracer which has been

trapped in the storage volume is gradually released. Since the rate of release is slow, the spread of the solute is markedly elongated. Figure 2.9 shows the dead zone effects of a surcharged manhole on temporal concentration distributions (Guymer *et al.*, 2005). The downstream profile is imparted with a reduction in the peak concentration and a skewness on the downstream profile. The peak reduction is a result of some of the tracer being retained in the storage; the skewness – with a considerably long trailing tail – reflects the slow release of the tracer as it is re-entrained into the main flow from the storage.
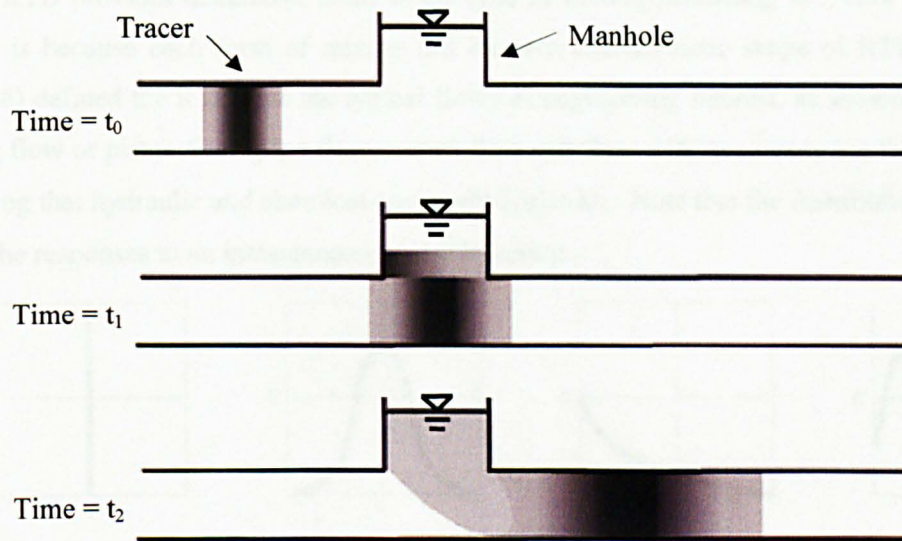
Figure 2.8 – Dead zone effects at a surcharged manhole
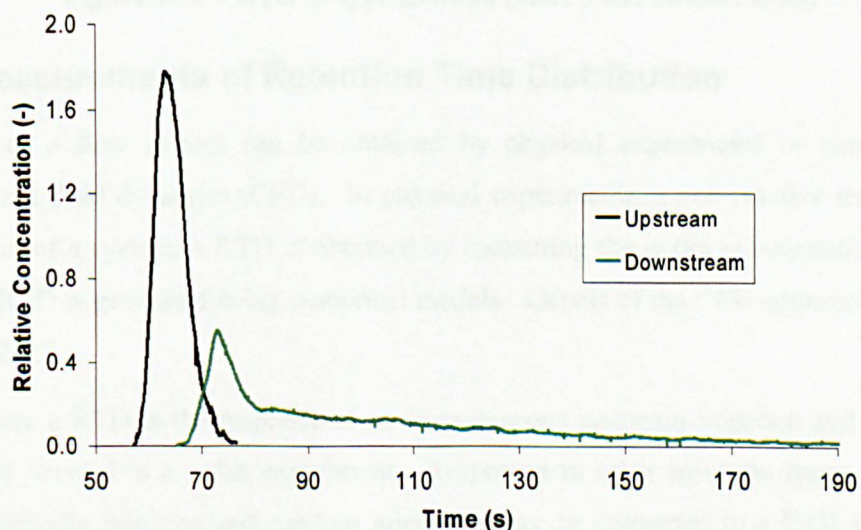
Figure 2.9 – Example of dead zone effects of a manhole on temporal concentration profiles (Manhole ID = 800 mm; Surcharge = 119 mm; Q = 2 l/s; after Guymer *et al.*, 2005)

2.4.3 Retention Time Distribution

When a neutrally buoyant solute is discharged instantaneously into the inlet of a flow system, the elements of the solute leave the system at different lengths of time due to mixing. The distribution of these times for the elements of the solute leaving the structure is referred to as the exit age distribution, or *E* curve, also termed the residence time distribution (RTD) (Danckwerts, 1958).

The RTD provides distinctive clues to the type of mixing prevailing in a flow (Fogler, 1992). This is because each form of mixing has its own characteristic shape of RTD. Danckwerts (1958) defined the RTDs for the typical flows of engineering interest, as shown in Figure 2.10. Plug flow or piston flow, pipe flow, mixed flow and flow with dead zone are the usual types of mixing that hydraulic and chemical engineers deal with. Note that the distributions in the figure are the responses to an instantaneous pulse injection.

| (a) – Piston flow or plug flow | (b) – Pipe flow | (c) – Mixed flow | (d) – Flow with dead zone |
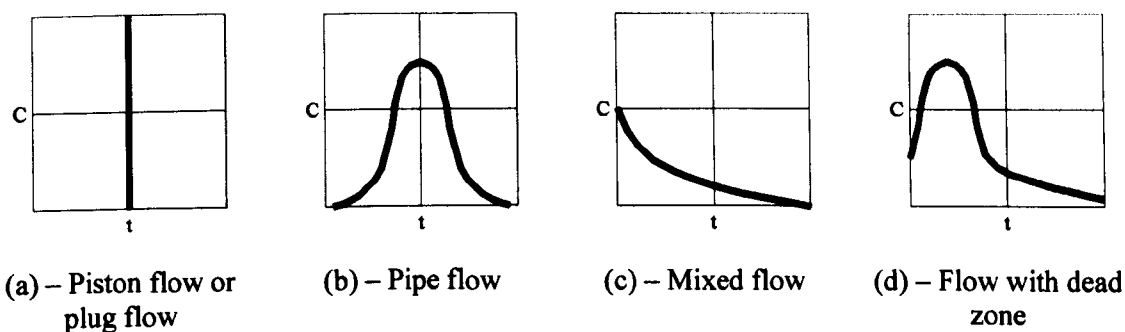
Figure 2.10 – RTD of typical flows (after Danckwerts, 1958)

2.4.4 Measurements of Retention Time Distribution

The RTD of a flow system can be obtained by physical experiments or simulated using computational fluid dynamics (CFD). In physical experiments, a non-reactive tracer is added into the inlet of a system; a RTD is obtained by measuring the outlet concentration over time. In CFD, a RTD is generated using numerical models. Details of the CFD approach are covered in Section 2.6.5.

By definition, a RTD is the response of an instantaneous upstream injection and conceptually can only be derived in a pulse experiment. Responses to other injection types, such as step injection, periodic injection and random injection, may be converted to a RTD via numerical manipulation, for example deconvolution (Section 4.4.2.3). In chemical engineering, pulse and step injection are the two most popular methodologies for the determination of RTD (Fogler, 1992). This literature review therefore focuses on pulse and step experiments. In the tracer study undertaken in this research, a Gaussian upstream distribution was recorded. This was because the injection was made some distance upstream of the upstream sampling monitor to

achieve a fully mixed condition within the pipe by the time the tracer arrived at the upstream monitor. Details of the experiments are reported in Chapter 3.

2.4.4.1 Pulse Experiment

In a pulse experiment, an amount of tracer N_o is discharged as a short pulse upstream of a flow system. The temporal concentration distribution of the tracer is recorded at the outlet. This concentration profile is termed the C_{pulse} curve (Figure 2.11).
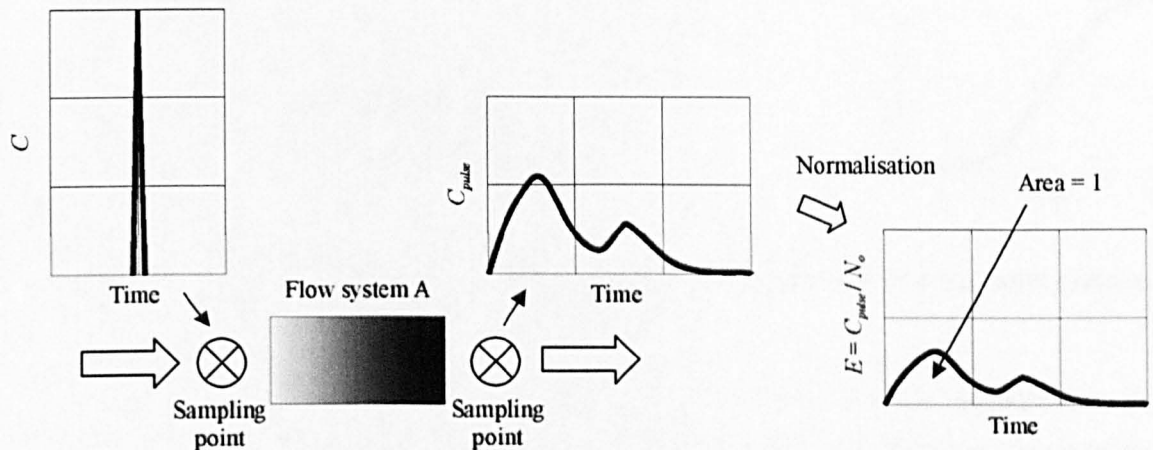
Figure 2.11 – A diagram of a pulse experiment and transformation of a C_{pulse} curve into a RTD curve, E curve

For the determination of a RTD curve, or an E curve, the C_{pulse} curve is normalised with respect to the amount of tracer N_o. If N_o is not known, it can be estimated by calculating the area under the C_{pulse} curve. A RTD has an area of 1.

There are principle difficulties in the pulse experiment regarding the generation of a reasonable pulse at the system inlet (Fogler, 1992). In physical experiments, a perfect instantaneous pulse injection (a Dirac-delta function) rarely exists. The injection must take place over a short period of time. For a valid RTD to be determined from the pulse experiment, the injection period must be negligible in comparison to the average residence time of the flow; and the longitudinal dispersion between the point of injection and the system inlet must be insignificant, meaning that the injection point has to be as close to the inlet as possible with no structure that could perturb the flow. These conditions are likely to be satisfied in large scale structures where the average residence time is high.

2.4.4.2 Step Experiment

In a step experiment (Figure 2.12), a tracer is fed into the system at a constant rate, C_{max}, until the concentration at the system outlet becomes indistinguishable from that in the feed. The outlet concentration is measured as a function of time and this curve is referred to C_{step} curve.

The dimensionless form of the C_{step} curve, normalised with respect to C_{max}, yields a F curve (Danckwerts, 1958).
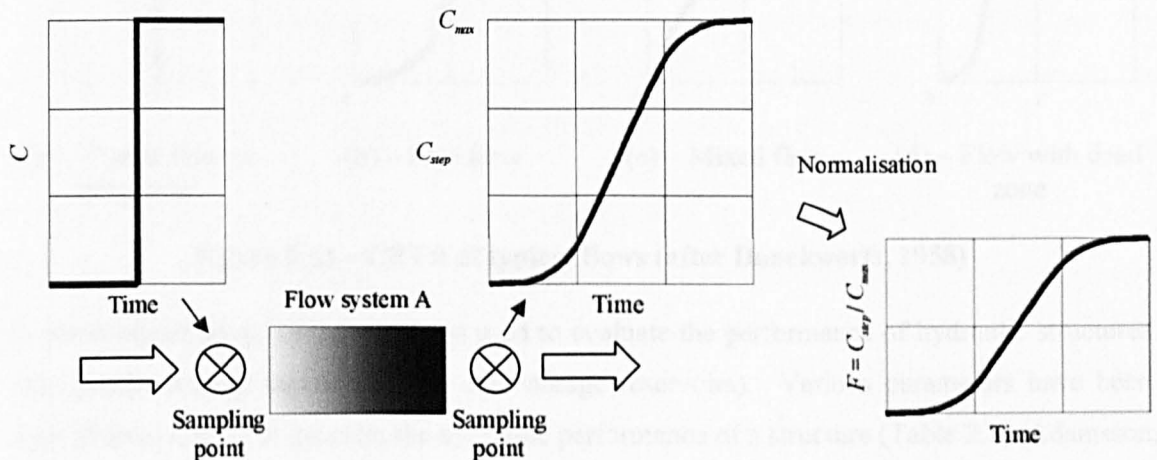
Figure 2.12 – A diagram of a step experiment and transformation of a C_{step} curve into a F curve

The F curve (a step input response) can be converted to a RTD curve (an instantaneous input response) by differentiation with respect to time (Equation 2.6). Since the reverse conversion of a RTD to a F curve is by means of integration, the F curve can be regarded as a cumulative retention time distribution (CRTD).

$$E(t) = \frac{\partial F(t)}{\partial t}$$

2.6

Fogler (1992) highlighted possible drawbacks of this technique. In laboratory experiments, to maintain a constant tracer concentration in the feed could be technically difficult and may be costly if the tracer is expensive. If a RTD curve is the interest of the study, converting a F curve to a RTD involves differentiation, which could lead to large errors in some occasions. In contrast to the pulse experiment, the step experiment seems to be suitable for small scale structures.

2.4.4.2.1 Application of CRTD

The CRTD represents an alternative presentational form of the RTD. Similar to the RTD, each type of flow is represented by a characteristic shape of CRTD (Figure 2.13). However, one major difference between the two types of presentation is that CRTD enables analysis to be made regarding the performance of a flow system (Danckwerts, 1958).

(a) – Piston flow or plug flow   (b) – Pipe flow   (c) – Mixed flow   (d) – Flow with dead zone
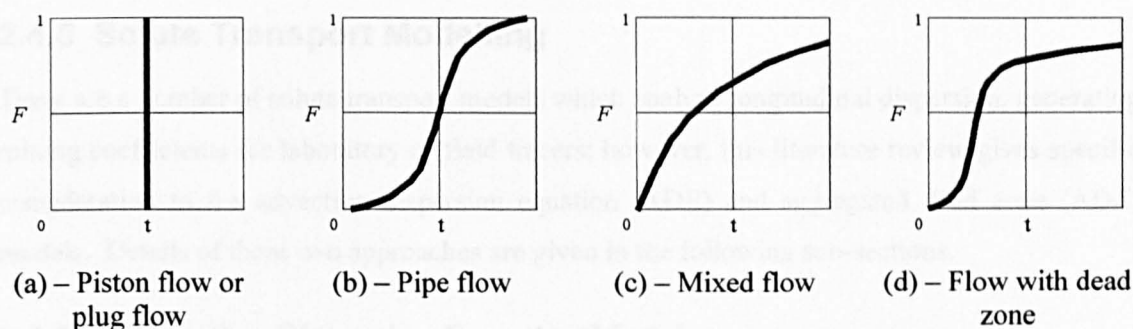
Figure 2.13 – CRTD of typical flows (after Danckwerts, 1958)

In water engineering, CRTD has been used to evaluate the performance of hydraulic structures (e.g. ponds, storage tanks, wetlands and storage reservoirs). Various parameters have been derived from CRTD to describe the hydraulic performance of a structure (Table 2.1) (Adamsson, 2004; Persson, 2000). However, at present, there is no general consensus on which parameter is the best for assessing the hydraulic performance of a system. A discussion on which parameter should to be used to quantify short-circuiting in storage chambers is presented in Stovin *et al.* (in press).

Literature	Purposes	Definition
Thackston *et al.* (1987)	A measure of the effective volume ratio	t_{50}/t_n
Ta and Brignal (1998)	A measure of short circuiting	t_{16}/t_{50}
Persson *et al.* (1999)	A measure of short circuiting	t_{peak}/t_n; t_{peak} is the time to peak concentration
Reddy *et al.* (1999)	A measure of short circuiting	t_{16}/t_n

Table 2.1 – Hydraulic parameters for the assessment of the performance of a hydraulic structure (t_i is the time at which the *i* percentage of the tracer has left the system)

Another application of CRTD is to predict the distributions of residence times for a system at different physical scale, i.e. for scaling purposes. Danckwerts (1958) suggested that if a model is geometrically similar to the prototype and the principles of scaling, for example Reynolds number or Froude number is identical between the model and prototype, are valid, the CRTD normalised with respect to the volumetric travel time corresponding to the model should be identical to that for the prototype. However, no scaling examples using CRTD were demonstrated in his work and the validity of this application of CRTD (for scaling purposes) is not clear. This scaling method has been tested and used to examine the effects of scale at surcharged manholes in this study.

2.4.5 Solute Transport Modelling

There are a number of solute transport models which analyse longitudinal dispersion, generating mixing coefficients for laboratory or field tracers; however, this literature review gives specific consideration to the advection dispersion equation (ADE) and aggregated dead zone (ADZ) models. Details of these two approaches are given in the following sub-sections.

2.4.5.1 Advection Dispersion Equation Model

The advection dispersion equation (ADE) model, derived by Taylor (1954), was originally developed for the transport of a solute in pipe flows (Equation 2.7). This equation can account for the effects of advection and dispersion due to molecular diffusion, turbulent diffusion and differential advection. Mixing is described by a dispersion coefficient, K, which is a hydraulic property of a flow.

$$\frac{\partial C}{\partial t} + U\frac{\partial C}{\partial x} = K\frac{\partial^2 C}{\partial x^2} \qquad\qquad 2.7$$

where:

C	is the concentration
K	is the longitudinal dispersion coefficient
U	is the mean velocity of the flow
x	is the longitudinal direction

The advection dispersion equation (ADE) model, also called the Fickian model, was founded on the basis of Fick's first law (derived by Fick in 1855) that relates dispersion to some properties of the average tracer concentration. The validity of Equation 2.7 is therefore confined to a flow condition that satisfies Fick's law. This condition occurs when the differential advection effects and turbulent diffusion reach an equilibrium (Taylor, 1921), usually some distance after the injection where the spatial concentration variation becomes Gaussian. This zone is known as the equilibrium zone where the variance of the concentration distributions is a linear function of distance (Figure 2.14). In the near field, the correlation between dispersion and the average tracer concentration using Fick's first law is invalid. This is because the differential advection effect is not in equilibrium with turbulent diffusion. Within this zone, known as the advection zone, the tracer profile is highly skewed or asymmetrical due to the velocity distribution (Rutherford, 1994).
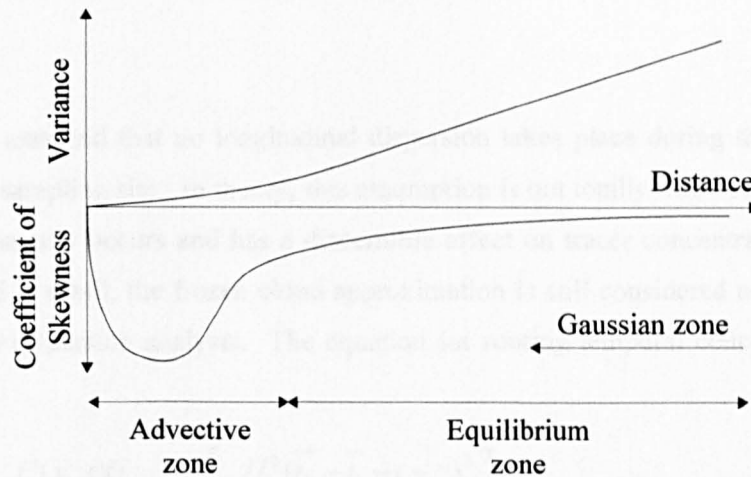
Figure 2.14 – Variation of the variance and skewness of a concentration profile with time predicted by the Fickian model (after Rutherford, 1994)

2.4.5.1.1 Solution of the ADE Model

The spatial concentration profile, $C_s(x, t)$, can be predicted using Equation 2.7. Assuming U and K are constant and a point source is injected, the solution to the equation is (Rutherford, 1994; Taylor, 1954):

$$C_s(x,t) = \frac{M}{A\sqrt{4\pi Kt}} \exp\left[-\frac{(x-Ut)^2}{4Kt}\right] \qquad \qquad 2.8$$

where:

A   is the cross sectional area of the channel

M   is the mass of tracer injected at $x = 0$ and $t = 0$

Using Equation 2.8 to route the spatial downstream profile from a slug injection, a Gaussian bell-shaped profile would be obtained. However, the present form of the equation poses difficulties for practical use. This is because measurements are reported as temporal concentration profiles at a fixed sampling site, rather than a spatial profile at a fixed time; and the input profiles are usually temporally distributed. Rutherford (1994) proposed two routing methods to predict temporal profiles from a temporally distributed input, which are 'frozen cloud method' and 'Hayami solution'. However, only the frozen cloud approximation will be discussed in more detail as it was used in this study. The frozen cloud approximation was adopted to analyse the traces in previous manhole research (Dennis, 2000; Guymer *et al.*, 2005; O'Brien, 2000; Saiyudthong, 2004).

The frozen cloud approximation suggests that advection dominates dispersion in many situations, such that:

$$\frac{x}{U} >> \frac{K}{U}$$

2.9

Therefore, it is assumed that no longitudinal dispersion takes place during the time taken for tracer to pass a sampling site. In theory, this assumption is not totally true because longitudinal dispersion continually occurs and has a discernible effect on tracer concentrations. Since the error introduced is small, the frozen cloud approximation is still considered accurate and valid for longitudinal dispersion analysis. The equation for routing temporal concentration profiles reads:

$$C(x_2,t) = \int_{\gamma=-\infty}^{\infty} \frac{C(x_1,t)U}{\sqrt{4\pi K(\overline{t_2}-\overline{t_1})}} \exp\left[-\frac{U^2(\overline{t_2}-\overline{t_1}-t+\gamma)^2}{4K(\overline{t_2}-\overline{t_1})}\right] d\chi$$

2.10

$$\overline{t_i} = \frac{\int_{\gamma=-\infty}^{\infty} t C(x_i,t)dt}{\int_{\gamma=-\infty}^{\infty} C(x_i,t)dt}$$

2.11

where:

subscript $_{1\ \&\ 2}$ denote upstream and downstream profile respectively

$C(x_i, t)$ is the temporal concentration at profile i

$\overline{t_i}$ is the time at the centroid of the tracer at profile i

χ is the integration time

The frozen cloud routing method effectively divides the upstream profile into a number of individual elements with a width of Δt. These individual elements act as a single instantaneous injection source and each of the individual downstream profiles predicted by Equation 2.10 are projected downstream, given that the travel time, $\overline{t}$ and dispersion coefficient, K, are known. Through superposition, the entire downstream profile with reference to the upstream profile can be attained. An example of the frozen cloud routing method is shown in Figure 2.15.
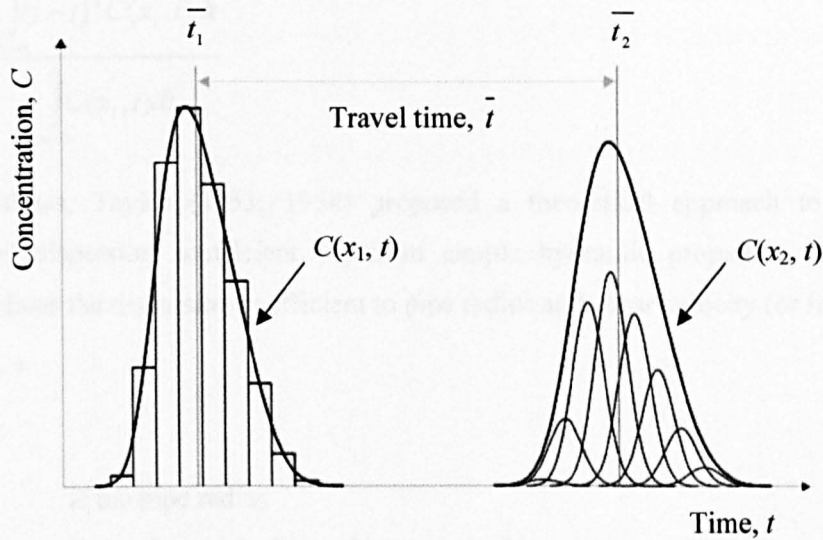
Figure 2.15 – Example of the ADE frozen cloud routing procedure

Rutherford (1994) suggested four points to be aware of when applying the routing procedure:

1. The upstream profiles must be outside the advection zone;

2. A complete temporal concentration upstream profile, including the leading edge and the long tail, must be captured;

3. If tracer loss is detected, a correction must be made prior to the routing procedure;

4. The parameters, U or $\bar{t}$ and K, inputted to Equation 2.10 should be reach-averaged values.

The ADE model requires values for the parameters, travel time, $\bar{t}$, and the dispersion coefficient, K, in order to make a prediction of a downstream concentration profile. A method to estimate the value of these model parameters was demonstrated by Fischer (1966). It was proved that they can be estimated if both upstream and downstream concentration profiles are available. Through measuring the time between the centroids of the profiles and the variance, i.e. spread, of the profiles, the parameters can be obtained by:

$$\bar{t} = \bar{t_2} - \bar{t_1} \tag{2.12}$$

$$K = \frac{U^2}{2} \cdot \frac{\sigma^2(x_2) - \sigma^2(x_1)}{\bar{t_2} - \bar{t_1}} \tag{2.13}$$

where:

σ^2 refers to the temporal variance of the profile:

$$\sigma^2(x_i) = \frac{\int\limits_{t=-\infty}^{\infty}(t-\bar{t})^2 C(x_i,t)dt}{\int\limits_{t=-\infty}^{\infty}C(x_i,t)dt}$$

2.14

For pipe flows, Taylor (1953; 1954) proposed a theoretical approach to estimating the longitudinal dispersion coefficient, K, from simple hydraulic properties. The theoretical equation relates the dispersion coefficient to pipe radius and shear velocity (or friction velocity):

$$K = 10.1ru*$$

2.15

where:

r   is the pipe radius

$u*$ is the shear velocity or friction velocity

For smooth pipes, Taylor (1954) and Goldstein (1938) state that:

$$u^* = U\sqrt{\frac{\gamma}{2}}$$

2.16

$$\gamma^{-0.5} = -0.4 + 4\log_{10}Re + 2\log_{10}\gamma$$

2.17

where:

γ is a measure of pipe friction

However, Taylor's pipe equation is solely applicable to pipe flows and the constant of the equation, 10.1, does not hold for all pipe cases. For different pipe roughness and curvature, the constant seemed to vary from 10.0 to 21.9 (Taylor, 1954).

An optimisation procedure, such as that proposed by Dennis (2000), could also be adopted for the determination of model parameters from a pair of measured traces. The technique performs refined searches for pairs of model coefficients until a predefined resolution of the coefficients is reached. The pair of model coefficients derived should be the best pair to describe the mixing process of the flow system. Further information of the optimisation procedure is provided in Chapter 4.

2.4.5.1.2 Limitations of the ADE Model

The ADE model has been proved its applicability in pipe flows and laboratory-based open channel flows (Green et al., 1994). However, in the case of natural rivers or flows with dead zones, the Fickian model fails to describe observed tracer profiles (Day, 1975; Lees et al., 2000; Thackston and Schnelle, 1970). Dead zones can serve to retain portions of the solute as the

main cloud passes by, from where the solute is then slowly released back into the flow zone (Figure 2.8). The effect of this is reflected by a skewed temporal concentration profile with a long low concentration tail (e.g. Figure 2.9).

Over the last thirty years, two different modelling approaches have been developed in order to describe the mixing process in a flow with dead zones. One of the approaches suggested use of a transient storage (TS) model incorporated into the ADE model to account for the effects of dead zone (e.g. Pedersen, 1977; Thackston and Schnelle, 1970):

$$\frac{\partial C}{\partial t} + U \frac{\partial C}{\partial x} = K \frac{\partial^2 C}{\partial x^2} + K_s (C_t - C) \qquad \textbf{2.18}$$

$$\frac{\partial C_t}{\partial t} = K_s \frac{A}{A_t} (C - C_t) \qquad \textbf{2.19}$$

where:

A	is the average main channel cross sectional area
A_t	is the storage zone cross sectional area
C_t	is the storage zone solute concentration
K_s	is the storage exchange coefficient
K	is the longitudinal dispersion coefficient

Equation 2.18 and Equations 2.19 show the general TS model. The two terms on the left hand side and the first term on the right hand side of Equation 2.18 form the basis of the ADE model (Equation 2.7); the second term on the right hand side of Equation 2.18 and Equation 2.19 are elements to describe the mixing process in dead zones. The parameters of interest defining the solute transport in the TS model are K, α, A_t, U or A for a known discharge. These parameters are assumed to be constant in time and space within a reach. Parameter estimation techniques for the TS models, such as the OTIS model (Runkel, 1998) and the HART model (Hart, 1995), have been developed to analyse temporal concentration profiles. In this research, consideration was not given to the TS model for the longitudinal dispersion analysis in surcharged manholes. This is because the TS model is currently not implemented in sewerage system models; and most importantly, there are no general rules to link the parameter values to physical properties of a system, which poses difficulties in studying the scale effects through these parameters. Further discussion of the TS model is not given in this literature review but can be found in Runkel (1998) and Hart (1995).

The second approach developed to describing dead zone mixing (non-Fickian behaviour) was the aggregated dead zone model (ADZ), proposed by Beer and Young (1983). This model

originated from the cell-in-series (CIS) model suggested by Stefan and Demetracopoulas (1981). Further discussion of these models is given in the following sub-sections.

2.4.5.2 Non-Fickian Dispersion Models

2.4.5.2.1 Cells-In-Series Model

The cells-in-series (CIS) model is the first dispersion analysis model that is not based on Fick's law (Stefan and Demetracopoulas, 1981). The model takes an initial assumption that a reach is sub-divided into a series of sub-reaches, also called cells, which flow into each other. In each cell, the solute is assumed to be instantaneously mixed; therefore, the concentration of the outflow from each cell is equal to the average concentration in the cell. The concentration of a solute is determined by the concentration of the inflow and the residence time of the cell. The mathematical expression for the mass transport of a solute in a sub-reach is given by:

$$V \frac{\partial C(t)}{\partial t} = M(t) - QC(t) \qquad\qquad 2.20$$

where:

$C(t)$	is the tracer concentration at time t
$M(t)$	is the external mass flowing into the sub-reach at time t
Q	is the discharge flowing out of the sub-reach
t	is time
V	is the volume of the sub-reach

There are two drawbacks of the CIS model which explain its unpopularity in the water engineering industry. Firstly, the model does not reproduce a skewed profile which is often a feature of the traces in natural rivers (Stefan and Demetracopoulos, 1981) and sewers (Guymer and O'Brien, 2000; Guymer *et al.*, 2005). Furthermore, the number of cells determines the travel time, dispersion and also the skewness of the prediction, which limits the usefulness of the model as these parameters cannot be varied independently (Rutherford, 1994). Nevertheless, the CIS model is widely used in chemical engineering for modelling mixing in reactors or vessels (Levenspiel, 1962).

2.4.5.2.2 Aggregated Dead Zone Model

The Aggregated Dead Zone (ADZ) model, developed by Beer and Young (1983), is a variant on the CIS model. The model encapsulates the concept of using a sub-reach to represent the whole reach; and suggests that the overall dispersion of the reach, including molecular and turbulent diffusion, differential advection and dead zone effects, can be accounted by a single ADZ

element or a number of ADZ elements. A reach time delay term is introduced into the input mass, $M(t)$, in Equation 2.20. This is to allow separate description of the advection and dispersion processes. The resultant equation becomes:

$$\frac{\partial C(x_2, t)}{\partial t} = \frac{1}{T} C(x_1, t - \tau) - \frac{1}{T} C(x_2, t) \qquad\qquad 2.21$$

where:

T refers to residence time

τ refers to reach time delay

In practice, data is often acquired at discrete sampling intervals. Young and Wallis (1986) state that the discrete solution of the first order ADZ model can be written as:

$$C(x_2, t) = (1 + \alpha) C(x_1, t - \delta) - \alpha C(x_2, t - 1) \qquad\qquad 2.22$$

where:

α equals $-e^{\left(\frac{-\Delta t}{T}\right)}$

δ is the nearest integer value to $\tau/\Delta t$ and Δt is the time step

The model coefficients of the ADZ model, which are α and δ, can be determined from the temporal information, such as reach time delay, travel time and residence time, of the temporal concentration profiles shown in Figure 2.16. Reach time delay is defined as the time difference between the first arrival trace of the up and downstream profiles; and residence time, T, is the difference between travel time and time delay (Equation 2.23). Note that the determination of the ADZ model coefficients for a pair of temporal concentration profiles could also be conducted using the optimisation procedure, proposed by Dennis (2000). Details of parameter estimation technique are given in Chapter 4.

$$T = \bar{t} - \tau \qquad\qquad 2.23$$

The overall travel time, $\bar{t}$, is segregated into two temporal components: reach time delay and residence time. Reach time delay refers to the travel time for pure advection and residence time can be interpreted as the time spent in dispersion. If these temporal parameters are multiplied by discharge, they become volumetric components which may be interpreted as: travel time corresponds to total reach volume, V_t; reach time delay is related to the volume in which advection occurs, V_a; and residence time is analogous to the volume of dead zone associated with dispersion, V_d.

Young and Wallis (1986) defined dispersive fraction (DF) to describe the mixing characteristics within a reach. DF is defined as the ratio of dead zone to total reach volume (Equation 2.24)

and ranges from 0 to 1. A value of 1 indicates 100 % of the total volume introducing dispersion effects, while a value of 0 is indicative of pure advection. The physical meaning of the DF parameter is similar to the dispersion coefficient in the ADE model (Equation 2.7).

$$DF = \frac{V_d}{V_t} = \frac{T}{\bar{t}} \qquad\qquad 2.24$$
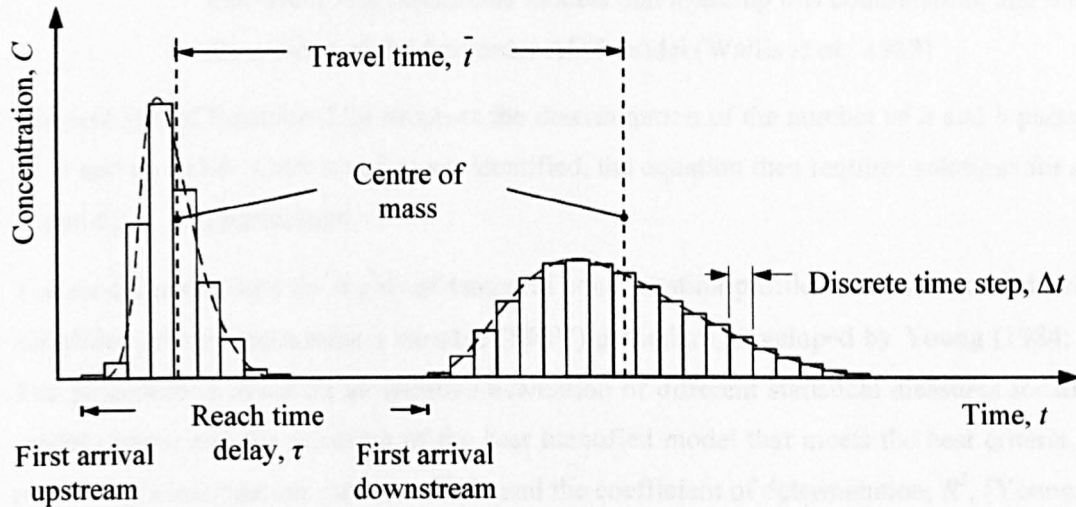
Figure 2.16 – Estimation of the model coefficients for the ADZ model from traces

2.4.5.2.2.1   ADZ in Series and Parallel Connections

Series or parallel connections of the first order ADZ models may be sometimes required to describe observed higher-order transport mechanisms (Lee *et al.*, 2000). To combine a number of the first order ADZ models, a general discrete time transfer function (TF) form of the model is required (Young, 1992):

$$C(x_2,t) = \frac{bz^{-\delta}}{1 + az^{-1}} C(x_1,t) \qquad\qquad 2.25$$

where:

a	is equal to α
b	is equal to $1+\alpha$, and $b = 1+a$
$z^{-\delta}$ or z^{-1}	is from the transfer function that $C(k,t-i) = z^{-i}C(k,t)$

The general discrete time model for a number of the ADZ models in series or parallel then takes the form:

$$C(x_2,t) = \frac{B(z^{-1})z^{-\delta}}{A(z^{-1})} C(x_1,t) \qquad\qquad 2.26$$

$$B(z^{-1}) = b_0 + b_1 z^{-1} + ... + b_m z^{-m}$$ **2.27**

$$A(z^{-1}) = 1 + a_1 z^{-1} + ... + a_n z^{-n}$$ **2.28**

where:

n, m are integers whose value depends on the nature of both the combination and the individual ADZ elemental models that make up this combination; and n defines the number of the first order ADZ model (Wallis *et al.*, 1989)

The problem of Equation 2.26 involves the determination of the number of a and b parameters, i.e. n and m, and δ. Once n and m are identified, the equation then requires solutions for $a_1, ... , a_n$ and $b_o, ... , b_m$ parameters.

The model parameters for a pair of temporal concentration profiles can be estimated using the simplified refined instrumental variable (SRIV) procedure, developed by Young (1984; 1985). The procedure is based on an iterative evaluation of different statistical measures for different model orders; and the selection of the best identified model that meets the best criteria, which are Young's information criterion (YIC) and the coefficient of determination, R^2, (Young, 1992). The YIC is a combined measure of model fit and parametric efficiency; and R^2 is a measure of goodness of fit between the variance of the predicted and observed profiles:

$$R^2 = 1 - \frac{\sigma_o^{\ 2}}{\sigma_p^{\ 2}}$$ **2.29**

where:

$\sigma_{o,p}$ is the variance of the observed and predicted profiles respectively

Further details of the SRIV analytical procedure can be found in Young (1984; 1985).

2.5 Previous Manhole Research

Extensive research has been conducted on head loss and mixing at surcharged manholes and a wide range of geometrical configurations have been studied, such as manholes with different 'manhole diameter to pipe diameter' ratios; step manholes; manholes with pipe direction change; and manholes with benching (see schematic diagrams of these manholes in Figure 2.17). The majority of the work was based on laboratory scale models and conducted under steady state conditions; while a small proportion of the work was carried out in field tests where measurements were taken in real sewer networks. During dry weather flows, there is little problem with sewerage operation. Therefore, most of the research focused on storm conditions, during which manholes may be surcharged. Some other manhole research investigated supercritical flow across sewer manholes when the sewer is not surcharged (e.g. Gargano and

Hager, 2002; Giudice and Hager, 2001; Martino *et al.*, 2002). However, supercritical flow across sewer manholes is not within the scope of the present research, and further discussion of this topic is not provided here.

This section provides a review of previous manhole research and begins with energy loss.
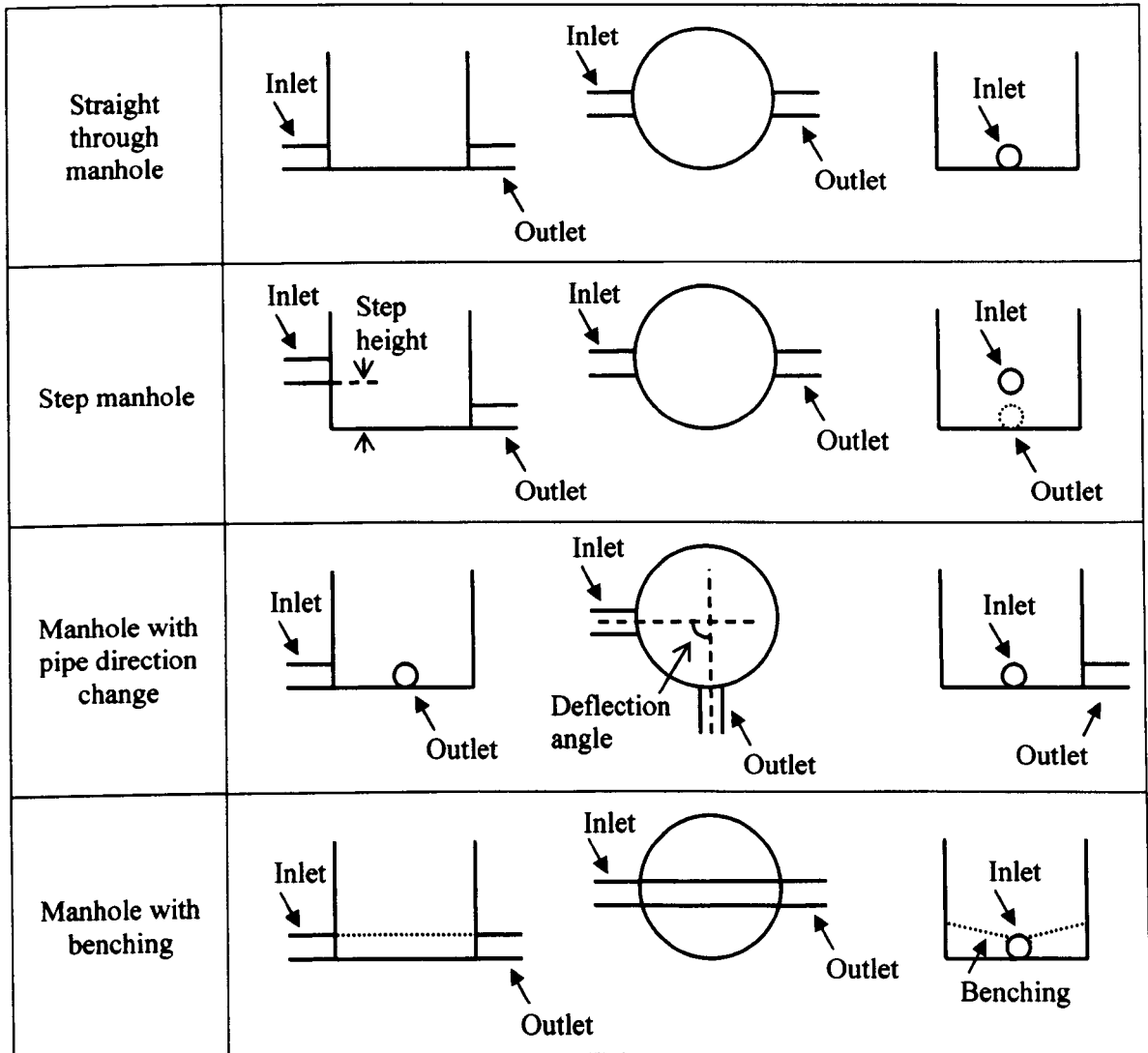
Figure 2.17 – Schematic diagrams of manhole with different manhole configurations
(Left – Side elevation; Middle – Top view; Right – Front elevation)

2.5.1 Energy Loss in Surcharged Manholes

There have been three major reasons for the investigation of energy loss at surcharged manholes. Firstly, the energy loss caused by these structures is important for pipeline engineers to know when designing a gravity-fed sewer network. Secondly, sewerage system models require inputs for energy loss coefficients to make predictions of head loss at surcharged manholes and hydrodynamic performance of an urban drainage system. Thirdly, to study design alternatives,

such as baffle plates and benching configurations, to minimise or reduce head loss across manhole structures (Johnston and Volker, 1990; Marsalek and Greck, 1988).

Determination of energy loss in previous manhole research was based on the analytical method proposed by Sangster *et al.* (1958). The head loss due to a manhole, ΔH, is defined as the difference in pressure head at the manhole centreline between the extrapolated upstream and downstream hydraulic lines (Figure 2.18); and the value of the energy loss coefficient can then be determined using Equation 2.30.

$$\Delta H = K_L \frac{u^2}{2g}$$ 2.30

where:

g   is the gravitational acceleration

K_L is the head loss coefficient

u   refers to the mean pipe velocity
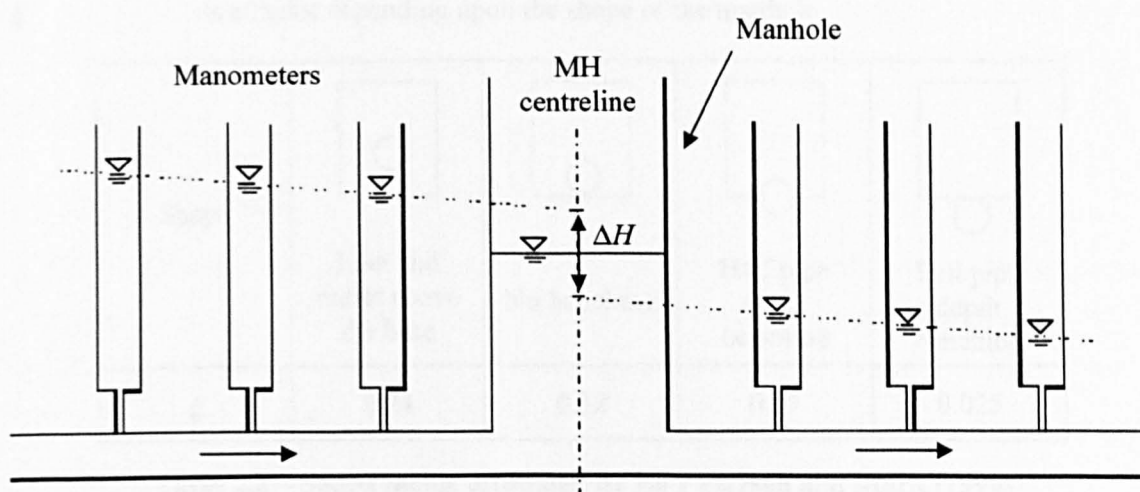
Figure 2.18 – Manhole head loss estimation

There are a wide range of manhole configurations in a sewerage system. However, the findings for one manhole configuration do not necessarily apply to a manhole with a different configuration; for example, the energy loss coefficient for a step manhole would be different from that of a typical straight through manhole. Therefore, each manhole configuration requires independent study for the evaluation of its hydraulic performance.

2.5.1.1 Manhole Shape and Size

Archer *et al.* (1978) conducted laboratory experiments for circular and rectangular manholes with benching. Their results suggested that the variations of head loss coefficient between the

two types of manholes were not significant but that rectangular manholes tended to have lower energy loss than circular manholes.

Sangster *et al.* (1958) investigated manholes with different manhole diameter to pipe diameter (D/D_p) ratios. Their investigation concluded that head loss increased with the D/D_p ratio; however, there was no increase in head loss for D/D_p greater than 2.5. In the studies of Bo Pedersen and Mark (1990) and Howarth and Saul (1984), energy loss at surcharged manholes continued to increase up to a D/D_p value of greater than 4.0. Bo Pedersen and Mark (1990) also developed an empirical equation using submerged jet theory (see Section 2.5.3), developed by Albertson *et al.* (1950), to correlate energy loss coefficient to D/D_p and manhole shape (Equation 2.31). This empirical equation is implemented in MOUSE (DHI, 2008).

$$K_L = \xi\left(\frac{D_m}{D_p}\right)$$

2.31

where:

ξ is a factor depending upon the shape of the manhole
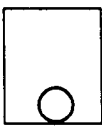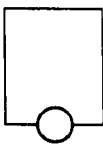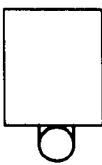
Shape	Inlet and outlet above the base	No benching	Half pipe depth benching	Full pipe depth benching
ξ	0.24	0.12	0.07	0.025

Table 2.2 – Shape factor estimated by Bo Pedersen and Mark (1990)

2.5.1.2 Flow Conditions

Most of the research on manhole head loss was carried out under steady state conditions and assumed that the parameters derived can be applied to unsteady state flows, which are normally seen in the real sewerage systems. Howarth and Saul (1984) undertook a study to examine the effects of this assumption by assessing the difference in the head loss obtained from steady state and unsteady state tests.

One of the important findings of their work was that a circular swirling flow appeared in the manholes at low surcharge depths. The effects of the swirling flow led to a considerable increase in energy loss; in some cases, the energy loss coefficients increased seven times in comparison to those derived during the absence of the swirling.

The study also suggested that in the absence of the swirling in the manhole, similar values of the head loss coefficients were obtained in the steady state and unsteady state testes. In contrast, when the swirling appeared, the steady state values were higher than those derived from the unsteady state experiments.

2.5.1.3 Surcharge Level

A number of studies (Arao and Kusuda, 1999; Howarth and Saul, 1984; Johnston and Volker, 1990; Lindvall, 1984) showed a transition in the energy loss characteristics in response to variations of surcharge level; at low surcharge depths, before the threshold depth at which the transition occurred, energy loss appeared to increase with surcharge depth; after the transition, energy loss dropped to a much lower level and stayed constant as a function of surcharge. Howarth and Saul (1984) explained that the excessive energy loss at the low surcharge depths was related to the existence of the swirling motion in the manhole. The results presented by Arao and Kusuda (1999) and Lindvall (1984) suggested that the point at which the transition of the coefficient occurred, i.e. the threshold level, was constant with discharge. An example of the variations of energy loss with surcharge, published by Arao and Kusuda (1999), is provided in Figure 3.17.

2.5.1.4 Step Height

Kusuda and Arao (1996) and Kusuda *et al.* (1993) presented the results from a comprehensive investigation of head loss at circular step manholes. In these studies, a wide range of manhole diameter to upstream pipe diameter (D/D_p) ratios from 1.4 to 3.6 and step heights (defined as the difference in invert level between the inlet and outlet pipes) from $0.0D_p$ to $4.0D_p$ were considered. These studies concluded that for step heights between $0.0D_p$ and $1.5D_p$, head loss coefficient increased with step height; however, further increase in step height resulted in no increase in the coefficient value.

2.5.1.5 Change in Direction

The energy loss at surcharged manholes with change in pipe direction has been studied by Archer *et al.* (1978), Marsalek and Greck (1988) and Saiyudthong (2004). In general, all study results showed that the energy loss was higher when there was a change in pipe direction in manhole structures. For instance, the energy loss coefficient for a benched manhole with 60° deflection, i.e. the difference in the angle of the pipes, was approximately six times the value for a benched manhole of the same diameter with no pipe deflection (Archer *et al.*, 1978; Saiyudthong, 2004).

2.5.1.6 Benching

The effects of benching within manholes have been shown to introduce a large influence on the recorded energy loss coefficient. Marsalek (1984) examined square and circular manholes with benching arrangements (no benching, half pipe depth benching and full depth benching). The study found that the unbenched manholes had double energy loss compared with those with full depth benching. This observation also agreed with the experimental results of Johnston and Volker (1990). Howarth and Saul (1984) commented that benching could prevent the swirling within the manholes and reduce energy loss at low surcharge depths.

2.5.2 Longitudinal Dispersion in Surcharged Manholes

Detailed investigation of solute transport in manholes began with Guymer and O'Brien (1995). The aims of their study were to quantify dispersion due to surcharged manholes and to provide this information in a format that could be used by sewerage system models, such as MOUSE TRAP. Further investigation of mixing in manholes was followed by Dennis (2000); Guymer and O'Brien (2000); Guymer *et al.* (1996, 1998 and 2005) and Saiyudthong (2004). These studies investigated the effects of different manhole configurations, such as change in manhole diameter, step height and pipe direction and benching, on the mixing process in manholes.

Previous longitudinal dispersion studies for surcharged manholes were based on laboratory tracer experiments in physical scale models. A small amount of dye (Rhodamine WT) was injected in the flow upstream of the manhole and its concentration was measured using fluorometers at either side of the manhole. Temporal concentration profiles were then recorded and analysed using the ADE and ADZ models, in association with standard moment analysis and the optimisation procedure proposed by Dennis (2000), to produce model parameters. Note that in this literature review, only the results analysed by the optimisation procedure will be discussed. This is because these parameter results could produce predictions in better agreement with the measured profiles then the results of standard moment analysis (Dennis, 2000). Details of the optimisation procedure are covered in Chapter 4.

2.5.2.1 Manhole Size and Surcharge

The effects of manhole diameter on longitudinal dispersion at surcharged manholes were comprehensively studied by Guymer *et al.* (2005). In their studies, four unbenched manholes with different D/D_p ratios (4.55, 5.68, 6.82 and 9.09; or manhole internal diameters of 400 mm, 500 mm, 600 mm and 800 mm) were investigated under a wide spectrum of discharge and surcharge conditions. One of the important findings in the study was the identification of the threshold surcharge level at which the solute transport characteristics indicated a sharp transition

between pre- and post-threshold conditions; at surcharge levels below the threshold, the travel times varied linearly with surcharge, whilst above the threshold travel times dropped to a low and constant level (see example in Figure 2.19). The threshold surcharge level appeared to be more pronounced in manholes with a large D/D_p ratio.
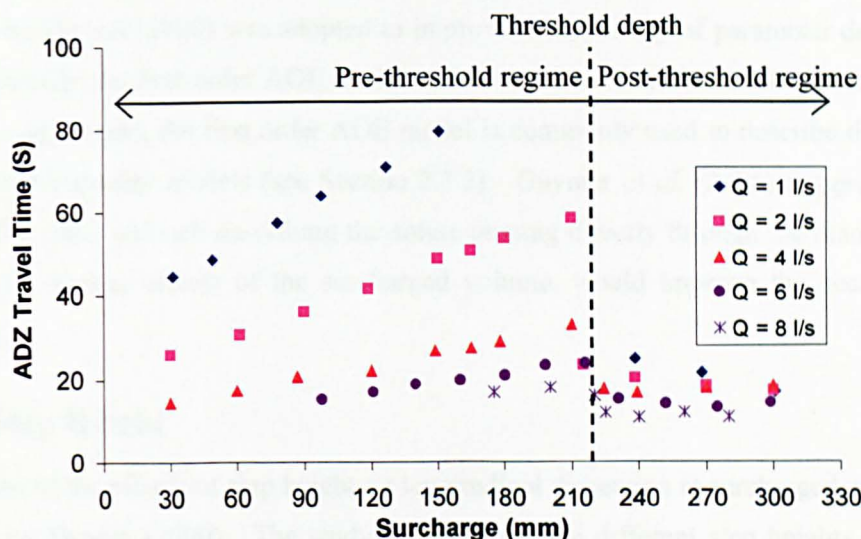
Figure 2.19 – Variations of the ADZ travel time with surcharge for the 800 mm ID manhole (after Guymer et al., 2005)

The manhole diameter directly relates to the volume of water available for mixing. In theory, a manhole with a larger size should provide more mixing within the chamber. The analysed model coefficient results agreed with this theory and showed that the model coefficients corresponding to the same discharge and surcharge conditions, such as travel time, dispersion coefficients and dispersive fraction, in the ADE and ADZ models increased with manhole diameter. This was with the exception of reach time delay that appeared to be independent of manhole diameter.

Guymer et al. (2005) derived a large amount of ADE and ADZ model parameters from the four laboratory scale manhole models in the tracer experiments under a wide range of discharge and surcharge conditions. The relationship between the model coefficients and discharge and surcharge was developed. Guymer et al. (2005) suggested that the derived relationship may be used in water quality models to improve predictions of temporal and spatial water quality variation within sewerage systems. However, Guymer et al. (2005) also commented that the application of their laboratory results is limited to the range of hydraulic conditions and manhole configurations considered in the experiments. The author also thought that at present, their experimental results may only be applicable to the specific scale of the manholes studied in the laboratory experiments, as the scalability of the laboratory scale derived coefficients to full

scale structure in the urban drainage system is not clearly understood. Scaling law or methodology for these model parameters was not considered in their work.

Another concern raised in their work was that the first order ADE and ADZ models do not fully describe the mixing process occurring in the manholes, although the optimisation technique developed by Dennis (2000) was adopted to improve the accuracy of parameter determination. This is especially the first order ADE model which could not account for the mixing effects of dead zone. At present, the first order ADE model is commonly used to describe the dispersion effects in water quality models (see Section 2.3.2). Guymer *et al.* (2005) suggested that two parallel ADZ cells, one cell describing the solute passing directly through the manhole and the other for the storage effects of the surcharged volume, would improve the accuracy of the predictions.

2.5.2.2 Step Height

Examination of the effects of step height on longitudinal dispersion at surcharged manholes was conducted by Dennis (2000). The study investigated five different step heights, which were $0.0D_p$, $0.5D_p$, $1.0D_p$, $1.5D_p$ and $2.0D_p$, in a 388 mm internal diameter manhole. Dennis (2000) concluded that the degree of mixing at the manhole increased with step height and explained this phenomenon by the theory that the increase in step height led to a greater contact between the incoming jet and the stored water. Therefore, a greater transfer of tracer between the dead zone and the main flow zone was achieved. The analysed model coefficients, which were travel time, dispersion coefficients and dispersive fraction except reach time delay, showed an approximately linear relationship with step height. The model coefficients appeared to be independent of surcharge depth, showing no evidence in the transition of the solute transport characteristics. However, the author assumed that this might be because Dennis (2000) primarily focused on high surcharge levels.

2.5.2.3 Change in Direction

Investigations were made by Saiyudthong (2004) to examine the effects of manhole with change in pipe direction on the mixing process. Tracer studies were undertaken in a 388 mm internal diameter manhole with four different deflection angles, which were 0°, 30°, 60° and 90°; benched and unbenched manhole designs were also studied.

The ADZ model results showed that a threshold surcharge level, at which the solute transport characteristics indicated a sharp transition between pre-threshold and post-threshold conditions, was evident in the four unbenched manholes. The threshold level appeared to increase with deflection angle. However, a similar transition in the solute transport characteristics in the

benched manholes was not observed in the analysed ADZ data. No explanation was given by Saiyudthong (2004).

Saiyudthong (2004) concluded that the increase in deflection angle generally resulted in more mixing within the benched and unbenched manholes. Travel time and dispersive fraction increased with deflection angle, while reach time delay varied with deflection angle in a random manner. The increase in mixing with regard to a higher deflection angle was explained by Saiyudthong (2004) that the change in pipe direction deterred a solute from travelling straight through the manhole without undertaking any mixing, and that introduced a greater transfer of tracer between the dead zone and the incoming jet.

An attempt was made by Saiyudthong (2004) to correlate residence time, T (Equation 2.23), and energy loss using Equation 2.32. G is a parameter used in wastewater engineering to determine floc break-up in hydraulic flocculators. Saiyudthong (2004) derived G-values for his manhole using the experimental energy loss and tracer results. However, the parameter appeared to be sensitive to deflection angle, discharge and the design option for benching.

$$G = \sqrt{\frac{g\Delta H}{vT}} \hspace{4cm} 2.32$$

where:

g is the gravitational acceleration

ΔH is the head loss across manhole

T refers to the ADZ residence time

v refers to the kinematic viscosity of the fluid

2.5.2.4 Benching

Benching affects the mixing process in surcharged manholes by restricting the spread of the incoming jet and hence the mixing with the stored water. Dennis (2000) studied the effect of benching in a manhole with $1.5D_p$ step height. His study concluded that with full pipe depth benching, the response of the manhole to the tracer experiments was highly comparable to that of a straight pipe, meaning that the mixing was primarily governed by differential advection. The effects of benching (half pipe depth) were also studied by Saiyudthong (2004) but in the manhole with change in pipe direction. The results of his tracer tests showed that benching generally reduced mixing. However, the reduction in mixing was more significant when the deflection angles were $0°$ and $30°$; and was less when the deflection angles were greater. Saiyudthong (2004) explained that for deflection angles greater than $30°$, the bend of the dry weather flow channel within the manhole might become too sharp and that the incoming flow passed over the channel and mixed with the storage. Therefore, more flow was entrained into

the storage of the manhole when the angles were higher and that promoted more mixing in the chamber (Figure 2.20).
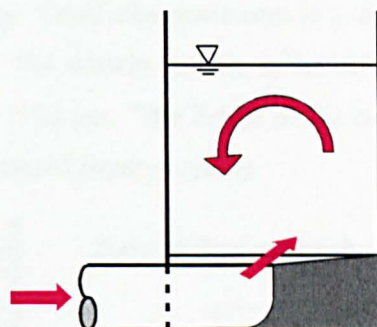
Figure 2.20 – Flow entrainment into the dead zone in a benched manhole with a change of pipe angle greater than 30° (after Saiyudthong, 2004)

2.5.2.5 Higher Order Solute Transport Modelling

Higher order solute transport models have been used to analyse the laboratory manhole traces (Guymer and Dutton, 2007; Saiyudthong, 2004). The aim of these studies was to simulate the skewed downstream distributions with a high accuracy using a more complicated model that can account for dead zone mixing. This is because the first order ADE and ADZ models failed to entirely describe the observed downstream traces, implying that the hydraulics of the system was not fully represented (Guymer and Dutton, 2007; Guymer *et al.*, 2005).

In Guymer and Dutton (2007)'s work, the Hart transient storage (TS) model was employed to re-analyse the traces collected in Guymer *et al.* (2005) and the model showed a more accurate prediction in comparison to the first order ADE and ADZ models. In Saiyudthong (2004)'s study, consideration was given to the two cell technique of the first order ADZ model. A prediction with an excellent goodness of fit to the measured profile was made by the higher order model showing a significant improvement to the single cell ADZ model prediction. Although the higher order solute transport models could provide a better description for the manhole traces, they are not implemented in sewerage system models because of the models' complexity and there are no general rules to link the parameter values to physical properties of the system.

2.5.3 Submerged Jet Theory

Bo Pedersen and Mark (1990) proposed that the hydraulic of surcharge manholes with straight through flow could be represented by submerged jet theory, developed by Albertson *et al.* (1950). The theory proposed that a submerged jet comprises two flow zones, which are zone of flow establishment and zone of established flow (Figure 2.21). In the zone of flow

establishment, there are a core region and a diffusion region. The fluid within the core region is assumed to have constant velocity (U_o) as in the outlet. The width of the core decreases with distance due to lateral mixing. Surrounding the core is a diffusion region with an approximate rate of expansion of 1 in 5. The velocity profile in the diffusion region can be described by a Gaussian normal probability function. The length of the core region is typically 6.2 times the outlet width or diameter, measured experimentally.
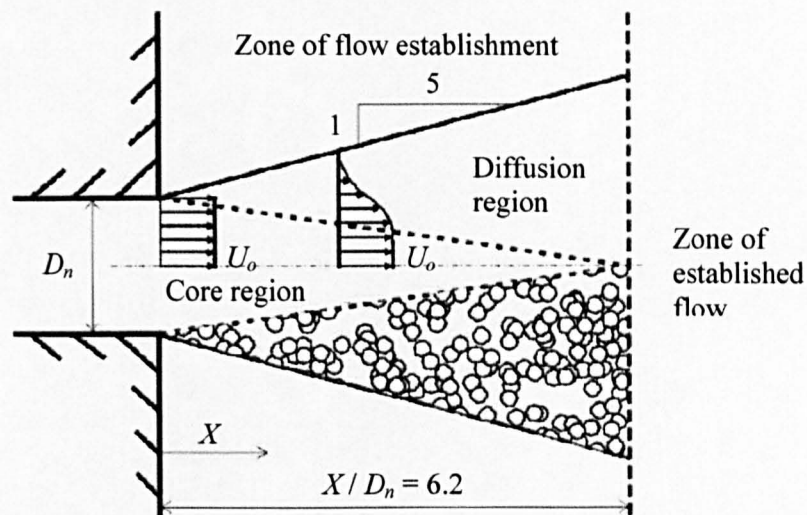
Figure 2.21 – Velocity distribution and diffusion region in three-dimensional circular free jet (after Albertson *et al.*, 1950)

This theory was originally developed for a free submerged jet, i.e. a turbulent jet discharging into a stagnant fluid with infinite boundary. In the case of manholes, the hydraulic characteristics within the chamber may not be truly represented by this theory because the jet is released in a confined space (manhole) in which circulation flows may influence the jet characteristics. In addition, if the invert of the inlet pipe is levelled with the manhole base, the friction effects of the manhole base will affect the properties of the submerged jet near there (Naib, 1992). Nevertheless, submerged jet theory has been successfully applied to describe energy loss and mixing within manholes with straight through flow (Bo Pedersen and Mark, 1990; Mark *et al.*, submitted in 2006). The theory is also generally accepted in manhole research that explains the general flow pattern occurring within manholes. However, at present, there is limited knowledge regarding the validity of submerged jet theory in manholes; for example, the validity of the jet expansion ratio. Velocity measurements within the chamber are needed in order to carry out this verification.

2.5.4 Terms Used in this Manhole Study

This sub-section defines the key terms employed in this manhole study.

Different definitions for surcharge depth exist within the literature. In this study, surcharge, s, describes the water depth measured with respect to the inlet pipe soffit, i.e. the top of the delivery pipe (Figure 2.22). When comparing the results between manholes at different scale, surcharge ratio, S, is used to refer to the ratio of surcharge depth, s, to the pipe internal diameter, D_p.

Threshold depth indicates the surcharge depth at which a transition in the hydraulic and associated phenomena, such as energy loss and mixing, occurs (see example in Figure 2.19). The hydraulic regime emerging at surcharges below the threshold depth is termed pre-threshold; and post-threshold indicates the hydraulic conditions after the transition, above the threshold depth.
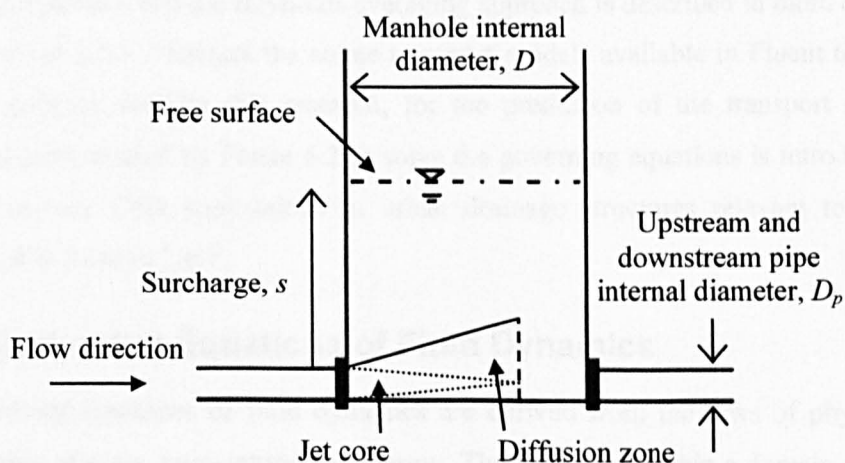
Figure 2.22 – Terminology used in this manhole study

2.6 *Computational Fluid Dynamics*

2.6.1 Introduction

Computational fluid dynamics (CFD) is a computational technique which solves fluid flow, heat transfer and associated phenomena such as chemical reactions within a flow system using numerical equations derived from the laws of physics (Versteeg and Malalasekera, 1995). The fluid body within a flow system, or a domain, requires spatial discretisation (a grid mesh) such that details of the flow within the system can be solved. This technology has been brought into the engineering industry since the 1980's and its application has increased rapidly over the last decade. This can be attributed to the advanced ultra-high speed computer processors and user-friendly commercial CFD packages being available, allowing more complex problems to be

investigated through this technique. CFD is now widely used for research and industrial applications associated with a wide range of fluid flow problems, e.g. aerodynamics of aircraft and automotive; mixing processes in reactor and stirred tanks; flows in river, estuaries and oceans etc. (Shaw, 1995; Versteeg and Malalasekera, 1995).

CFD can be an alternative tool for the investigation of fluid flow problems. For example, once a numerical model is validated, the model can be used to examine the impact of changes to the geometry, scale or flowrate without the need to construct additional physical models. The final solution of the model contains a complete data set of variables over the control volume. It may not be possible to obtain this from physical models or in-situ testing. This demonstrates that CFD may provide benefits in terms of information, time and cost.

The following sub-section describes the fundamental equations of fluid flow that form the basis of all CFD codes. Section 2.6.3 describes the three approaches that can provide solutions to the governing equations and the Reynolds averaging approach is described in more detail in Section 2.6.4. Section 2.6.5 discusses the solute transport models available in Fluent 6.2, which is the software package used in this research, for the prediction of the transport of solutes. The numerical method used by Fluent 6.2 to solve the governing equations is introduced in Section 2.6.6. Previous CFD applications in urban drainage structures relevant to this study are highlighted in Section 2.6.7.

2.6.2 Governing Equations of Fluid Dynamics

The governing equations of fluid dynamics are derived from the laws of physics, which are conservation of mass, momentum and energy. The flow field within a domain can be predicted by solving these governing equations given the correct boundary conditions. The derivation of the governing equations is not presented here but can be found in many fluid dynamics text books, including Chadwick and Morfett (1999) and Versteeg and Malalasekera (1995). Presented in the following sub-sections are the governing equations for a three-dimensional compressible flow. The equations corresponding to the conservation of thermo-energy are excluded in this review as this is not relevant in the present study.

2.6.2.1 Conservation of Mass

Considering an infinitesimal small element of fluid with sides Δx, Δy and Δz (Figure 2.23), the equation for conservation of mass, also called the continuity equation, is derived from the principle:

Rate of increase of mass in fluid element = Net rate of flow of mass into fluid element

This is the mass balance equation for a fluid element and can be numerically expressed as:

$$\frac{\partial \rho}{\partial t} + \left(\frac{\partial \rho u}{\partial x} + \frac{\partial \rho v}{\partial y} + \frac{\partial \rho w}{\partial z} \right) = 0 \qquad \qquad \textbf{2.33}$$

where:

u, v, w are the velocities with respect to x, y, z directions

The first term on the left hand side is the rate of change of density (mass per unit volume) in time and the rest are the convective terms which describe the net flow of mass out of the element across its boundaries. In an incompressible flow, where the density of fluid is constant, the first term and the fluid density in the rest of the terms can be omitted.
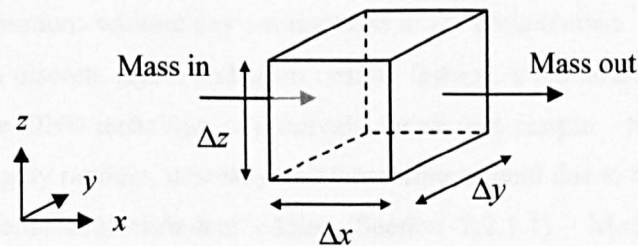
Figure 2.23 – Mixing flux into and out of a control volume

2.6.2.2 Conservation of Momentum

The conservation of momentum equations, commonly called the Navier Stokes (NS) equations, were developed from the principle of Newton's second law which states that:

Rate of increase in momentum of fluid particle = Sum of forces on fluid particle

The original mathematical expression of the conservation of momentum contains viscous stress components of the fluid element. In a Newtonian fluid, whose viscosity is dependent upon temperature and pressure, these viscous stresses can be expressed as functions of the local deformation rate (Versteeg and Malalasekera, 1995). Therefore, the time dependent NS equation of a Newtonian fluid for the x direction can be written as:

$$\frac{\partial(\rho u)}{\partial t} + \frac{\partial(\rho u u)}{\partial x} + \frac{\partial(\rho v u)}{\partial y} + \frac{\partial(\rho w u)}{\partial z} = -\frac{\partial p}{\partial x} + \mu \left(\frac{\partial^2 u}{\partial x^2} + \frac{\partial^2 u}{\partial y^2} + \frac{\partial^2 u}{\partial z^2} \right) + S_{Mx} \qquad \textbf{2.34}$$

where:

p is the static pressure

S_{Mx} is the momentum source term

μ is the dynamic viscosity of the fluid

Similarly, the NS equations for the y and z directions:

$$\frac{\partial(\rho v)}{\partial t} + \frac{\partial(\rho uv)}{\partial x} + \frac{\partial(\rho vv)}{\partial y} + \frac{\partial(\rho wv)}{\partial z} = -\frac{\partial p}{\partial y} + \mu\left(\frac{\partial^2 v}{\partial x^2} + \frac{\partial^2 v}{\partial y^2} + \frac{\partial^2 v}{\partial z^2}\right) + S_{My} \qquad 2.35$$

$$\frac{\partial(\rho w)}{\partial t} + \frac{\partial(\rho uw)}{\partial x} + \frac{\partial(\rho vw)}{\partial y} + \frac{\partial(\rho ww)}{\partial z} = -\frac{\partial p}{\partial z} + \mu\left(\frac{\partial^2 w}{\partial x^2} + \frac{\partial^2 w}{\partial y^2} + \frac{\partial^2 w}{\partial z^2}\right) + S_{Mz} \qquad 2.36$$

2.6.3 Numerical Solutions of the Governing Equations

In theory, a fluid flow in either a laminar or turbulent flow regime can be completely described temporally and spatially by directly solving the continuity and the NS equations. This numerical solution technique is called direct numerical simulation (DNS), which resolves all scale of fluid motions without any assumptions in the computation. In laminar flows, where the fluid travels in discrete layers and in an orderly fashion, a numerical simulation for this type of flow using the DNS technique is relatively quick and simple. In turbulent flows, the fluid motions are highly random, unsteady and three-dimensional due to the extensive range of length scales and lifetimes of turbulent eddies (Section 2.2.1.1). Modelling turbulent fluid flow requires massive storage capacity and ultra high speed computer processors to describe all time-varying eddy motions, including the smallest eddy and the eddy with the shortest eddy lifetime. With current levels of computer technology, this is not perceived to be a practical approach for general engineering application (Awbi, 2003; Rodi, 1993; Versteeg and Malalasekera, 1995).

Computer hardware limitations do not stop turbulent flows from being modelled using CFD. Alternative approaches, which simplify the modelling of turbulence by making assumptions, have been developed. They are the large eddy simulation (LES) technique and the Reynolds averaging technique.

LES is a simplified version of DNS in which large eddies are explicitly resolved in a time dependent simulation using the 'filtered' NS equations. Compared with DNS, the LES technique requires less computational resource and time due to the filtering process incorporated into the time dependent NS equations. The filter removes eddies with a size smaller than the filter size (usually defined as the size of the cell) from being directly resolved and the filtered eddies are simulated by turbulence models for which assumptions, or errors, are always implied. Although less of the turbulence/eddy is required to be resolved, the LES technique still demands huge computational resources for solving time dependent solutions on a reasonably fine mesh. Therefore, this LES approach is not considered for most practical situations.

The Reynolds averaging approach is the least computationally expensive approach among the three. This is because the approach incorporates the greatest number of approximations. Through the Reynolds averaging operation (Section 2.2.1.1) to the original NS equations, the subsequent governing equations, renamed Reynolds averaged Navier Stokes (RANS) equations, only resolve the mean flow quantities, while all terms with fluctuating component are modelled. Without time-dependent variables in the RANS equations, the equations can be solved in steady state, meaning that massive computational time can be saved. Although this approach leads to a loss of the details of turbulence (the eddy motion) in the flow, these are of limited importance to most engineering applications and usually the mean flow properties are the main concern.

2.6.4 Reynolds Averaged Navier Stokes Equations

The Reynolds averaged Navier Stokes (RANS) equations are obtained by substituting Equation 2.2 into Equation 2.34 – Equation 2.36. After re-arrangement, the RANS equation in the x, y and z directions for an incompressible flow is therefore:

$$\rho \frac{\partial U}{\partial t} + \rho U \frac{\partial U}{\partial x} + \rho V \frac{\partial U}{\partial y} + \rho W \frac{\partial U}{\partial z} =$$
$$-\frac{\partial P}{\partial x} + \mu \left(\frac{\partial^2 U}{\partial x^2} + \frac{\partial^2 U}{\partial y^2} + \frac{\partial^2 U}{\partial z^2} \right) - \left(\rho \frac{\partial \overline{u'^2}}{\partial x} + \rho \frac{\partial \overline{u'v'}}{\partial y} + \rho \frac{\partial \overline{u'w'}}{\partial z} \right) \qquad \textbf{2.37}$$

$$\rho \frac{\partial V}{\partial t} + \rho U \frac{\partial V}{\partial x} + \rho V \frac{\partial V}{\partial y} + \rho W \frac{\partial V}{\partial z} =$$
$$-\frac{\partial P}{\partial y} + \mu \left(\frac{\partial^2 V}{\partial x^2} + \frac{\partial^2 V}{\partial y^2} + \frac{\partial^2 V}{\partial z^2} \right) - \left(\rho \frac{\partial \overline{u'v'}}{\partial x} + \rho \frac{\partial \overline{v'^2}}{\partial y} + \rho \frac{\partial \overline{v'w'}}{\partial z} \right) \qquad \textbf{2.38}$$

$$\rho \frac{\partial W}{\partial t} + \rho U \frac{\partial W}{\partial x} + \rho V \frac{\partial W}{\partial y} + \rho W \frac{\partial W}{\partial z} =$$
$$-\frac{\partial P}{\partial z} + \mu \left(\frac{\partial^2 W}{\partial x^2} + \frac{\partial^2 W}{\partial y^2} + \frac{\partial^2 W}{\partial z^2} \right) - \left(\rho \frac{\partial \overline{u'w'}}{\partial x} + \rho \frac{\partial \overline{v'w'}}{\partial y} + \rho \frac{\partial \overline{w'^2}}{\partial z} \right) \qquad \textbf{2.39}$$

In Cartesian tensor form, these equations can be re-written more compactly as:

$$\rho \frac{\partial U_i}{\partial t} + \rho U_j \frac{\partial U_i}{\partial x_j} = -\frac{\partial P}{\partial x_i} + \mu \frac{\partial^2 U_i}{\partial x_j^2} - \rho \frac{\partial \overline{u_i' u_j'}}{\partial x_j} \qquad \textbf{2.40}$$

And the continuity equation written in Cartesian tensor form is:

$$\frac{\partial U_i}{\partial x_i} = 0 \qquad \textbf{2.41}$$

The RANS equations (Equation 2.37 – Equation 2.39) share the general form of the original NS equations. Now, the velocities and the pressure are replaced with time average variables. On the right hand side of the RANS equations, there are new terms containing the products of fluctuating velocity components. These new terms describe the convective momentum transfer due to velocity fluctuations and are termed Reynolds stresses. There are six Reynolds stresses, comprising three normal stresses and three shear stresses:

Normal stresses: $\tau_{xx} = -\rho\overline{u'^2}$; $\tau_{yy} = -\rho\overline{v'^2}$; $\tau_{zz} = -\rho\overline{w'^2}$

Shear stresses: $\tau_{xy} = \tau_{yx} = -\rho\overline{u'v'}$; $\tau_{xz} = \tau_{zx} = -\rho\overline{u'w'}$; $\tau_{yz} = \tau_{zy} = -\rho\overline{v'w'}$

According to the principles of Reynolds averaging, the mean of a fluctuating velocity component in Equation 2.2 is always zero. However, in turbulent flows, these Reynolds stresses are always non-zero. This is because the normal stresses contain squared velocity fluctuations and the fluctuating components in the shear stresses are statistically dependent fluctuations. In fact, the turbulent shear stresses are usually very large in magnitude compared with their viscous counterparts (Rodi, 1993; Versteeg and Malalasekera, 1995).

The instantaneous NS equations form a closed set of four equations with four unknowns, u, v, w and p (Equation 2.33 - Equation 2.36). However, after Reynolds averaging, six additional Reynolds stresses are introduced into the set of four equations, and the number of unknowns then outnumber the number of the governing equations. A direct solution to these equations is therefore impossible. This type of problem is called 'the problem of closure'.

To solve the mean properties of a flow, such as velocity and pressure, a numerical model which describes the effects of turbulent fluctuations, i.e. Reynolds stresses, on the mean flow properties is essential. This numerical model governs the accuracy of the flow field solution, particularly when Reynolds stresses are dominant in the momentum equation, while the inertia and pressure terms are far less important (Rodi, 1993). One example, which illustrates the impact that the choice of turbulence model may have on the accuracy of the flow field predictions was presented by Buxton (2003): in the prediction of the turbulence driven secondary motions in a trapezoidal open channel, the standard k-ε turbulence model, which assumes isotropy of turbulent viscosity, failed to produce the inherent secondary flow features. These secondary features were replicated when a more sophisticated Reynolds stress model (RSM) was used. At present, there are two categories of turbulence models commonly used in studying turbulent flows, namely: the eddy viscosity models and the differential second-moment turbulence closure models. Note that the standard k-ε turbulence model is a variant of the eddy viscosity models and the RSM belongs to the second category.

2.6.4.1 Eddy Viscosity Models

Turbulence models within this category, such as the mixing length and k-ε turbulence models, were developed on the basis of the eddy viscosity concept, developed by Boussinesq in 1877. The eddy viscosity concept assumes that, analogous to the viscous stresses in a laminar flow, the Reynolds stresses are proportional to the mean-velocity gradients:

$$\tau_{ij} = -\rho \overline{u_i' u_j'} = \mu_t \left(\frac{\partial U_i}{\partial x_j} + \frac{\partial U_j}{\partial x_i} \right) \qquad \qquad \textbf{2.42}$$

where:

μ_t is the turbulent or eddy viscosity

The turbulent viscosity, in contrast to the molecular viscosity which is a fluid property, is a property of the flow. It is strongly dependent upon the state of turbulence. Therefore, its value varies spatially in a particular flow field. Mathematically, the turbulent viscosity is usually expressed in terms of the kinematic turbulent viscosity, denoted by $v_t = \mu_t/\rho$. It is also commonly assumed that the kinematic turbulent viscosity is directly proportional to the product of a turbulent velocity scale, θ, and a length scale, l (Versteeg and Malalasekera, 1995):

$$v_t = C\theta l \qquad \qquad \textbf{2.43}$$

where:

C is a dimensionless constant

Eddy viscosity turbulence models predict solutions to turbulent flow problems based on Equation 2.42 and Equation 2.43. Models within this category employ different approaches to characterising the turbulent velocity and length scales. For example, the k-ε turbulence model uses sophisticated modelling concepts and techniques to correlate the velocity and length scales to the kinetic turbulent energy and turbulent dissipation rate. However, the underlying assumption of this concept may limit its applicability in a wide range of flows (Rodi, 1993). The eddy viscosity concept assumes isotropy of the turbulence viscosity, implying that the ratio of Reynolds stresses to the mean velocity gradients is constant in all directions. This assumption is invalid in many categories of flow, e.g. turbulence driven secondary flows in non-circular ducts and highly swirling flows, where this type of model may result in inaccurate flow field predictions (Hanjalic and Kakirlic, 2002; Launder et al., 1975; Rodi, 1993).

Further discussion of the eddy viscosity turbulence model only considers the k-ε turbulence models. Details of the other eddy viscosity turbulence models can be found in Rodi (1993) and Versteeg and Malalasekera (1995).

2.6.4.1.1 The k-ε Turbulence Model

The k-ε turbulence model is a sophisticated eddy viscosity turbulence model, which accounts for the effects of transport of turbulence properties by the mean flow and diffusion; and for the production and destruction of turbulence (Versteeg and Malalasekera, 1995). It consists of two equations, one for the turbulent kinetic energy, k, and one for the turbulent energy dissipation rate, ε, to estimate the turbulent viscosity in the flow. In this model, the turbulent velocity scale and length scale are defined in terms of k and ε:

$$\theta = k^{1/2} \tag{2.44}$$

$$l = \frac{k^{3/2}}{\varepsilon} \tag{2.45}$$

Various versions of the k-ε turbulence model have been developed over the past decades. The most popular k-ε turbulence models in the current engineering industry are the standard and the renormalisation group (RNG) k-ε turbulence models. These two models are reviewed in this literature review. A brief introduction of the realisable k-ε turbulence model proposed by Shih *et al.* (1995) is also provided.

2.6.4.1.1.1 The Standard *k*-ε Turbulence Model

This model is the earliest version of the k-ε turbulence model that allows the turbulent velocity and length scales to be independently determined. The numerical equations for k and ε in the standard k-ε turbulence model for an incompressible flow are presented in Equation 2.46 and 2.47. The ε equation, developed by Hanjalic (1970), contains many terms which are immeasurable and not well understood. Significant assumptions have been introduced to the ε equation to model complex correlations whose behaviour is little understood (Rodi, 1993).

$$\frac{\partial k}{\partial t} + U_i \frac{\partial k}{\partial x_i} = \frac{\partial}{\partial x_i}\left(\frac{v_t}{\sigma_k}\frac{\partial k}{\partial x_i}\right) + 2v_t \overline{S_{ij}S_{ij}} - \varepsilon \tag{2.46}$$

$$\frac{\partial \varepsilon}{\partial t} + U_i \frac{\partial \varepsilon}{\partial x_i} = \frac{\partial}{\partial x_i}\left(\frac{v_t}{\sigma_\varepsilon}\frac{\partial \varepsilon}{\partial x_i}\right) + C_{1\varepsilon}\frac{\varepsilon}{k}2v_t\overline{S_{ij}S_{ij}} - C_{2\varepsilon}\frac{\varepsilon^2}{k} \tag{2.47}$$

$$v_t = C_\mu \frac{k^2}{\varepsilon} \tag{2.48}$$

$$\overline{S_{ij}} = \frac{1}{2}\left(\frac{\partial U_i}{\partial x_j} + \frac{\partial U_j}{\partial x_i}\right) \tag{2.49}$$

where:

$\overline{S_{ij}}$ is the main strain rate

ν_t is the turbulent kinematic viscosity

C_μ σ_k, σ_ε, $C_{1\varepsilon}$, and $C_{2\varepsilon}$ are empirical constants and their values were determined from extensive free turbulence flow experiments (Table 2.3). The experimental methodology to evaluate the value of the standard k-ε turbulence model constants is described in Rodi (1993).

C_μ	σ_k	σ_ε	$C_{1\varepsilon}$	$C_{2\varepsilon}$
0.09	1.00	1.30	1.44	1.92

Table 2.3 – Value of the constants used in the standard k-ε turbulence model (Launder and Spalding, 1974)

The standard k-ε turbulence model is considered to be the 'classic' turbulence model and it has been extensively validated in various turbulent flows, including thin shear layer flows, pipe flows, recirculating flows and confined flows, without the need for case-by-case adjustment of the model constants (Grimm, 2004; Rodi, 1993; Versteeg and Malalasekera, 1995). However, weakness of the model has been shown in modelling unconfined flows, weak shear layers (far wakes and mixing layers), swirling flows and axisymmetric jets in stagnant surroundings (Rodi, 1993; Versteeg and Malalasekera, 1995). The limitations of the model led to the development of other versions of the k-ε turbulence model, for example the renormalisation group (RNG) (Yakhot et al., 1992) and realisable k-ε turbulence models (Shin et al., 1995).

2.6.4.1.1.2 The Renormalisation Group k-ε Turbulence Model

The renormalisation group (RNG) k-ε turbulence model, proposed by Yakhot et al. (1992), was derived on the basis of a rigorous statistical technique, called renormalisation group (RNG) theory. This modelling approach describes the effects of the small scale turbulence by means of a random forcing function in the NS equations (Yakhot et al., 1992). Through the RNG procedure, these small scales of motion are systemically removed from the governing equations but their effects are expressed in terms of larger scale motions and a modified viscosity (Versteeg and Malalasekera, 1995). This modelling concept leads to a numerical model with a set of constants different from those in the standard k-ε turbulence model, and additional terms and functions in the transport equations for k and ε (Fluent, 2005). Further details of the RNG model can be found in Yakhot and Orszag (1986) and Yakhot et al. (1992).

The two governing equations for k and ε in the RNG k-ε turbulence model have similar forms to those in the standard model:

$$\frac{\partial k}{\partial t} + U_i \frac{\partial k}{\partial x_i} = \frac{\partial}{\partial x_i}\left(\alpha_k v_t \frac{\partial k}{\partial x_i}\right) + 2v_t \overline{S_{ij} S_{ij}} - \varepsilon \qquad \textbf{2.50}$$

$$\frac{\partial \varepsilon}{\partial t} + U_i \frac{\partial \varepsilon}{\partial x_i} = \frac{\partial}{\partial x_i}\left(\alpha_\varepsilon v_t \frac{\partial \varepsilon}{\partial x_i}\right) + C_{1\varepsilon}^* \frac{\varepsilon}{k} 2v_t \overline{S_{ij} S_{ij}} - C_{2\varepsilon} \frac{\varepsilon^2}{k} \qquad \textbf{2.51}$$

The main difference between the k and ε equations in the standard and RNG models is in the coefficient, $C_{1\varepsilon}^*$. This term functions as a strain-dependent correction which adjusts the value of $C_{1\varepsilon}$ according to the level of strain in the flow; hence, the prediction in rapid strained flows is improved (Fluent, 2005).

$$C_{1\varepsilon}^* = C_{1\varepsilon} - \frac{\eta(1 - \eta/\eta_0)}{1 + \beta\eta^3} \qquad \textbf{2.52}$$

$$\eta = \frac{\left(2\overline{S_{ij} S_{ij}}\right)^{1/2} k}{\varepsilon} \qquad \textbf{2.53}$$

where:

β is a dimensionless constant, equal to 0.012 (Yakhot *et al.*, 1992)

The constants in the RNG model (Table 2.4) were derived analytically using the RNG theory. Some of the constant values are close to the values for the standard k-ε model, which were empirically derived.

C_μ	σ_k	σ_ε	$C_{1\varepsilon}$	$C_{2\varepsilon}$
0.0845	1.39	1.39	1.42	1.68

Table 2.4 – Value of the constants used in the RNG k-ε turbulence model (Yakhot *et al.*, 1992)

In Fluent, additional modelling options are available for users to enhance the prediction accuracy for swirling flows and flows at low Reynolds number. These options introduce new formulations to describe the turbulent viscosity. Detailed description of these additional modelling approaches can be found in the Fluent manual (Fluent, 2005).

The benefit of this model over the standard k-ε turbulence model is that it has been shown to perform better for rapidly strained and swirling flows and can improve the modelling of low Reynolds number flows (Fluent, 2005; Versteeg and Malalasekera, 1995).

2.6.4.2 Differential Second-Moment Turbulence Closure Models

Differential second-moment (DSM) turbulence closure model (also refered to as the Reynolds stress model – RSM), which abandons the eddy viscosity hypothesis, closes the RANS

equations by solving the transport equations separately for each of the Reynolds stresses. This closure scheme provides an exact treatment of the Reynolds stresses, which improves the prediction of the turbulent stress field and its anisotropy (Hanjalic and Jakirlic, 2002). In complex turbulent flows, for example in rotating and swirling flows, stress anisotropy usually plays a crucial role in the turbulence dynamics. Failure to identify these turbulent structures leads to prediction inaccuracy. Among all RANS turbulence models, the RSM model provides the most detail of the turbulent structures in a flow.

The exact transport equation for the turbulent stresses in an incompressible flow without body force and rotation is presented in Equation 2.54. Derivation of the equation is given in Hinze (1959). To obtain a solution for the exact transport equation of the Reynolds stresses, modelling is required and the terms modelled are the turbulent diffusion, pressure-strain and dissipation terms. Of the three terms, the pressure-strain interaction is the most difficult and important term to model accurately (Versteeg and Malalasekera, 1995).

Launder *et al.* (1975) and Rodi (1993) give comprehensive details of the most general models. The literature review provides specific reference to the modelling technique for the pressure strain term.

| Rate of change | Convective transport | Turbulent diffusion | Molecular diffusion |

$$\rho\frac{\partial \overline{u_i'u_j'}}{\partial t} + \rho U_k \frac{\partial \overline{u_i'u_j'}}{\partial x_k} = -\frac{\partial}{\partial x_k}\left[\rho\overline{u_i'u_j'u_k'} + \overline{p(\delta_{kj}u_i'+\delta_{ik}u_j')}\right] + \frac{\partial}{\partial x_k}\left[\mu\frac{\partial}{\partial x_k}\left(\overline{u_i'u_j'}\right)\right]$$

$$-\rho\left(\overline{u_i'u_k'}\frac{\partial U_j}{\partial x_k} + \overline{u_j'u_k'}\frac{\partial U_i}{\partial x_k}\right) + \overline{p\left(\frac{\partial u_i'}{\partial x_j} + \frac{\partial u_j'}{\partial x_i}\right)} - 2\mu\overline{\frac{\partial u_i'}{\partial x_k}\frac{\partial u_j'}{\partial x_k}}$$

2.54

| Stress production | Pressure strain | Dissipation |

2.6.4.2.1 Pressure-Strain Interaction Modelling

The pressure-strain interaction links two distinct physical processes affecting the Reynolds stresses: pressure fluctuations caused by interactions between pairs of eddies; and pressure fluctuations due to the interaction of an eddy with a region of flow of different mean velocity. The overall effects of the pressure-strain interaction are two-fold: it re-distributes energy among the three normal Reynolds stresses so that the normal stresses become more isotropic; and it reduces the Reynolds shear stresses without impacting on the turbulent kinetic energy, k, in a flow (Rodi, 1993; Versteeg and Malalasekera, 1995).

A number of techniques have been developed to model the pressure-strain interactions. The most well known are the linear pressure strain (LPS) model, developed by Launder *et al.* (1975), and the quadratic pressure strain (QPS) model, proposed by Speziale *et al.* (1991).

The linear model proposed by Launder *et al.* (1975) breaks down the pressure-strain interactions into three terms to model separately: a slow pressure-strain term, also known as the return-to-isotropy term; a rapid pressure-strain term; and a wall reflection term which is responsible for the redistribution of normal stresses near the wall. The pressure-strain correlation in the LPS model is assumed to be a linear function of mean velocity gradients with coefficients that depend algebraically on the anisotropy tensor (Speziale *et al.*, 1991); however, the interaction process is known to be non-linear (Hanjalic and Jakirlic, 2002).

The QPS model is a more sophisticated model than the LPS model. It describes the Reynolds stresses in quadratic form (Younis *et al.*, 1996), which improves the prediction of various turbulent flows, including basic shear flows, rotating plane shear, and axisymmetric expansion/contraction (Fluent, 2005). Similar to the linear model, the QPS equation consists of a slow and a rapid pressure-strain terms, which account for the overall pressure-strain interactions. The QPS does not require an additional wall reflection term to describe the wall reflection effects on the Reynolds stresses in the near wall region. This is because its effect has been accounted for in the quadratic equation of the rapid pressure-strain term.

The mathematics for the LPS and QPS models are highly convoluted and therefore are excluded from this literature review. Full coverage of the equations can be found in Hanjalic and Jakirlic (2002); Launder *et al.* (1975); Speziale *et al.* (1991).

2.6.4.3 Near Wall Turbulence Treatment

The presence of a solid boundary in a flow system affects the wall adjacent fluid flow in non-trivial ways (Figure 2.24). In extremely close proximity to the boundary, called the inner sub-layer, turbulent eddies barely exist and the flow is dominated by viscous stress; toward the outer part of the near wall region, called the log-law layer, the effects of viscous stress become insignificant and turbulent stresses play a major role in momentum and heat or mass transfer; between the two layers is the buffer layer, in which turbulent and viscous stresses are of similar magnitude. The high Reynolds number turbulence models, such as the eddy viscosity models and the RSMs, cannot accurately describe the low Reynolds number flows near the wall. Near wall treatments for the viscous affected regions are therefore required.

There are two approaches commonly used to model these complex flow regimes in the near wall region. In the first approach, the near wall flow is not directly resolved but modelled using

semi-empirical wall functions. The wall functions bridge the gap between the wall and the fully turbulent flow region and assume that the velocity profile is logarithmic and the turbulence quantities are either constant or vary linearly with depth in the viscosity-affected regime. In the second approach, the turbulence models are modified to enable the viscous sub-layer and buffer layer to be resolved. The difference between the two approaches is shown graphically in Figure 2.25. Since the near wall model was not considered in this research, further discussion is not provided in this literature review but can be obtained from Launder and Spalding (1974).
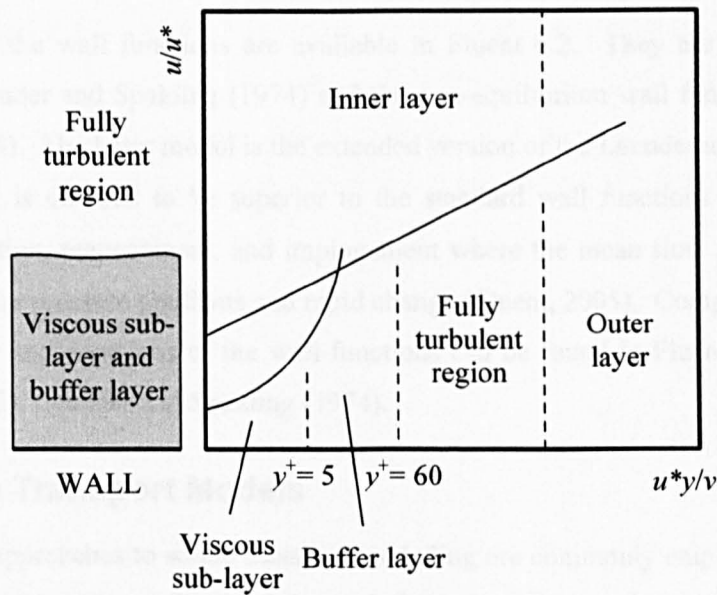
Figure 2.24 – Sub-divisions of the near wall region (after Versteeg and Malalasekera, 1995) ($u*$ is the shear velocity)
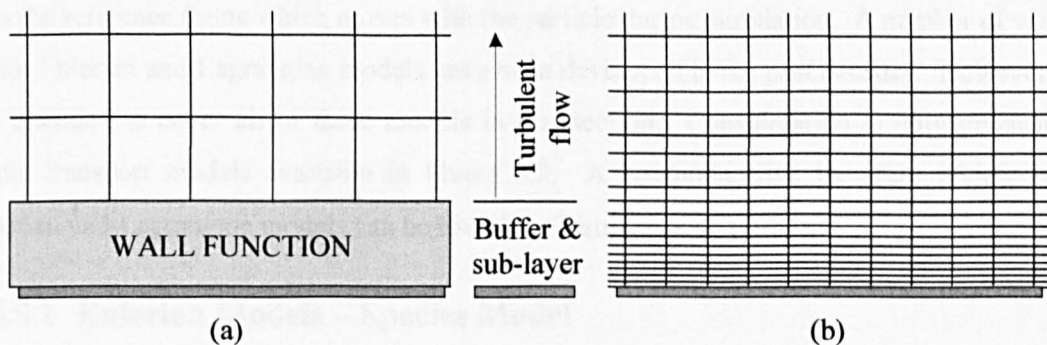
Figure 2.25 – Comparison between the near wall turbulence treatments: (a) the wall function approach, (b) the near wall model (after Fluent, 2005)

There are two benefits to the use of wall functions. Firstly, the computational time is greatly reduced because fewer cells are needed near the wall; secondly, they allow additional empirical information to be considered, such as a wall roughness. One limitation of the wall function

approach is that the centroid of the cell should be located within the log-law layer, $30 < y^+ <$ 300 (Fluent, 2005). y^+ is a non-dimensional distance from wall and is given by:

$$y^+ = \frac{u^* y}{v}$$

2.55

where

u^* is the shear velocity

y is the distance from the wall

Two variants of the wall functions are available in Fluent 6.2. They are the standard wall functions of Launder and Spalding (1974) and the non-equilibrium wall functions of Kim and Choudhury (1995). The latter model is the extended version of the Launder and Spalding's wall functions, which is claimed to be superior to the standard wall functions in complex flows involving separation, reattachment, and impingement where the mean flow and turbulence are subjected to severe pressure gradients and rapid change (Fluent, 2005). Complete description of the methodology and equations of the wall functions can be found in Fluent (2005); Kim and Choudhury (1995); Launder and Spalding (1974).

2.6.5 Solute Transport Models

At present, two approaches to solute transport modelling are commonly employed: the Eulerian and Lagrangian approaches. Each of the techniques employs distinct concepts to simulate solute movement in a flow. The Eulerian approach employs a stationary reference frame and treats the solute phase as a continuum, similar to the way the carrier phase is treated; the other uses the reference frame which moves with the particle during simulation. A number of variants of the Eulerian and Lagrangian models have been developed in the past decades. However, it is not intended to cover all of these models in this section. Consideration is only given to the solute transport models available in Fluent 6.2. A comprehensive literature review of the Eulerian and Lagrangian models can be found in Shirolkar *et al.* (1996).

2.6.5.1 Eulerian Models – Species Model

The species model is one of the solute transport models available in Fluent 6.2. It is based on the advection diffusion equation described in Section 2.4.5.1 and the partial differential equation is solved in a similar fashion to the governing equations of the flow through discretisation:

$$\frac{\partial \bar{c}}{\partial t} + \bar{u}\frac{\partial \bar{c}}{\partial x} + \bar{v}\frac{\partial \bar{c}}{\partial y} + \bar{w}\frac{\partial \bar{c}}{\partial z} = \left(e_m + e_{tx}\right)\frac{\partial^2 \bar{c}}{\partial x^2} + \left(e_m + e_{ty}\right)\frac{\partial^2 \bar{c}}{\partial y^2} + \left(e_m + e_{tz}\right)\frac{\partial^2 \bar{c}}{\partial z^2}$$

2.56

where:

$\bar{c}$ is the time average concentration

e_m is the molecular mass diffusivity

e_{ti} is the turbulent mass diffusivity in the i direction

Solving Equation 2.56 requires the values of the molecular mass diffusivity, e_m, and the turbulent mass diffusivity, e_{ti}. The molecular mass diffusivity, which describes the random Brownian motion, for solutes in water has a typical value of between 0.5×10^{-9} m^2/s and 2×10^{-9} m^2/s (Rutherford, 1994). It is a fluid property and hence is constant over the domain and at various flow conditions. The turbulent mass diffusivity, e_{ti}, is a property of the flow and therefore varies over the domain and flow conditions. The turbulent mass diffusivity can be evaluated via the introduction of the turbulent Schmidt number, Sc_t, (Rodi, 1993):

$$e_{ti} = \frac{v_t}{Sc_t}$$

                                                                         2.57

where:

v_t is the turbulent kinematic viscosity

For an accurate prediction of solute transport using the species model, a good knowledge of the turbulent Schmidt number is necessary. Extensive work on the determination of the turbulent Schmidt number has been carried out over the past 20 years. The research has considered different flow situations, including pipe flows (Hinze, 1975), flows over a flat plate (Koeltzsch, 2000) and open channel flows (Shiono and Feng, 2003). However, the value of the variable appeared to be a function of the nature of the flow and of molecular properties (Goldman and Marchello, 1969; Launder, 1976). For example, Hinze (1975) determined a value of 0.625 for the turbulent Schmidt number in the core region of turbulent pipe flows, while Launder (1976) suggested that a value of 0.7 was more appropriate. Launder (1976) and Shiono and Feng (2003) also commented that the value of the parameter varied in the range of 0.5 to 1.0 between experiments for different flow types and conditions. Koeltzsch (2000) demonstrated in an air flow measurements over a flat plate that the turbulent Schmidt number does not only vary over flow types and flow conditions, it also has a strong dependence on the position within the boundary layer.

The default value for the turbulent Schmidt number in Fluent is 0.7. The value may need re-adjustment in order to correctly describe the turbulent solute dispersion in a flow.

The species model has been widely used in the chemical engineering industry, modelling engine combustion, reaction and mixing. Hydraulic engineers and researchers have also employed the species model to solve hydraulic engineering problems. Grimm (2004) investigated solute

transport in a straight pipe using the species model. The same technique has been applied to model solute dispersion in a storage tank (Stovin *et al.*, in press). Further discussion of these studies is presented in the following sub-section.

2.6.5.2 Lagrangian Models – Particle Tracking Model

The particle tracking model provides an alternative approach to modelling solute transport. This computational technique works by assuming the tracer can be represented by a large number of discrete particles that are each subjected to advection and dispersion. The particle trajectory in a continuum is determined by solving the force balance equation on the particle. The particle acceleration is correlated to the drag force, gravitational force and other forces acting on the particle. The force balance on a particle in the x direction may be written as:

$$\frac{\partial u_p}{\partial t} = F_D(u - u_p) + \frac{g(\rho_p - \rho)}{\rho_p} + F_x \qquad \qquad 2.58$$

where:

F_D is the drag force

F_x is other forces such as Brownian force

g is the gravitational acceleration

u is the instantaneous fluid velocity

u_p is the particle velocity

ρ_p is the density of the particle

The first component on the right hand side of Equation 2.58 corresponds to the particle inertia force. The drag force, F_D, can be generally expressed as (Fluent, 2005):

$$F_D = \frac{18\mu_f}{d_p^2 \rho_p} C \qquad \qquad 2.59$$

where:

C is the correction factor

d_p is the particle diameter

μ_f is the molecular viscosity of the fluid

Equation 2.59 can be applied in a wide range of flow conditions and particle conditions, such as high Mach number flows, sub-micron particle and any particle shapes, provided an appropriate correction factor, C, is applied. In neutrally buoyant solute transport studies, the size of the particle that leads to 'particle size independent' solutions is 1 micron diameter (Grimm, 2004). Therefore, the correction factor, C, is given by:

$$C = \frac{C_D \, \text{Re}_p}{24}$$ 　　　　　　　　　　　　　　　　　　　　　**2.60**

For smooth spherical particles, the drag coefficient, C_D, becomes a function of the particle Reynolds number, Re_p, and three constants, a_1, a_2 and a_3 (Morsi and Alexander, 1972):

$$C_D = a_1 + \frac{a_2}{\text{Re}_p} + \frac{a_3}{\text{Re}_p{}^2}$$ 　　　　　　　　　　　　　**2.61**

Based on a time average flow field solution, the particle tracking equation (Equation 2.58) can only predict the mean particle trajectory. The turbulent dispersion of particles is modelled using an additional sub-model incorporated into Equation 2.58 to account for the random turbulent fluctuations. In Fluent, there are two sub-models which can be utilised to model turbulent dispersion. The first sub-model, called the stochastic tracking process, attempts to generate turbulent eddies in the carrier phase, based upon the local turbulent field associated with a Gaussian probability distribution. The second approach, called the particle cloud model, transports the particles about a mean trajectory and the concentration of the particles within the cloud is represented by a Gaussian probability density function about the cloud centre. Since the particle cloud model was not used in this study, further details of the model may be found in Baxter and Smith (1993), Fluent (2005), Litchford and Jeng (1991) and Jain (1995). Note that the particle cloud model could not generate retention time distributions of a flow system, which is of the interest of this research.

2.6.5.2.1 The Stochastic Tracking Process

To model turbulent dispersion in the stochastic tracking process, particles are tracked by continuous succession of turbulent eddies superimposed on the mean flow of the fluid phase (Adeniji-Fashola and Chen, 1990). Each eddy has its own characteristics which can be expressed by Gaussian distributed random velocity fluctuations, u', v' and w', and an eddy lifetime, τ_e. The random velocity fluctuation can be defined as the square root of the normal Reynolds stress associated with a normally distributed random number, ζ, for example:

$$u' = \zeta \sqrt{\overline{u'^2}}$$ 　　　　　　　　　　　　　　　　　　　　　**2.62**

If the flow field is solved by the k-ε turbulence models which assume isotropic turbulence, the value of the fluctuating velocity can be estimated from the turbulent kinetic energy, k, computed in the mean flow field:

$$\sqrt{\overline{u'^2}} = \sqrt{\overline{v'^2}} = \sqrt{\overline{w'^2}} = \sqrt{\frac{2k}{3}}$$ 　　　　　　　　　**2.63**

For anisotropic turbulence model, such as the RSM, the fluctuating velocity can be directly extracted from the computed Reynolds stresses:

$$u' = \sqrt{\overline{u'^2}}; \quad v' = \sqrt{\overline{v'^2}}; \quad w' = \sqrt{\overline{w'^2}} \qquad \textbf{2.64}$$

The characteristic eddy lifetime determines the time at which the eddy dissipates or changes its properties. The time scale can be defined as a constant:

$$\tau_e = 2T_L \qquad \textbf{2.65}$$

where

T_L \qquad is the integral time or the fluid Lagrangian integral time and can be written as:

$$T_L = C_L \frac{k}{\varepsilon} \qquad \textbf{2.66}$$

where

C_L \qquad equals 0.15 for the k-ε turbulence models or 0.3 for the RSM (Daly and Harlow, 1970)

In Fluent there is an additional option for choosing random eddy lifetime. The time scale is correlated to the integral time T_L and a uniform random number, r, between 0 and 1 (Equation 2.67). The Fluent manual claims that the random eddy lifetime modelling approach yields a more realistic description of the eddy lifetime (Fluent, 2005). However, this correlation function lacks literature support and has therefore not been used in this study.

$$\tau_e = -T_L \log(r) \qquad \textbf{2.67}$$

The stochastic tracking process also takes account of cross trajectory effect, which results in an early migration of a particle from one eddy to another due to the significant free fall velocity of the particle (Shirolkar, et al., 1996). The transit time of a particle within an eddy can be estimated from the solution of a linearised form of the equation of the motion of the particle (Adeniji-Fashola and Chen, 1990):

$$t_{cross} = -\tau_p \ln\left[1 - \left(\frac{L_e}{\tau_p |u - u_p|}\right)\right] \qquad \textbf{2.68}$$

where:

τ_p \qquad is the particle relaxation time

L_e \qquad is the eddy length scale and can be defined as (Gosman and Ioannides, 1981):

$$L_e = \frac{C_L k^{3/2}}{1.225\varepsilon}$$

<div align="right">2.69</div>

The retention time of a particle in a given eddy is taken as the smaller of the eddy lifetime and the particle eddy crossing time. Once the time is reached, a new value of the normally distributed random number, ζ, is updated and hence a new instantaneous velocity is obtained. Note that when the stochastic tracking process is used, the time step, dt, in Equation 2.58 is determined by the smaller of the retention time of a particle in a given eddy or the maximum allowable time step defined by the user.

The particle tracking model is commonly used in simulating spray combustion systems in chemical engineering. In water engineering, a number of researchers have applied this modelling framework to study sediment transport in CSO storage tanks (Adamsson *et al.*, 2003; Stovin and Saul, 1998) and invert traps (Buxton, 2003). Retention times of a neutrally buoyant solute in hydraulic structures can also be studied using the particle tracking model. Examples can be found in Lau *et al.* (2004), in which the performance of various shaped rectangular storm tanks was evaluated by comparing their retention time and short circuiting parameters; and Grimm (2004), who studied the travel time of a neutrally buoyant solute in a straight pipe.

Grimm (2004) and Stovin *et al.* (in press) have both provided comparisons between the species transport modelling approach and the neutrally buoyant stochastic particle tracking. Their conclusions are that both solute transport models could provide highly comparable downstream concentration predictions. However, the simulation time required by the particle tracking approach to run is significantly shorter than that required by the species model. In addition, careful consideration of the model set-up parameters, such as the selection of temporal and spatial discretisation schemes (discussed later) and time step, is necessary for the species model simulation. The benefit of the species model over the particle tracking approach is the ability to show spatial concentration distributions within the domain. At present, both approaches have been used to study solute transport in hydraulic structures (e.g. Egarr *et al.*, 2005; Lau *et al.*, 2004; Lau *et al.*, 2007; Ta and Brignal, 1998).

2.6.6 Discretisation

The CFD equations which govern the motion of fluids and solute transport, e.g. Equation 2.40 and Equation 2.56, are partial differential equations. These equations are not solvable by computers unless they are transformed into numerical analogues of the equations that the computer can be programmed to calculate through numerical discretisation (Shaw, 1992). Three major techniques are available to perform numerical discretisation for CFD programming: the finite difference method, the finite element method and the finite volume method. These

techniques are based on different set of principles, but the results from each technique should not show significant differences. Comprehensive description of these discretisation techniques can be found in Shaw (1992). The Fluent software utilises the finite volume scheme for numerical computation. Further discussion of discretisation therefore focuses on the finite volume method. A schematic representation of this scheme is provided in Figure 2.26.
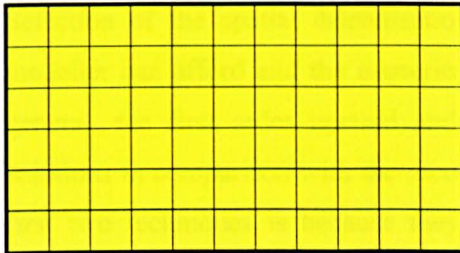
1. The domain is divided up into a grid or mesh of small volumes. The sub-volumes are called grid cells.

2. Each cell has a set of algebraic equations. These equations are obtained from the integration of the governing equations over all the control volumes.

Cell face

Cell centre
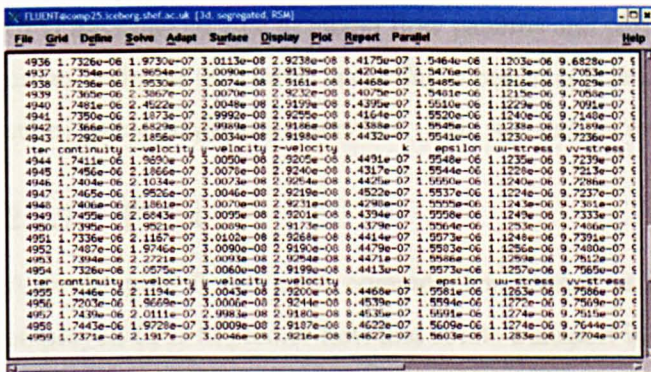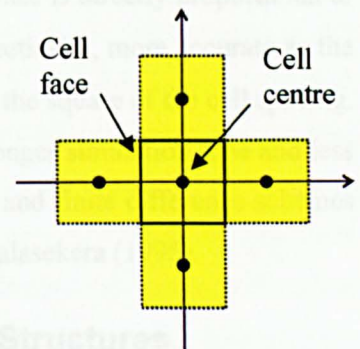
3. The equations are coupled through dependence on values in surrounding cells and on values in other equations; and the solution of the equations is obtained via an iterative calculation process.

Figure 2.26 – Overview of the finite volume scheme for numerical computation

In finite volume based CFD, the fluid properties of a cell, such as velocity, pressure and turbulent quantities, are stored at the cell centre. However, face values are required for the calculation of the governing equations and must be interpolated from the cell centred values. The interpolation is achieved through a finite difference scheme (in Fluent called spatial discretisation scheme). There are a number of spatial discretisation schemes developed for obtaining a solution, for example first and second order upwind, power law and QUICK. The first order upwind scheme is the most basic of the finite difference schemes as it assumes the face values is identical to the upstream cell centred value. The power law scheme interpolates

face values from the cell centre using the solution to a one-dimensional convection diffusion equation (Patankar, 1980). The second order upwind scheme calculates each face value from a Taylor series expansion of the cell centred solution about the cell centroid (Barth and Jespersen, 1989). The QUICK scheme is based on a weight average of second order upwind and central interpolations of the variable (Leonard, 1979).

Selection of the spatial discretisation scheme is based on the computational time that the modeller can afford and the numerical accuracy of the solution required by the modeller. In general, the first order upwind and power law should generate quicker but less accurate solutions in comparison with the second order upwind and QUICK. The lower accuracy of the first two techniques is because they are only first order accurate due to the Taylor series truncation error. The truncation error for first order accurate schemes is directly proportional to the cell spacing. The second order upwind and QUICK are, theoretically, more accurate as the truncation error for these approaches has a linear relationship with the square of the cell spacing. However, the drawback of the second order accurate schemes is longer simulation time and less computational stability. Further information of the discretisation and finite difference schemes can be found in Fluent (2005); Turnbull (2003); Versteeg and Malalasekera (1995).

2.6.7 Previous CFD Studies in Urban Drainage Structures

CFD has been utilised to model flow patterns and particle/solute movement through a variety of urban drainage structures, including pipes, manholes, storage tanks, CSOs, sewer invert traps, storm tanks, ponds and reservoirs. This sub-section reviews the previous CFD-based studies.

2.6.7.1 Pipes

A sewer pipe is the most common component in urban drainage systems. Grimm (2004) employed CFD to predict flow and solute transport in a straight pipe. Rigorous validation work was conducted to verify the flow field and solute transport predictions using published laboratory data. Through the validation work, he found that the flow field and solute transport predictions, especially the turbulence quantities (k, ε and v_t) and solute turbulent dispersion, were sensitive to the choice of the model set-up parameters, such as grid arrangement, selection of spatial discretisation scheme and turbulence model; and temporal discretisation scheme and time step when time dependent solution is used.

In his validated model, the numerical predictions showed good agreement with the published flow field and solute transport data. A general modelling guideline of model set-up parameters for simulation of solute transport in engineering structures was proposed. This modelling

guideline is very useful as one main problem with CFD application in the simulation of hydraulic structures is the lack of standard modelling protocols (Stovin *et al.*, 2002).

2.6.7.2 Manholes

Manholes form the second most common component in sewerage networks and during surcharge conditions their hydraulic behaviour is different from that during dry weather flow. CFD was used by Asztely and Lyngfelt (1996) to predict energy loss in a benched manhole under surcharged conditions. A number of simplifications to the manhole geometry were made in the study, which included modelling only half of the manhole using a symmetry plane on the vertical plane at the pipe centreline and simulating the free surface using a fixed lid approximation. The standard k-ε turbulence model was used for the flow field prediction and a good correlation was shown between the CFD predictions of energy loss coefficient and the laboratory measurements published by Lindvall (1984). Dennis (2000) and Saiyudthong (2004) also utilised the standard k-ε turbulence model to predict the flow field and energy loss within step manholes and manholes with change in pipe direction respectively. However, their studies concluded that the computed energy loss coefficients were consistently smaller than their laboratory results. This might be because thorough consideration of the model set-up parameters, such as meshing technique and grid resolution, selection of spatial discretisation scheme and turbulence model, was not made during the generation of the CFD models. Note that consideration of the use of CFD for solute transport predictions was not given in Dennis (2000) and Saiyudthong (2004).

2.6.7.3 Storage Chambers

Storage chambers play an important role in urban pollution management by reducing the number and magnitude of CSO spill events. A number of CFD-based studies have been performed to develop a generic modelling methodology for this type of structure and to apply the methodology developed to evaluate the performance of storage chamber with different geometrical configurations. Stovin (1996) employed CFD to predict flow patterns and retention efficiency of sediments in a storage chamber. Laboratory validation flow field data was collected and the comparisons of the predicted and measured flow fields showed reasonable agreement. Two modelling approaches to predicting retention efficiency were suggested by Stovin (1996). One approach was based on the concept of a critical bed shear stress for deposition. The bed shear stress was obtained from the flow field solutions. The other approach used the particle tracking model, with default model boundary conditions, to obtain a statistical distribution of sediment destinations. The two approaches were employed to examine the differences in the retention efficiency arising from a number of geometric and hydraulic

configurations. Further work was undertaken by Stovin *et al.* (1999) to use the particle tracking model for the predictions of the gross solids separation efficiency in six different full scale storage chambers. Building upon the work of Stovin (1996), Adamsson *et al.* (2003) developed a user-defined boundary condition, based on bed shear stress, for the particle tracking model to determine the destination of particles in a storage chamber. The revised boundary conditions reflected a more realistic condition under which particles are likely to settle. The comparison between measured data and the numerical prediction showed that the revised boundary condition was superior to the standard options.

2.6.7.4 Combined Sewer Overflows

Combined sewer overflows (CSOs) are an integral component of combined sewerage systems, which limit the flow to treatment to a maximum level and discharge the excess to a nearby watercourse. Harwood (1999) used the RSM to simulate the complex three-dimensional flow structures in a Storm King hydrodynamic separator CSO. The particle tracking model was employed to determine the retention efficiency of the hydraulic structure. The flow field and retention efficiency results were compared with the laboratory measurements from a full scale physical model and the study demonstrated that the CFD models replicated both the swirling flow pattern and the retention efficiency. In a similar study, Tyack and Fenner (1999) conducted a CFD study to predict the flow field in a Grit King hydrodynamic separator. The RNG k-ε turbulence model was employed and the predictions from this model showed good agreement with the experimental velocity data. Egarr *et al.* (2005) presented a CFD numerical model for a hydrodynamic vortex separator. They used the RSM in conjunction with a modified species model to predict the residence time distributions of the hydraulic structure and the mean travel time predictions matched the experimental data.

2.6.7.5 Sewer Invert Traps

Sewer invert traps are used in urban drainage systems to collect the sediments carried by the sewage and minimise the amount of undesired deposition in the sewers. Buxton (2003) conducted a study which aimed to develop a CFD modelling approach for the prediction of the sediment retention performance of invert traps. The numerical predictions were compared with laboratory PIV flow field data and sediment trapping performance results. The study demonstrated that the choice of turbulence model dramatically affected the predictions of the secondary circulations in a trapezoidal channel, and that the sediment retention performance was highly sensitive to the choices for set-up parameters of the particle tracking model.

2.6.7.6 Storm Tanks

Storm tanks are designed to store excess storm water during storm events and clarify the stored water before it is discharged into a natural watercourse. Kluck (1997) employed CFD to develop design methods for this hydraulic structure to achieve optimum performance for solids removal. Ta (1999) considered a time dependent flow simulation in a rectangular storm tank using CFD. The work examined the retention efficiency of suspended particles with a range of particle sizes using the particle tracking approach; and the concentration distribution of dissolved solid in the structure using the species model. Lau *et al.* (2004) created a number of two-dimensional CFD models to evaluate the hydraulic performance of storm tanks with different geometrical configuration by comparing their retention time and short circuiting parameters. The retention time distribution was predicted using the particle tracking model.

2.6.7.7 Ponds and Reservoirs

A number of studies have employed CFD to model flow patterns and tracer movement in large volumes of enclosed water such as reservoirs (Ta and Brignal, 1998), ponds (Shilton, 2000; Wood *et al.*, 1998) and lagoons (Salter *et al.*, 2000). These studies were initiated because of concerns about the operating performance, usually in respect to short circuiting effects. The use of CFD in these studies has gained insights into the hydraulic residence time characteristics of these structures. However, the lack of validation data and the poor reporting of the modelling procedure have limited these studies.

2.7 Tracer and Flow Field Measurement Techniques

2.7.1 Introduction

Dye tracing, laser induced fluorescence (LIF) and particle image velocimetry (PIV) were employed in the laboratory experiments of this research. This section provides a brief introduction to the principles of these laboratory measurement techniques.

2.7.2 Fluorescence

Fluorescence is a quantum mechanical interaction between electromagnetic radiation and electrons of a fluorescent molecule (Schlicke, 2001), in which the molecule absorbs photons and emits photons with a longer wavelength. There are many natural and synthetic compounds that exhibit fluorescence and this photochemical characteristic of compounds has a wide range of applications in biotechnology research and flow measurements. This literature review only focuses on the fluorescence applications in flow measurements. Coverage of fluorescence applications in biotechnology can be found in Lakowicz (2006).

2.7.2.1 Fluorescence Applications in Flow Measurements

Typical fluorescence applications in flow measurements include dye tracing and planar laser induced fluorescence (LIF). Both applications rely on the characteristic of fluorescence that under certain conditions fluorescence is proportional to concentration of a fluorescent matter (Arcoumanis *et al.*, 1990).

2.7.2.1.1 Dye Tracing

Dye tracing is a measure of concentration of the tracer, and will, in effect, be the measure of the concentration of the element of fluid in a fluid flow and of its dispersion characteristics (Kilpatrick and Wilson, 1982). The results are usually presented in the form of temporal concentration profiles which define the dye response. Dispersion characteristics are quantified based on the temporal concentration profiles and solute transport models, such as the ADE and ADZ models. In water engineering, dye tracing is a useful tool for the measurement of travel time and dispersion of a solute in a fluid flow.

The dye tracing information represents the overall fluid behaviour but does not give any detail at a microscopic scale, for example the internal flow field (Wood *et al.*, 1995). Temporal concentration profiles or the model coefficients, such as dispersion coefficient and dispersive fraction, are not able to picture the fluid dynamics of the flow. This is the limitation of this approach and the reason why the fundamental validation of a CFD model requires quantitative flow field data.

Temporal concentration profiles of a tracer in a fluid flow can be measured using filter fluorometers. The basic structure of filter fluorometers is illustrated in Figure 2.27. A filter fluorometer provides a particular range of wavelengths through the energy source, usually a UV lamp, associated with a primary filter for the excitation of the tracer. Emitted fluorescence passes through a secondary filter, which removes any original light source, before reaching a sensing device that converts fluorescence to an electrical signal. Since the instrument only gives a relative measure of the intensity of fluorescence emitted by the tracer contained in a sample, determination of tracer concentrations is based on calibration (Wilson *et al.*, 1986). Turner Design Model 10 Series fluorometers, SCUFAs and Cyclops are the common filter fluorometers used for dye tracing (http://www.turnerdesigns.com).

6. Readout device

5. Sensing device

1. Energy source

4. Secondary filter

2. Primary filter

90°

3. Sample
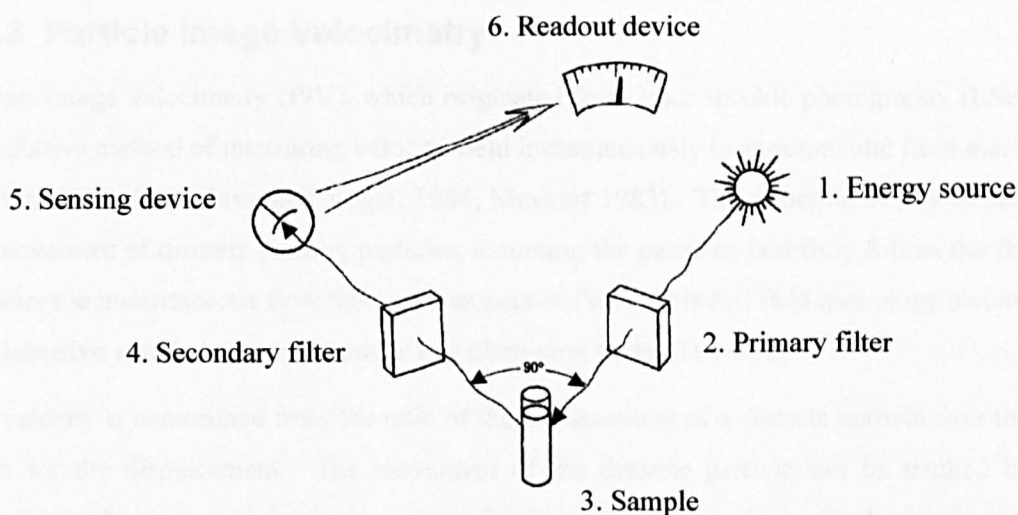
Figure 2.27 – Basic structure of most filter fluorometer (after Wilson *et al.*, 1986)

2.7.2.1.2 *Planar Laser Induced Fluorescence*

Planar laser induced fluorescence (LIF) is a non-intrusive technique to visualise temporal and spatial tracer concentration distributions on a two-dimensional plane. The advantage of this technique over dye tracing is that this measurement approach provides detail of the internal fluid dynamics and/or solute transport processes within a flow.

The principle of planar LIF is similar to that of a filter fluorometer. The detection of concentration depends upon the intensity of light emitted from an excited fluorescent substance after illumination by a laser light sheet. The intensity of fluorescence is proportional to the incident light intensity and the concentration of the fluorescent substance in a flow (Webster *et al.*, 2003). Therefore, concentration can be determined via calibration. In practice, a laser coupled with a light sheet generation device is employed to illuminate a plane in a flow and a camera to record a series of LIF images for subsequent analysis of the temporal and spatial distributions of the excited fluorescent substance. A typical laboratory configuration required for LIF experiments is similar to that for PIV experiments (Figure 2.28). Note that the acronym 'LIF' means 'planar LIF' in this thesis.

LIF studies can provide insights into the mechanisms of solute transport in the dead zone/flow zone boundary layer (Guymer and Harry, 1996). Useful data, such as the rate of mass exchange between the two zones, can be extracted to validate the transient storage ADE models (Purnama, 1988; Valentine and Wood, 1977; Yagi, 1984). LIF is also a useful tool for qualitative flow field analysis.

2.7.3 Particle Image Velocimetry

Particle image velocimetry (PIV), which originated from laser speckle photography (LSP), is a quantitative method of measuring velocity field instantaneously in experimental fluid mechanics (Adrian, 1986; Lauterborn and Vogel, 1984; Meynart 1983). The principle of PIV is based on the movement of discrete seeding particles, assuming the particles faithfully follow the fluid, to measure the instantaneous flow field over an area of flow. This full field metrology technique is non-intrusive which does not introduce any disruption to the flow field.

The velocity is determined from the ratio of the displacement of a discrete particle over the time taken for the displacement. The movement of the discrete particle can be tracked by two recording techniques, which are single frame/multi-exposure recording or multi-frame recording. The latter recording technique is most frequently used because of its inherent ability to eliminate directional ambiguity (Raffel *et al.*, 1998). During multi-frame recording, a monochromatic light source, such as a laser light sheet, is required to illuminate the area of interest. A camera is used to record PIV images for subsequent data analysis. A typical PIV set-up is shown below:
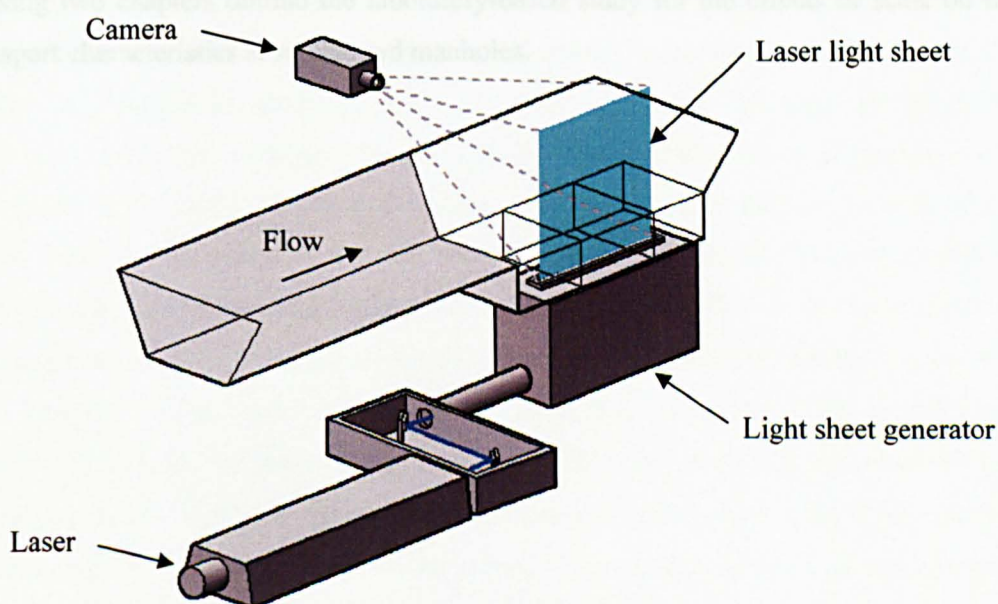
Figure 2.28 – A typical PIV set-up (after Buxton, 2003)

2.8 Summary

Manholes are extensively used in sewerage systems to provide a means of access for inspection and maintenance of sewers. A wide variety of manhole configurations have been examined in laboratory-based experiments to determine the head loss and mixing caused by surcharged manholes. Energy loss coefficients and solute transport model parameters were derived for engineers to design sewerage systems and to model urban drainage networks. However, there is

limited knowledge regarding the scalability of these laboratory scale derived parameters; and, unavoidably, there will be some uncertainty when applying these laboratory scale parameters to full scale manhole structures in real sewerage systems. The aim of this study is to fill in this knowledge gap by investigating the effects of scale on head loss and mixing processes in surcharged manholes.

A CFD-based study provides an alternative approach to laboratory experiments for studying the head loss and solute transport processes at surcharged manholes. This computational approach has a significant advantage over laboratory or field studies that once a numerical model has been validated it may be used to examine the impact of changes to the geometry or flowrate with comparative ease. A number of CFD-based manhole studies (Asztely and Lyngfelt, 1996; Dennis, 2000; Saiyudthong, 2004) were undertaken in the past. However, these studies provided limited information regarding the most appropriate choices for model set-up parameters. Therefore, this research undertook a detailed validation study for flow field and solute transport predictions in manholes.

The following two chapters outline the laboratory-based study for the effects of scale on the solute transport characteristics at surcharged manholes.

3 Laboratory Experiment – Dye Tracing

3.1 Introduction

Longitudinal dispersion due to surcharged manholes has been investigated in the University of Sheffield since the 1990s. Solute transport in a manhole structure has been studied using laboratory-based experiments. To date, the types of manhole that have been studied include manholes with different 'manhole diameter to pipe diameter' ratios (Dennis, 2000; Guymer *et al.*, 2005; O'Brien, 2000), step manholes (Dennis, 2000) and manholes with pipe direction change (Saiyudthong, 2004). This research continues to investigate solute transport within manholes, but focuses on an area which has not been covered in previous manhole studies - the effect of scale on the hydraulics and solute transport characteristics within a manhole structure.

Guymer *et al.* (2005) presented comprehensive data from laboratory experiments on the travel times and dispersion associated with a solute pulse passing through a surcharged manhole. Four manhole diameters (without benching or change in pipe level or direction) were considered over a broad range of flowrates and surcharge depths. Of particular interest in this work was the identification of a threshold surcharge level at which the solute transport characteristics indicated a sharp transition between pre- and post-threshold conditions; at surcharge levels below the threshold the travel times varied linearly with surcharge, whilst above the threshold travel times dropped to a low and constant level. This behaviour has been interpreted as reflecting two distinct hydraulic regimes; pre-threshold the incoming flow mixes throughout the manhole volume, whilst post-threshold the upper volume of fluid within the manhole appears to be cut-off, forming a dead zone which incoming flow passes beneath. This characteristic hydraulic behaviour forms an interesting test for the scale model study. It was observed that manholes with a large 'manhole diameter to pipe diameter' ratio show a more pronounced threshold in comparison to those with smaller ratios. The manhole studied in this research, therefore, is a scale model of the 800 mm internal diameter (ID) manhole, which was the manhole with the largest ratio considered by Guymer *et al.* (2005).

The laboratory study of the scale model took place in two stages. This chapter covers the experimental work carried out during the first stage, which focused on the collection of temporal solute concentration distributions and energy loss data over a spectrum of discharges and surcharge depths. For comparative purposes, similar experiments were conducted in a straight pipe using the same laboratory configuration and similar range of discharges. The laboratory tracer data will be used to investigate the effects of scale in a laboratory-based analysis described in Chapter 4; and will also be used for CFD validation in Chapter 6. Section

3.2 describes the laboratory system in which the experiments were undertaken. The instrumentation used for laboratory data collection and the experimental procedure are documented in Section 3.3. The methodology for data analysis and experimental results are presented in Section 3.4 and 3.5 respectively. Section 3.6 concludes this chapter.

3.2 Laboratory System

3.2.1 Selection of Manhole Scale

The prototype consisted of an 800 mm internal diameter (ID) manhole connected with 88 mm ID Perspex pipes, simulating sewers. Temporal concentration distributions were measured non-intrusively using a Series 10 Turner Design fluorometer in association with an adapter device, developed by O'Brien (2000). The adapter device enlarged the measuring volume of the fluorometer by providing a large black box and a set of reflective mirrors to fit around the 88 mm ID Perspex pipe. However, with this modification the range of concentrations that give linear response was reduced in comparison to that with a standard flow through fluorometer (O'Brien, 2000). As the fluorometer was not originally designed for concentration measurement across a large diameter tube/pipe (greater than 25 mm), the use of the adapter device required an assumption that the concentration measurement would be representative of the average concentration over the entire cross section.

In this study, in order not to use an adapter device on the Turner Design fluorometer for concentration measurement, a 1:3.67 physical scale model of the 800 mm ID manhole (prototype) has been constructed. This geometrical scale was determined by the maximum size (30 mm outer diameter (OD) and 24 mm ID) of the delivery pipe of the scale model that could fit within the fluorometer's original configuration for non-intrusive continuous sampling. The scale manhole model therefore had an ID of 218 mm. Details of the fluorometer arrangement are covered in Section 3.3.4.

Johnston and Volker (1990) suggested that for surcharged manholes, where a free surface exists, Froudian similarity should be used for general hydraulic scaling. The scale model was constructed based on the general principles of Froude number similarity. To obtain the same hydraulic regime as in the prototype, the flow through the scale model was set to be in the fully turbulent region, i.e. Reynolds number (Re) greater than 10,000. Since it was not possible to measure the level of turbulence inside the manhole structure, the level of turbulence in the test section was estimated based on the Reynolds number of the flow in the upstream straight pipe. Table 3.1 summarises the details of the prototype and the scale model.

Configurations and Flow Conditions	Prototype Model	Scale Model
Manhole internal diameter (mm)	800	218
Pipe internal diameter (mm)	88	24
Range of flowrates considered (l/s)	1 – 8	0.25 – 0.50
Minimum flowrate for fully turbulent condition (l/s)	0.789	0.215
Reynolds number of the upstream pipe flow (-)	12,692 – 101,534	11,634 – 23,268
Range of surcharges considered (mm)	0 – 300	0 – 100

Table 3.1 - Summary of the prototype and the scale model

3.2.2 Laboratory Configuration

3.2.2.1 General Arrangement

The scale manhole experimental work used the same laboratory facility as previous manhole studies (Dennis, 2000; O'Brien, 2000; Saiyudthong, 2004). It was a self-contained recirculating system which comprised a constant head tank and a storage sump, from which a submersible pump continuously circulated water through the system. The system had a maximum discharge capacity of 16 l/s and the flowrate through the test section (Figure 3.1) was controlled by a discharge control valve 4 m upstream of the manhole. The test section consisted of two horizontal 24 mm ID Perspex pipes set at a slope of 1:1000 and a 218 mm ID manhole. Discharge through the manhole apparatus was monitored using a Venturi meter installed 1.24 m downstream of the manhole outlet. This measurement device was connected to two 25 mm ID manometers with measurement scales attached. The flow rate measurement system could quantify a range of flowrates from 0.1 l/s to 2.0 l/s with an accuracy to 0.01 l/s. Positioned at the end of the pipe exit was a surcharge control tank. The tank inlet was positioned at a lower elevation, 500 mm beneath the manhole exit. This was to allow sufficient head between the water levels in the manhole and in the surcharge tank such that a complete range of surcharges could be studied. The need for the surcharge tank positioned at a lower elevation is explained as follows: Figure 3.2 shows the minimum surcharge levels in the manhole under free discharge conditions when the pipe and manhole inverts were levelled, i.e. the drop section was disconnected. The minimum surcharge level indicates the head required in the manhole to deliver a given flowrate downstream of the system. It can be observed that energy losses due to pipe friction and the manhole exit are high; without lowering the pipe end, and hence the hydraulic gradient line, it was not possible to generate surcharge levels below 75 mm without risking conditions falling outside of the turbulent flow regime (discharge greater than 0.215 l/s).

After the tank inlet was lowered, the surcharge level raised above 0 mm under free discharge conditions when the flowrate was greater than 0.7 l/s.

The water level in the manhole was controlled by modifying the weir height in the tank. Temporal variations in the free water surface were recorded using a model H45 water level follower (Armfield). This device could measure water level changes of up to 50 mm/s with an accuracy of 0.2 mm. Note that surcharge depth is measured with respect to the pipe soffit.

The straight pipe study employed the same laboratory configuration as Figure 3.1 but with a 24 mm ID straight pipe replacing the manhole.
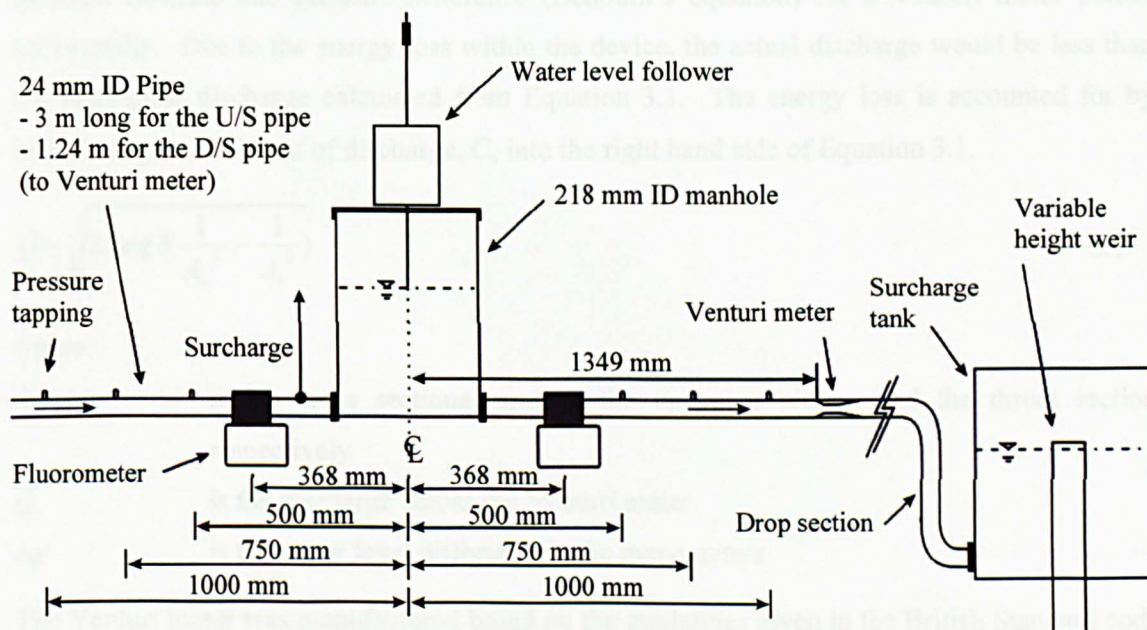
Figure 3.1 – Experimental Configuration
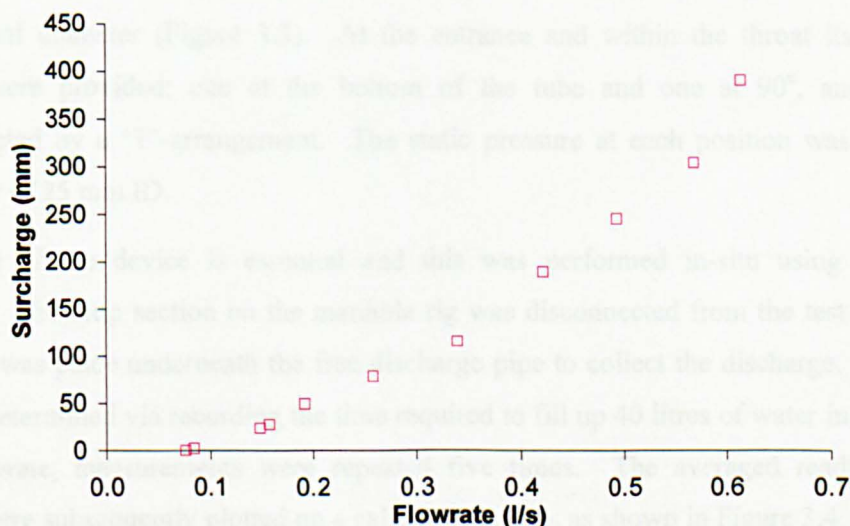
Figure 3.2 – Relationship between minimum surcharge level and flowrate under free discharge conditions (without the drop section)

3.3 Instrumentation and Data Collection

3.3.1 Instrumentation for Flowrate Measurement

A Venturi meter was utilised for flowrate measurement within the laboratory system. This device is characterised by a narrowed section (also called a throat) tapering out to the pipe diameter at each end. As a result of the geometrical change within the device, a pressure difference is created which, in conjunction with the characteristics of the fluid and geometry of the device, enables the flowrate to be estimated. Equation 3.1 shows the theoretical relationship between flowrate and pressure difference (Benoulli's equation) for a Venturi meter placed horizontally. Due to the energy loss within the device, the actual discharge would be less than the theoretical discharge calculated from Equation 3.1. The energy loss is accounted for by introducing a coefficient of discharge, C, into the right hand side of Equation 3.1.

$$Q = \sqrt{2\Delta p g /(\frac{1}{A_2^2} - \frac{1}{A_1^2})}$$
3.1

where:

A_1, A_2	is the cross sectional area at the upstream section and the throat section respectively
Q	is the discharge across the Venturi meter
Δp	is the water level difference in the manometers

The Venturi meter was manufactured based on the guidelines given in the British Standard code (BS EN ISO 5167-1:2003). It was made of Perspex and shaped by machining. The tube converged from a 24 mm ID section to a 17 mm ID throat section and tapered out gently to the pipe internal diameter (Figure 3.3). At the entrance and within the throat itself, two wall tappings were provided; one at the bottom of the tube and one at 90°, and these were interconnected by a 'T'-arrangement. The static pressure at each position was gauged by a manometer of 25 mm ID.

Calibration of the device is essential and this was performed in-situ using a volumetric technique. The drop section on the manhole rig was disconnected from the test section and a large tank was place underneath the free discharge pipe to collect the discharge. The flowrate was then determined via recording the time required to fill up 40 litres of water in the tank. For every flowrate, measurements were repeated five times. The averaged readings for each flowrate were subsequently plotted on a calibration curve, as shown in Figure 3.4. The equation describing the calibration curve is displayed in Table 3.2. Discharge coefficients for Venturi

meters can be estimated by Equation 3.2 (BS EN 24006:1993). For this small scale Venturi meter, it approximates to 0.958.

$$C = \frac{Q\sqrt{\rho\left(1 - \beta^4\right)}}{\frac{\pi}{4}D_p^2\sqrt{2\Delta p}}$$

3.2

where:

D_p is the pipe internal diameter or the internal diameter of the converging section

β is the internal diameter ratio of the throat to the upstream pipe

ρ is the density of the fluid, i.e. water

Throat section
- 17 mm ID

Converging section
- 24 mm ID

Flow direction
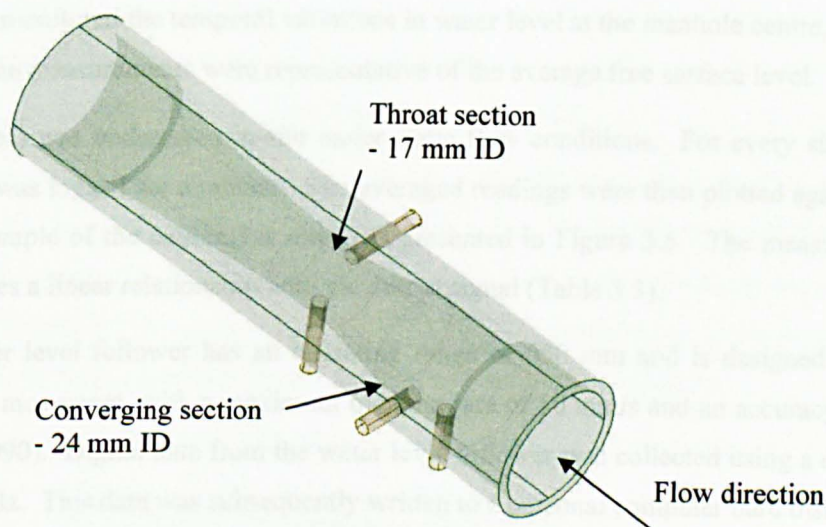
Figure 3.3 – Isometric view of the Venturi meter
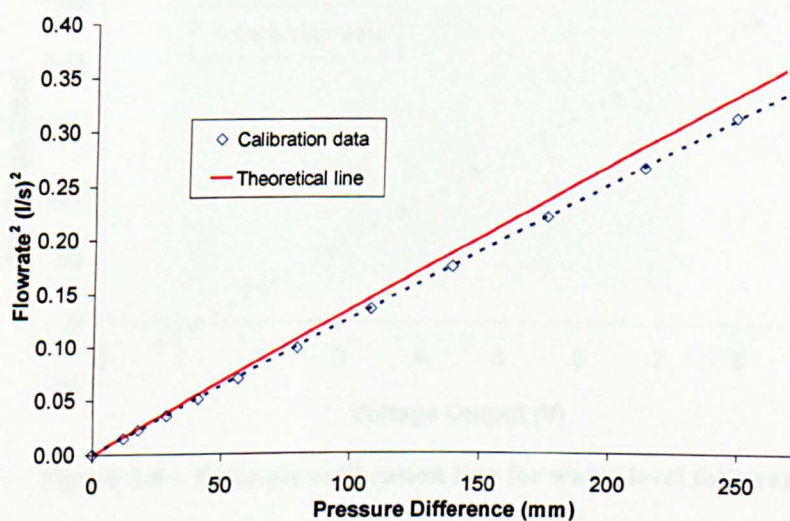
Figure 3.4 – Calibration of the Venturi meter

Equation (through the origin)	R_t^2
$Q^2 = 1.2572 \times 10^{-3} \times \Delta p$	0.9999

Table 3.2 – Equation describing the calibration equation of the Venturi meter

3.3.2 Instrumentation for Water Level Measurement

Temporal variations in free surface level during the steady state experiments were monitored using a model H45 water level follower, manufactured by Armfield Limited. The instrument recorded water level in terms of a digital signal and the actual surcharge depth was determined via calibration. Owing to space constraints, only one follower could be fitted on top of the manhole. The probe monitored the temporal variations in water level at the manhole centre, and it was assumed that the measurements were representative of the average free surface level.

The calibration process was undertaken in-situ under static flow conditions. For every single water level, the data was logged for a minute. The averaged readings were then plotted against water depth. An example of the calibration results is presented in Figure 3.5. The measured surcharge demonstrates a linear relationship with the output signal (Table 3.3).

The model H45 water level follower has an operating range of 650 mm and is designed for tracking gentle water movement, with a maximum tracking rate of 50 mm/s and an accuracy to 0.2 mm (Armfield, 1990). Digital data from the water level follower was collected using a data logger logging at 50 Hz. This data was subsequently written to a personal computer hard disk.
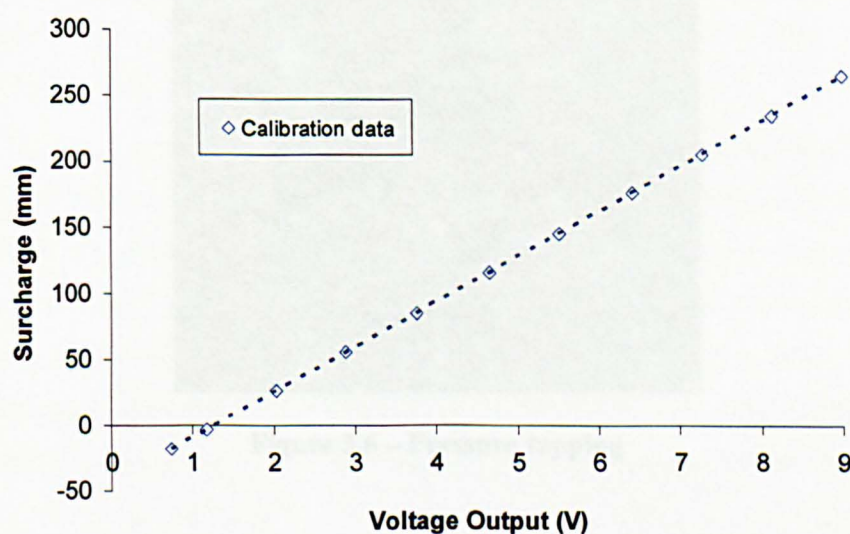
Figure 3.5 – Example calibration line for water level follower

Equation (through the origin)	R_t^2
Surcharge $= 34.28 \times$ Output $- 42.87$	1

Table 3.3 – Equation describing the calibration equation of the water level follower

3.3.3 Instrumentation for Head Loss

Head loss was measured in both the straight pipe and the manhole studies by means of six pressure tappings attached along the length of the delivery pipes. In the manhole study, the six tappings were installed at 500 mm, 750 mm and 1,000 mm upstream and downstream from the centre of the manhole (Figure 3.1). The closest downstream tapping point to the manhole approximated to 16 pipe diameters (IDs) downstream of the manhole outlet, at which point it would be expected that a fully turbulent flow profile would have re-established. The generally accepted minimum distance is 10 pipe diameters (IDs) (Howarth, 1985).

A pressure tapping comprised a 30 mm long steel tube of 2 mm ID held firmly by a Perspex collar (Figure 3.6). The steel tube connected the pipe to a 5 mm ID flexible pipe which was connected to a stilling column. The stilling columns were 88 mm ID, with a measurement scale that could be read to an accuracy of 1 mm. Note that all flexible pipes connected to the pressure tappings were of the same length and were de-aired before any readings were taken.

In the straight pipe study, pressure measurements were undertaken at similar locations.

Figure 3.6 – Pressure tapping

3.3.4 Instrumentation for Longitudinal Dispersion Measurement

Longitudinal dispersion in the surcharged manhole was studied by means of fluorometry. This approach was selected primarily because of the experience and equipment held by the Department of Civil and Structural Engineering Department at the University of Sheffield. This technique was used in previous manhole studies (Dennis, 2000; Guymer and O'Brien, 2000; Guymer et al., 2005; O'Brien, 2000; Saiyudthong, 2004) where it had been successfully used to measure the temporal solute concentration distributions with high levels of confidence.

To determine travel time and longitudinal dispersion within a manhole, the laboratory system requires measurement of temporal concentration profiles of a fluorescent tracer at two sites. The two sampling sites in the scale model were positioned at 368 mm either side of the centre of the manhole (see Figure 3.1). This distance was determined from geometrical scaling of the manhole prototype. In the straight pipe study, monitoring was undertaken at the same locations.

Turner Design Series 10 fluorometers were used for the measurement of temporal solute concentration distributions. The instrument was slightly modified to allow the 30 mm outer diameter, (24 mm ID) Perspex pipe to fit the instrument's original configuration for non-intrusive continuous sampling (Figure 3.7). The dye chosen for tests was Rhodamine WT. This dye was developed specifically for dye tracing studies and is inherently neutrally buoyant in water, conservative in natural environments, resistant to absorption, detectable in low concentration, readily available and economic (Smart and Laidlaw, 1977). The Turner Designs fluorometers are highly susceptible to interference from extraneous light that may intrude into the sampling section. As a result, all pipework and the manhole were fully enclosed with wooden black-out boxes.

The Turner Design fluorometer measures the concentration of a fluorescent material in terms of the intensity of fluorescence or re-emitted light. Inside the fluorometer, a mercury lamp provides a broad range of light wavelengths acting as an excitation source. For the fluorescent material used, a 10-056 dyed glass filter was adopted in the instrument (Turner Designs, 1990) which cut out all light above 546 nm for the excitation of Rhodamine WT. Although the maximum excitation of Rhodamine WT occurs at 550 nm, Smart and Laidlaw (1977) stated that excitation would occur as the excitation wavelength of the material ranges from 480 nm to 610 nm.

An excited fluorescent material immediately relaxes and a longer wavelength of light is released as a product of the relaxation process. The amount of re-emitted light is directly proportional to the concentration of the fluorescent material within the measuring volume, normally when the concentrations are low. The concentration threshold, which is the level before quenching

(fluorescence intensity does not increase with concentration but decreases with further concentration increases), depends on the type of fluorescent materials used, temperature and pH level of the solution. The threshold level can be easily determined via calibration. The emission spectra of Rhodamine WT are approximately from 540 nm to 640 nm, with a maxima at 580 nm (Smart and Laidlaw, 1977). To measure the intensity of the re-emitted light, the instruments were equipped with a 10-052 dyed glass filter (Turner Designs, 1990) which allows wavelengths greater than 570 nm to pass and removes the original light source. The intensity of light passing through the emission filter was measured as a voltage using a photomultiplier. To ensure that there was no degeneration in the fluorometer signal due to fluctuations in the light source or response of the photomultiplier, the instrument automatically calibrated itself 13 times a second. In the calibration, a zero reading was recorded, with no light source, to provide a reference fluorescence value; the intensity of the light source was noted to account for any fluctuations in power supply which would affect the fluorescence emitted; the instruments used this information to calculate a resultant fluorescence, from which a representative voltage was generated as an analogue signal. The analogue signal, similar to the water level follower data, was logged at 50 Hz using a data logger and stored in a personal computer hard disk. The concentration of the fluorescent material was determined from the analogue signal via calibration.
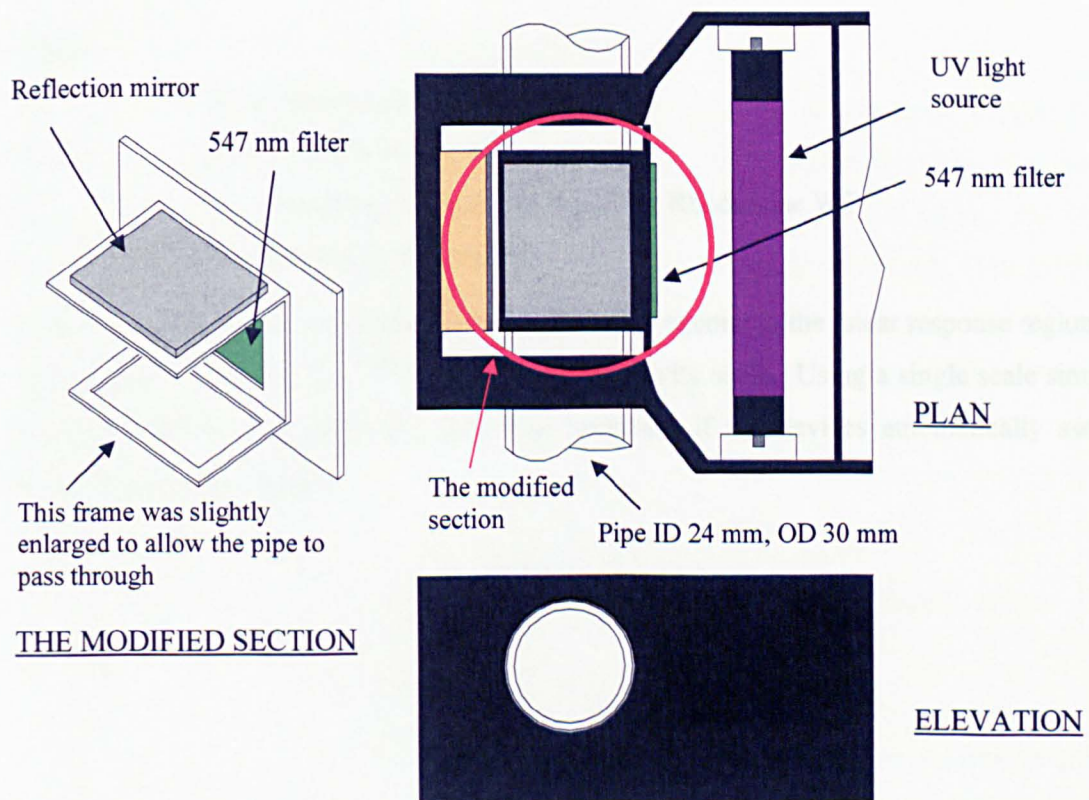
Figure 3.7 – Diagram of the fluorometer measuring compartment

Calibration of the fluorometers was undertaken in-situ in a smaller isolated closed system bypassing the header tank and the sump. The experimental section was disconnected from the rig and re-connected to a separate water tank with 40 litres of water. The water was recirculated through the system using a Water Puppy® pump (Jabsco) throughout the process. A known quantity of Rhodamine WT was introduced to the bulk of water and measurement was recorded when the solution became fully mixed. It took approximately 20 minutes to reach fully mixed condition by continuous water recirculation. For each calibration concentration, the output signals of the fluorometers were logged for 5 minutes and the average value was used.

Temperature has a substantial influence on the Rhodamine WT properties. High temperature reduces the fluorescent properties of the solution due to an increase of molecular motion with increasing temperature resulting in collisional quenching (Guilbault, 1990). Collisional quenching is the process that an excited molecule undergoes non-radiative relaxation when contacts with other molecular in the solution (Lakowicz, 2006). During the calibration process, the temperature of the solution increased due to the heat generation from the pump. The recorded readings for each calibration concentration, therefore, required adjustment for temperature using the equation given by Smart and Laidlaw (1977) (Equation 3.3). An example of the calibration results is illustrated in Figure 3.8.

$$F_t = F_0 \exp(nt_c) \qquad\qquad 3.3$$

where:

F_t	is the fluorescence at t °C
F_0	is the fluorescence at 0 °C
n	is a constant and is equal to -0.027 for Rhodamine WT
t_c	is the solution temperature

In the tracer study, the fluorometers were regulated to operate in the linear response region up to dye concentrations of 2.5×10^{-7} l/l on a single sensitivity scale. Using a single scale simplifies the calibration and prevents any data loss occurring if the devices automatically switched between sensitivity scales.
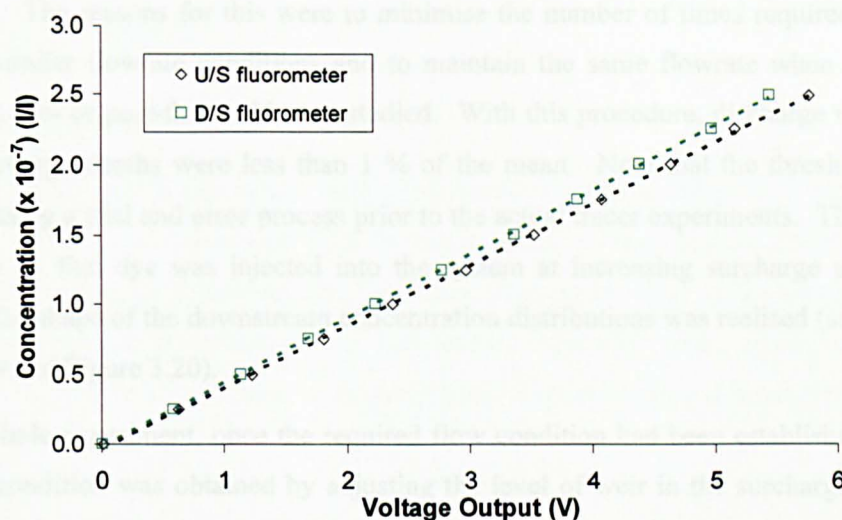
Figure 3.8 – Example of calibration for fluorometers (Temperature adjusted to 15 °C)

	Equation (through the origin)	R_t^2
Upstream fluorometer	Concentration = 0.4373 × Output − 0.0304	0.9998
Downstream fluorometer	Concentration = 0.4578 × Output − 0.0176	0.9998

Table 3.4 – Equation describing the calibration equation of the fluorometers

3.3.5 Test Procedure and Schedule

In stage one of the laboratory experiment, energy loss and longitudinal dispersion were measured in the scale manhole and the straight pipe. In the manhole study, five flowrates between 0.25 l/s and 0.50 l/s and ten surcharge depths within the range of 10 mm and 100 mm were considered, resulting in five hundred steady flow hydraulic conditions. For the straight pipe, six flowrates between 0.25 l/s and 0.50 l/s were studied (Table 3.5).

Straight Pipe Study	
Flowrates considered:	0.25, 0.3, 0.35, 0.4, 0.45 and 0.5 l/s
Manhole Study	
Flowrates considered:	0.25, 0.3, 0.35, 0.4 and 0.5 l/s
Surcharge depths considered:	10, 20, 30, 40, 50, 60, 70, 80, 90 and 100 mm

Table 3.5 – Summary of laboratory tests

As the discharge control valve showed poor repeatability of flowrate, in the manhole experiment, experiments for a single discharge were completed in two days; one day for pre-threshold data collection (10 mm – 50 mm surcharge) and the other day for post threshold (60 mm – 100 mm

surcharge). The reasons for this were to minimise the number of times required to adjust the valve for similar flowrate conditions and to maintain the same flowrate when one hydraulic regime, i.e. pre- or post-threshold, was studied. With this procedure, discharge variations over the 10 surcharge depths were less than 1 % of the mean. Note that the threshold depth was measured using a trial and error process prior to the actual tracer experiments. The process was carried out by that dye was injected into the system at increasing surcharge until a distinct change in the shape of the downstream concentration distributions was realised (see examples in Figure 3.19 and Figure 3.20).

In the manhole experiment, once the required flow condition had been established, the desired surcharge condition was obtained by adjusting the level of weir in the surcharge control tank. This adjustment was a trial and error process and time was given to allow the system to settle to steady flow conditions.

In each individual test run, approximately 25 ml of the dilute solution, with a concentration of between 8×10^{-6} l/l and 1.5×10^{-5} l/l depending on the operating flowrate, was introduced in the form of an instantaneous injection into the supply pipe 4 m upstream of the upstream sampling station. It is believed that this distance, more than 100 pipe diameters (IDs), would have ensured that the solute concentration was cross-sectionally well mixed at the upstream measurement position. The start of data logging, for the fluorometers and the water level follower, began at 1 minute prior to the dye injection. This ensured the capture of 30 s background concentration for subsequent data analysis. The time to peak was generally less than 5 s. In all cases, the solute concentration at the downstream measurement position had returned to background levels well within the 5 minute logging period. For the pressure measurement, the manometer readings were recorded three times during each run. For each test case, five repeat runs were performed.

3.4 Data Analysis

3.4.1 Energy Loss Coefficient

Pressure readings during the steady state experiments fluctuated within ± 1 mm of the mean value. The readings were averaged prior to data analysis. In the manhole study, head loss due to the manhole, ΔH, is defined as the difference in pressure head at the manhole centreline between the extrapolated upstream and downstream hydraulic lines, obtained from 3 point measurements (Figure 3.9). Values of the coefficient were calculated using Equation 3.4.

$$\Delta H = K_L \frac{u^2}{2g}$$
3.4

where:

g refers to gravitational acceleration

K_L is the head loss coefficient

u is the mean pipe velocity
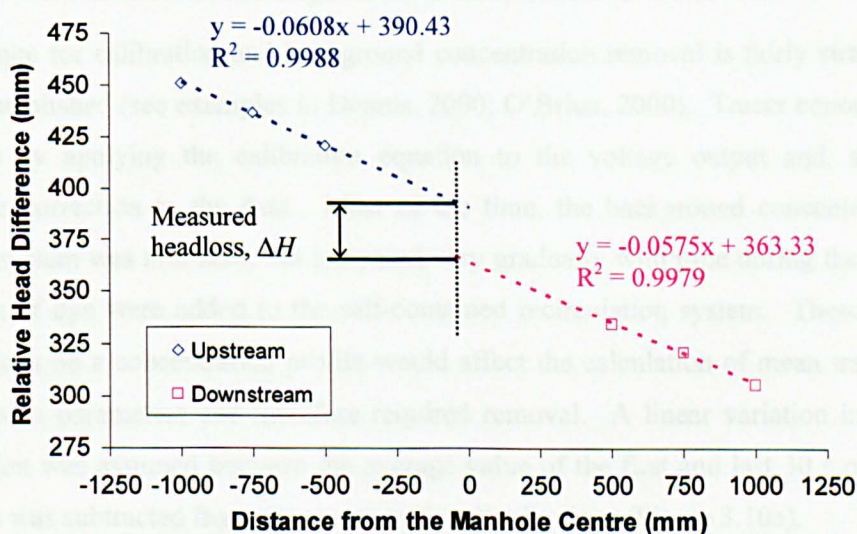
Figure 3.9 – Example of manhole headloss estimation

In the manhole datasets, a minor error in pressure measurement was observed; the measured downstream slope does not equal the measured upstream slope but is consistently shallower (on average 5 % lower in value), see example in Figure 3.9. One possible explanation for this phenomenon is that a fully developed flow profile had not been completely established at 16 pipe diameters (IDs) downstream of the manhole. If this was the case, the hydraulic gradient between the three measurement points at the downstream would be marginally different from that at the upstream, where a fully developed flow profile existed. Archer et al. (1978) measured the minimum distance required for the re-establishment of fully developed flow after

a manhole exit, concluding that it was approximately 70 pipe diameters (IDs) downstream of the manhole. However, due to space constraints in the laboratory and limited time available, it was not possible to re-configure the laboratory system and re-do the measurement. It is believed that the analysed results would not be far from the results measured in the ideal situation, as the difference in the slope throughout the datasets averaged 5 %.

3.4.2 Temporal Concentration Distributions Post-processing

For each individual injection of solute tracer, temporal concentration distributions were recorded from both upstream and downstream fluorometers. The data captured from the fluorometers comprised digital signals, which required post-processing to determine the concentration distributions corresponding to the solute. The post-processing procedure comprised calibration, background concentration removal and identification of the start and end points of temporal concentration distributions. All post-processing analysis of the tracer profiles was programmed and undertaken in MATLAB® (www.mathworks.com).

3.4.2.1 Calibration and Background Concentration Removal

The technique for calibration and background concentration removal is fairly straight-forward and well-established (see examples in Dennis, 2000; O'Brien, 2000). Tracer concentration was determined by applying the calibration equation to the voltage output and, subsequently, temperature correction to the data. Most of the time, the background concentration of dye within the system was non-zero, but increased very gradually with time during the experiments as volumes of dye were added to the self-contained recirculation system. These background concentrations on a concentration profile would affect the calculation of mean travel time and any dispersion parameters and therefore required removal. A linear variation in background concentration was assumed between the average value of the first and last 30 s of a particular trace. This was subtracted from the concentration distributions (Figure 3.10a).

3.4.2.2 Elimination of Noisy Background Data

Electrical interference within the Turner Design fluorometers unavoidably generated measurement noise. This noise is entirely random and the noisy data on the background would affect subsequent data analysis, such as travel time estimation by moment analysis, if not eliminated from the distribution. A way of removing it is to apply cut-offs to the distribution. This identifies the start and end of the trace. Dennis (2000) proposed a cut-off scheme, which was applied to the 800 mm ID manhole (prototype) tracer profiles. The scheme defines the cut-off as the 10th consecutive data point away from the peak with a concentration value less than 1 % of the peak concentration. This cut-off technique was tested on the straight pipe data.

Results showed that the technique successfully eliminated the noisy background, whilst keeping the entire solute trace (mass balances of nearly 100%). For comparative purposes, the same scheme was applied to the straight pipe and manhole data collected in this study.

The cut-off technique proposed by Dennis (2000) performed very well in terms of mass balance in all straight pipe cases. However, when this was applied to the manhole profiles, the resultant mass balance dropped to an average value of 94.8 %, with greater loss being observed at high surcharge depths. A mass balancing procedure is commonly used when the mass on the profiles is not conserved. It is achieved by multiplying the downstream data points with a mass balance factor, B, which is the ratio of the total mass measured upstream over the mass measured downstream:

$$B = \frac{\int_{t=-\infty}^{\infty} C_u \, dt}{\int_{t=-\infty}^{\infty} C_d \, dt} \qquad\qquad 3.5$$

where:

C_u, C_d are the concentrations on the upstream and downstream profiles

It was thought that with reference to the mass recovery ratio for the straight pipe (100 %) and manhole cases (94.8 %), the loss in mass in the manhole case was mainly attributed to the measurement limitation of the fluorometer at low concentrations and possibly the fact that the trace might not be cross-sectionally well mixed at the downstream monitor. The Turner Design fluorometers inevitably produced noise during measurements. When the concentrations were very low, for example the tail section of the manhole profiles (Figure 3.20), the degree of noise might be of the same order of magnitude as the low concentrations. Measurements of the noise level in the instruments suggest that the noise fluctuated about a mean reading of ± 0.05 V (see Section 4.2.3). This implies that at concentrations with a voltage reading of less than 0.05 V relative to the background readings, it is highly possible that the true readings were hidden by the instrument noise and hence were mis-read as background. This could be the reason to explain greater loss being observed at high surcharge depths. The downstream concentration profile for high surcharges is characterised by a long recession tail with very low concentrations. The length of the tail reduces with surcharge depth (see examples in Figure 3.19 and Figure 3.20). Observations from the LIF flow field visualisation data in Chapter 5 (see examples in Figure 5.33 and Figure 5.36) suggest that when the trace leaves the manhole, there are spatial variations of the dye concentration across the outlet. The dye might not be cross-sectionally well mixed within a length of 10 times the pipe diameter (ID). However, this hypothesis cannot be proved due to the lack of LIF flow field data at the downstream fluorometer position.

The mass balancing procedure achieves conservation of mass by scaling the entire downstream profile according to the mass balance factor, assuming that the loss in mass is uniform along the whole distribution. However, this assumption is invalid in the manhole case, as it is presumed that the loss was from the tail which was not measured accurately due to limitations in instrumentation and, possibly, the fact that the dye was not cross-sectionally well-mixed at the downstream fluorometer. Applying this simple mass balancing procedure to the manhole profile would mean that, although conservation of mass between the upstream and downstream distributions was obtained, the procedure would have erroneously increased some of the high concentration values (not an effect of the measurement limitation). As a result, none of the laboratory data was mass balanced.

(a) – Background concentration removal

(b) – Application of the cut-off scheme proposed by Dennis (2000)

(c) – Profile after the post-processing process
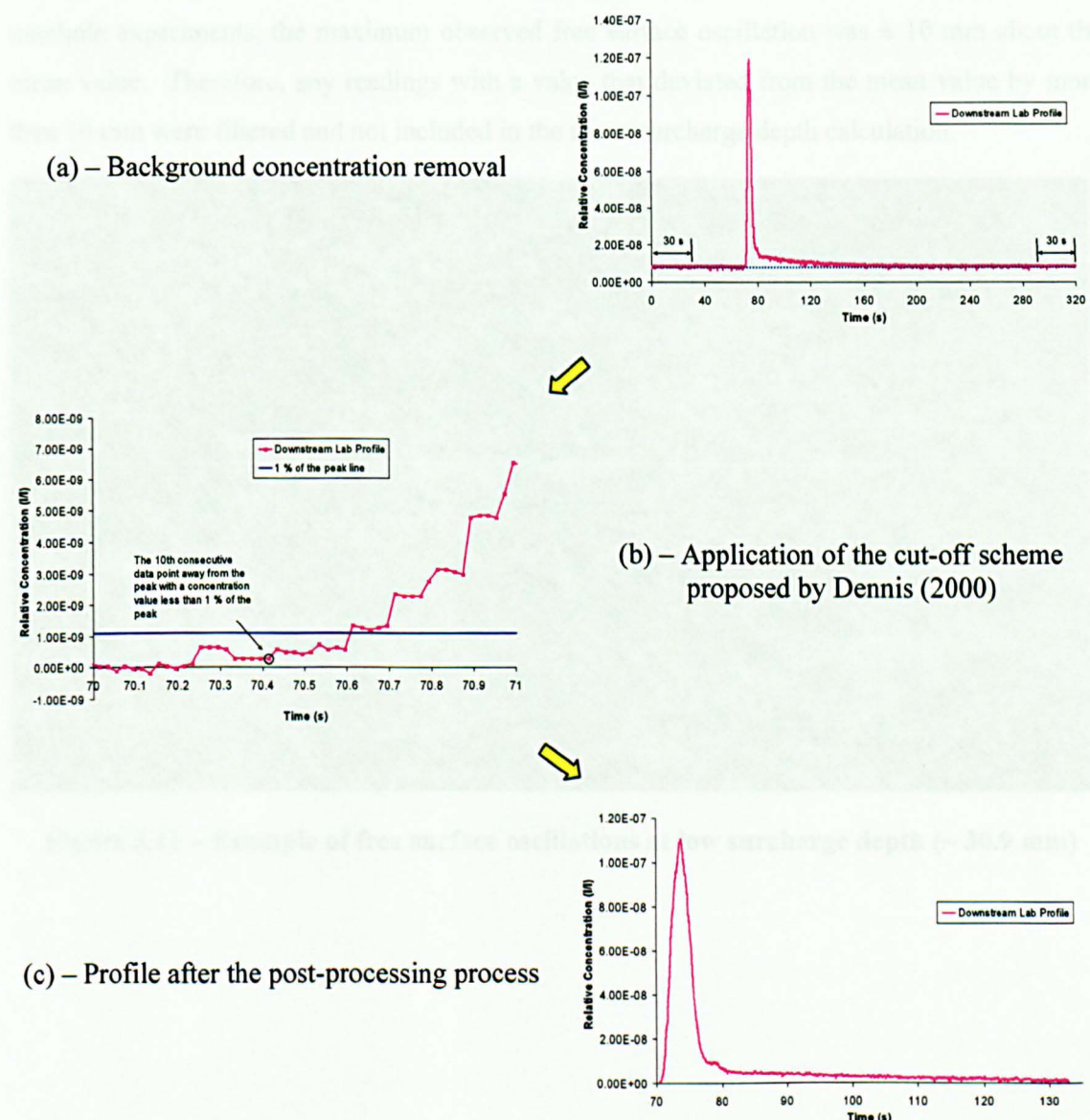
Figure 3.10 – Diagram of temporal concentration distribution post-processing processes

3.4.3 Mean Surcharge Depth

Under steady hydraulic conditions, variations in surcharge level during the experiment were observed. Measurements from the water level follower showed a mean standard deviation of 2 mm over the range of surcharge depths studied. Greater fluctuations were observed at low surcharge depths (Figure 3.11).

In certain circumstances, where the free surface in the manhole fluctuated about a mean depth at high frequency, the water level follower failed to track the surface and gave erroneous readings, for example a signal reading corresponding to a negative surcharge level (see Figure 3.12). These readings were eliminated via an iterative filtering process in the calculation of time average surcharge level. The operation of the process is explained in Figure 3.13. In the scale manhole experiments, the maximum observed free surface oscillation was ± 10 mm about the mean value. Therefore, any readings with a value that deviated from the mean value by more than 10 mm were filtered and not included in the mean surcharge depth calculation.
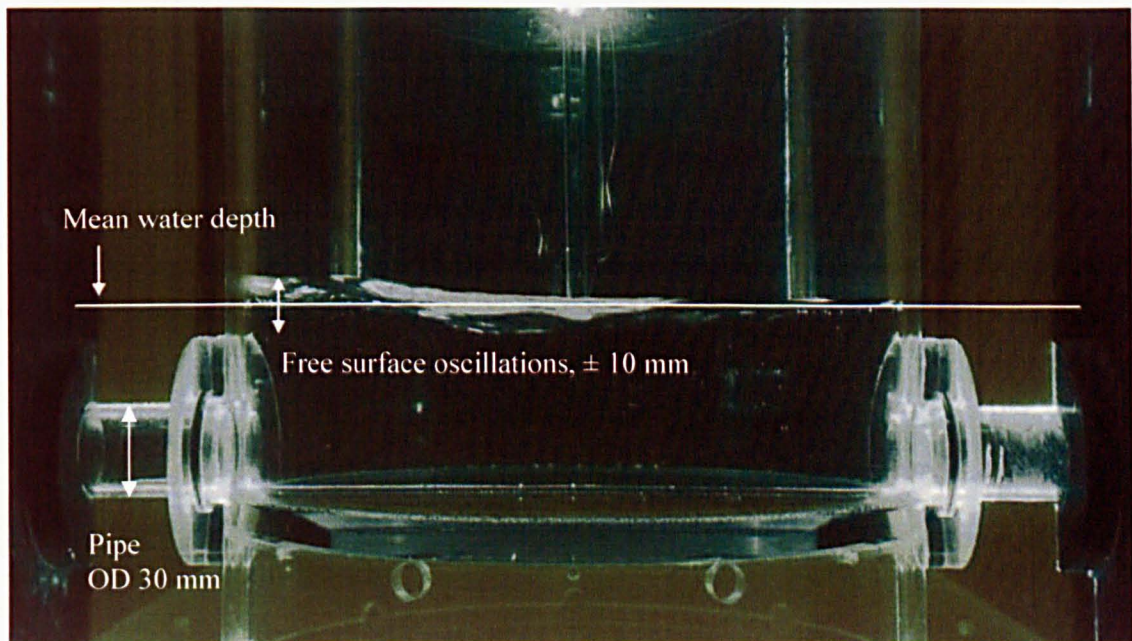
Figure 3.11 – Example of free surface oscillations at low surcharge depth (~ 30.9 mm)
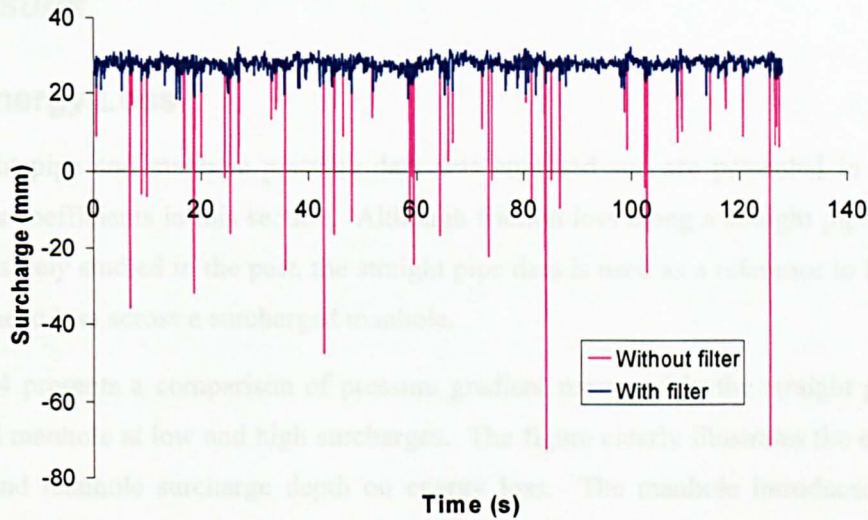
Figure 3.12 – Example of erroneous readings measured by the water level follower (Measurement of the free surface level illustrated in Figure 3.11)

| Stage 1 | Estimate a mean surcharge depth from the entire data series |

⇩

| Stage 2 | Examine the dataset to see whether there are any readings that deviate from the mean surcharge depth by more than the pre-defined tolerance level, i.e. ± 10 mm |

Yes ⇩   ⇩ No

| Stage 3 | Filter these readings from the dataset and recalculate the mean surcharge depth; back to Stage 2 | The mean surcharge depth for this particular data series equals the last calculated mean surcharge depth |

Figure 3.13 – Representation of the iterative filtering process for surcharge depth calculation

3.5 Results

3.5.1 Energy Loss

The straight pipe and manhole pressure data was analysed and are presented in the form of energy loss coefficients in this section. Although friction loss along a straight pipe might have been extensively studied in the past, the straight pipe data is used as a reference to highlight the effects of head loss across a surcharged manhole.

Figure 3.14 presents a comparison of pressure gradient measured in the straight pipe and the surcharged manhole at low and high surcharges. The figure clearly illustrates the effects of the manhole and manhole surcharge depth on energy loss. The manhole introduces extraneous secondary head loss and the loss appears to be a function of surcharge depth, with greater energy loss being observed at low surcharge.
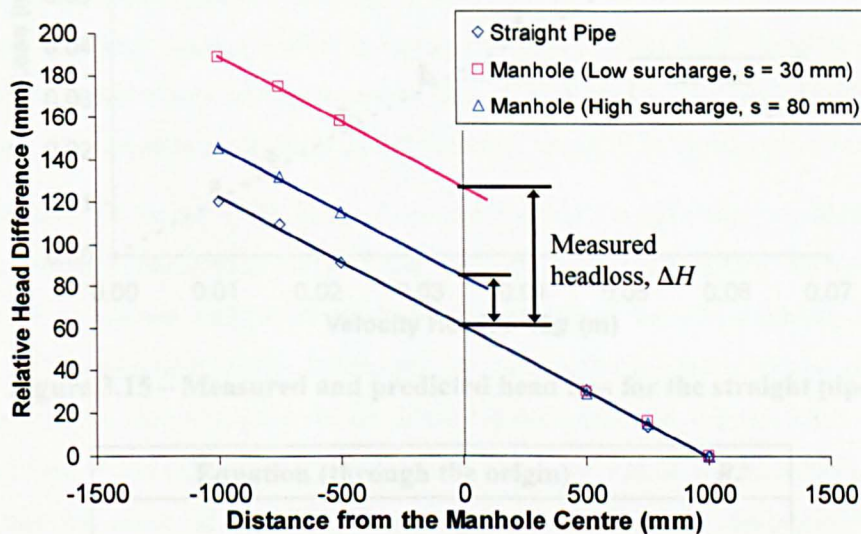
Figure 3.14 – Comparison of head loss along the six pressure measurement points between the straight pipe and scale manhole (*s* - surcharge depth)

3.5.1.1 Energy Loss Coefficient – The Straight Pipe

The energy loss coefficient for the straight pipe was estimated by plotting head loss against velocity head, as shown in Figure 3.15. A trendline through zero is fitted through the data points. The slope of the trendline (1.0278 m^{-1}) indicates the value of the coefficient for 1 m of this particular straight pipe (Table 3.6).

For turbulent flows, the head loss coefficient in a smooth pipe, K_{sp}, can be predicted using the Blasius equation associated with the Darcy-Weisbach equation (Chadwick and Morfett, 1998):

$$K_{sp} = \frac{4 \times 0.079}{D_p \times Re^{0.25}}$$ 3.6

where:

D_p is the pipe internal diameter

The Blasius smooth pipe data is also plotted in Figure 3.15. The error bars indicate ± 5 % deviations from the prediction. Comparison of the two datasets highlights that the laboratory measurement fits well to the smooth pipe prediction, with less than 5 % difference. A high level of accuracy in the measurement would be expected as this is a relatively simple structure.
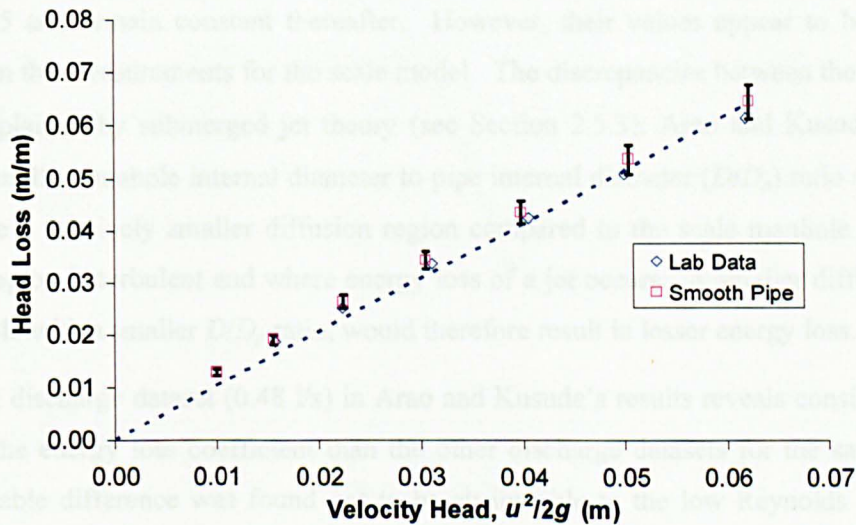
Figure 3.15 – Measured and predicted head loss for the straight pipe

Equation (through the origin)	R_t^2
$\Delta H = 1.0278 \times \dfrac{u^2}{2g}$	0.9847

Table 3.6 – Equation describing the linear best fit line for the head loss in the straight pipe

3.5.1.2 Energy Loss Coefficient – The Scale Manhole

The Energy loss coefficient of the manhole is plotted against surcharge ratio at a range of discharges in Figure 3.16. The surcharge ratio, S, is defined as the ratio of surcharge depth (measured with respect to the pipe soffit) to pipe internal diameter. A sharp transition in the energy loss coefficient between low and high surcharges is evident at surcharge ratios between 2.0 and 2.5. At surcharge ratios below the depth where the transition appears (the threshold depth), but above $S = 0.7$, energy loss coefficients seem to increase slightly with surcharge ratio. After the transition, the coefficient values are reduced by half compared with the values in the pre-threshold region, yielding a coefficient value of around 0.45.

At the lowest surcharge ratio considered in Figure 3.16, there are three data points that fall below the linear trend, with values less than 0.9. This phenomenon is similar to that observed by Arao and Kusuda (1999), shown in Figure 3.17. In the range of 0.0 to 0.5 surcharge ratio, their data suggests that energy loss coefficients increased rapidly with surcharge; beyond this region, the rate of increase began to flatten off until the hydraulic transition point, marked by a sudden drop in the energy loss coefficient value, was reached.

The relationship between energy loss coefficient and surcharge ratio observed in the post-threshold region (Figure 3.16) matches well to the experimental findings of Arao and Kusuda (1999). Immediately after the hydraulic transition, the coefficient values drop significantly to around 0.45 and remain constant thereafter. However, their values appear to be marginally smaller than the measurements for the scale model. The discrepancies between the two datasets may be explained by submerged jet theory (see Section 2.5.3): Arao and Kusuda's manhole obtains a smaller manhole internal diameter to pipe internal diameter (D/D_p) ratio and therefore would have a relatively smaller diffusion region compared to the scale manhole model. The diffusion region is turbulent and where energy loss of a jet occurs. A smaller diffusion region, or a manhole with a smaller D/D_p ratio, would therefore result in lesser energy loss.

The lowest discharge dataset (0.48 l/s) in Arao and Kusuda's results reveals consistently lower values of the energy loss coefficient than the other discharge datasets for the same manhole. The noticeable difference was found not to be attributable to the low Reynolds number (Re) effects on the development of the submerged jet within the manhole, as the corresponding Reynolds number at the inlet pipe for the lowest discharge (0.48 l/s) is 12,200. This value indicates the flow at the pipe should be in the fully turbulent regime and Albertson et al. (1950) suggested that the onset of the full development of turbulence in the region of diffusion occurred at a Re value corresponding to the jet outlet of 1,500. In addition, the lowest discharge considered in the scale model (218 mm ID manhole) gives a Re value of 11,634 and the corresponding dataset shows similar coefficient values to the higher discharge (or Re) measurements. Arao and Kusuda do not offer an explanation for the discrepancy between their measurements.

Figure 3.17 suggests that a secondary peak in energy loss occurred at surcharge ratios of around 3.3 (i.e. three times the surcharge ratio associated with the primary step in energy loss coefficient). As the present laboratory data set does not extend beyond two times the threshold surcharge ratio, it is not possible to comment on the existence or not of a comparable secondary peak. Energy loss coefficient does not appear to be strongly dependent upon discharge, with the exception of the lowest discharge considered in Arao and Kusuda (1999).

The threshold depth for the hydraulic transition differs between the present data set and that presented by Arao and Kusada (1999) (surcharge ratio of 2.5 compared with 1.0). This reflects the fact that the two studies have considered manholes with different D/D_p ratios. Guymer *et al.* (2005) suggested that the threshold depth varies as a linear function of the D/D_p ratio, and that the value of the threshold depth can be approximately predicted by reference to submerged jet theory. Hereafter, surcharge depths below the threshold are termed pre-threshold and the converse are named post-threshold.

This part of the work (Section 3.5.1.2) has been published in Lau et al. (2008).
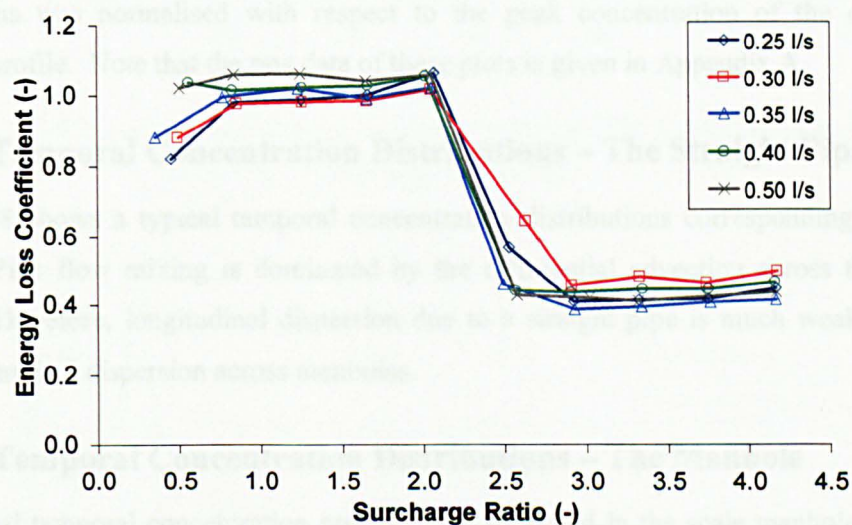
Figure 3.16 – Variations of energy loss coefficient with surcharge ratio for the 218 mm ID manhole
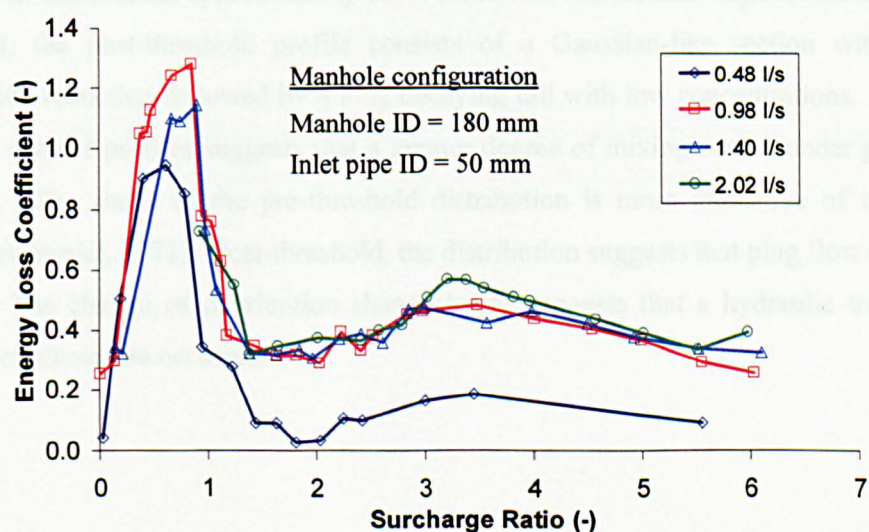
Figure 3.17 – Variations of energy loss coefficient with surcharge ratio (after Arao and Kusuda, 1999)

3.5.2 Temporal Concentration Distributions

After post-processing, temporal concentration distributions were saved in output files with '.csv' format. Each of these files contained data for time and concentration values. These were subsequently plotted as concentration against time showing the mixing characteristics of the flow.

Three typical temporal concentration distributions were observed in the laboratory studies, one from the straight pipe and the rest from the manhole. Examples of the profiles are presented in Figure 3.18 - Figure 3.20. For comparative purposes, the y-axis of the concentration distributions was normalised with respect to the peak concentration of the corresponding upstream profile. Note that the raw data of these plots is given in Appendix A.

3.5.2.1 Temporal Concentration Distributions – The Straight Pipe

Figure 3.18 shows a typical temporal concentration distributions corresponding to pipe flow mixing. Pipe flow mixing is dominated by the differential advection across the pipe cross section. Therefore, longitudinal dispersion due to a straight pipe is much weaker, compared with longitudinal dispersion across manholes.

3.5.2.2 Temporal Concentration Distributions – The Manhole

Two typical temporal concentration profiles were observed in the scale manhole. The profile shown in Figure 3.19 is typical of low surcharge conditions, pre-threshold, and the profile in Figure 3.20 appears under post-threshold conditions. The pre-threshold profile is characterised by large peak attenuation, approximately 50 % reduction, and an near-exponential decaying tail. In contrast, the post-threshold profile consists of a Gaussian-like section with low peak concentration reduction followed by a long decaying tail with low concentrations. Comparison of the two distinct profiles suggests that a greater degree of mixing occurs under pre-threshold conditions. The shape of the pre-threshold distribution is more indicative of instantaneous mixing (Levenspiel, 1972). Post-threshold, the distribution suggests that plug flow dominates in the flow. The change of distribution shape clearly suggests that a hydraulic transformation within the manhole has occurred.
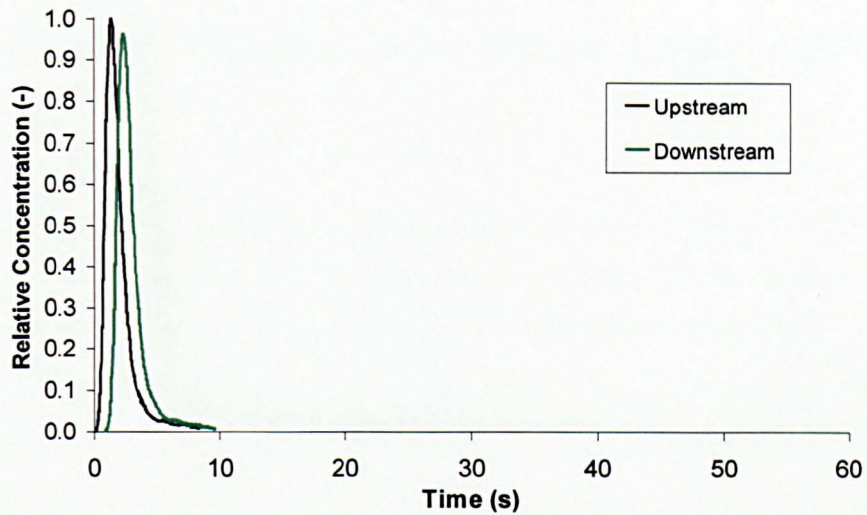
Figure 3.18 – Example of tracer temporal concentration distributions in the straight pipe study ($Q = 0.35$ l/s)
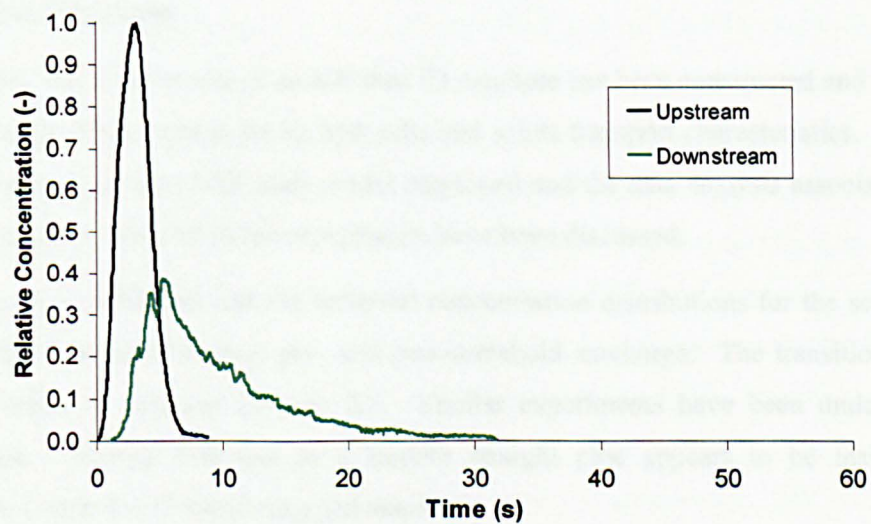
Figure 3.19 – Example of tracer temporal concentration distributions in the scale manhole study ($Q = 0.35$ l/s; $S = 1.25$; Pre-threshold)
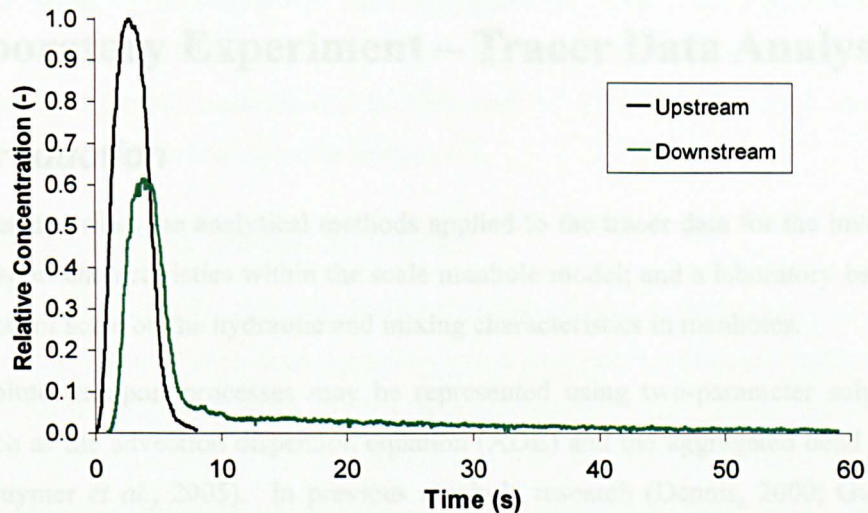
Figure 3.20 – Example of tracer temporal concentration distributions in the scale manhole study (Q = 0.35 l/s; S = 3.33; Post-threshold)

3.6 Conclusions

A 1:3.67 physical scale model of an 800 mm ID manhole has been constructed and experiments have been undertaken to examine its hydraulic and solute transport characteristics. The general laboratory arrangements of the scale model employed and the data analysis associated with the measurement data collected in the experiments have been discussed.

The energy loss coefficient and the temporal concentration distributions for the scale manhole show a sharp transition between pre- and post-threshold surcharge. The transition appears at surcharge ratios of between 2.0 and 2.5. Similar experiments have been undertaken on a straight pipe. Energy loss due to a smooth straight pipe appears to be insignificant in comparison to that due to the surcharged manhole.

The analysis of the temporal concentration distributions and the study of the effects of scale on the mixing process in surcharged manholes using a laboratory-based analysis are covered in the following chapter.

4 Laboratory Experiment – Tracer Data Analysis

4.1 Introduction

This chapter describes the analytical methods applied to the tracer data for the investigation of solute transport characteristics within the scale manhole model; and a laboratory-based analysis of the effects of scale on the hydraulic and mixing characteristics in manholes.

Primary solute transport processes may be represented using two-parameter solute transport models such as the advection dispersion equation (ADE) and the aggregated dead zone (ADZ) models (Guymer et al., 2005). In previous manhole research (Dennis, 2000; Guymer et al., 2005; Saiyudthong, 2004), the laboratory tracer measurements were analysed using the two models in order to quantify longitudinal dispersion of solutes due to the specific manhole configurations. Results in the form of parameter coefficients for the ADE and the ADZ models were derived. Following the previous research, the ADE and ADZ models have been employed for the analysis of the scale manhole tracer data.

Laboratory derived mixing parameters for manholes (Dennis, 2000; Guymer et al., 2005; Saiyudthong, 2004) may be used in urban drainage network models that predict the transport of dissolved substances. For example, the two-parameter ADE equation has been incorporated in MOUSE TRAP (DHI, 2000) to account for the transport and dispersion of dissolved substances in sewerage systems; Boxall et al. (2005) developed a modular sewer quality model which utilised the ADZ model to describe solute transport in sewer networks. However, at present the applicability of laboratory-scale derived parameters to full scale structures in the urban drainage system, i.e. scalability of these parameters, is not clearly understood. The ADE and ADZ analysis of the scale manhole data provides an opportunity to enhance our understanding of the scalability of the mixing parameters corresponding to manholes.

In addition to the ADE and ADZ analyses, cumulative temporal concentration profiles (CTCPs) have been used to study the effects of discharge and surcharge on the solute transport characteristics within the scale manhole. A CTCP can provide information regarding the fundamental mixing characteristics occurring in a flow system. It is also a direct graphical representation of percentile travel times, such as t_{10}, t_{50} and t_{90}. Percentile travel times are often used to assess the hydraulic performance of a flow system (Adamsson, 2004; Danckwerts, 1958; Persson, 2000). The tracer data of the prototype has also been plotted as CTCPs for the study of scale effects within manholes. Section 4.2 describes the details of the ADE and ADZ analyses. The ADE and ADZ results for the 24 mm internal diameter (ID) straight pipe and the scale

manhole are presented in Section 4.3; also highlighted in Section 4.3 is the discussion of the analysed results and the comparisons of the mixing parameters of the two manholes. Section 4.4 presents the temporal concentration profiles and the CTCPs of the scale model and the prototype. This chapter is concluded in Section 4.5.

4.2 ADE and ADZ Model Analysis

The ADE and ADZ analyses quantify mixing characteristics of a flow system by estimating a pair of parameters from the measured profiles using parameter estimation techniques. In the past, before the development of the optimisation procedure (Dennis, 2000), the technique that had been adopted to predict mixing parameters was standard moment analysis (e.g. Guymer *et al.*, 1995). However, parameters derived from moment analysis (Equation 2.11 - Equation 2.14), hereafter called 'standard parameters', were often a poor representation of the actual mixing characteristics. Predictions made using the standard parameters significantly deviated from recorded profiles, especially in manhole tracer profiles (Dennis, 2000). Boxall (2000) offered an explanation to the poor representation given by the standard parameters. He explained that the inaccurate prediction of the parameters is attributable to the noise on the tracer profiles, particularly on the tail, leading to inaccuracies in the calculation of the centroid and variance from the recorded fluorometric data in the moment analysis.

Dennis (2000) proposed an alternative parameter estimation technique, called the optimisation procedure, for parameter evaluation in the ADE and ADZ analyses. Adaptation of the optimisation technique in the analyses resulted in noticeable improvement in the quality of the model prediction. This procedure has been previously used in solute transport analysis (e.g. Dutton, 2004; Richter, 2003). The optimisation procedure was adopted for the analysis of the scale model data.

4.2.1 Parameter Optimisation Procedure

The parameter optimisation procedure, developed by Dennis (2000), determines a set of representative coefficients for a pair of temporal concentration profiles via refined searches of the coefficients that give the best fit prediction to the downstream measured profile. A measure of the goodness of fit, R_t^2, (Young *et al.*, 1980) between the predicted and measured distributions is used to identify the best pair of the coefficients:

$$R_t^2 = 1 - \left[\frac{\sum_{t=1}^{n} (C(x_d,t) - P(x_d,t))^2}{\sum_{t=1}^{n} C(x_d,t)^2} \right] \leq 1 \qquad \qquad 4.1$$

where:

$C(x_d, t)$ is the recorded downstream concentration profile

$P(x_d, t)$ is the predicted downstream concentration profile

t is time

The measure of fit, R_t^2, is defined as the ratio between the sum of the squares of the errors and the sum of the squares of the measured concentration. An exact fit to the recorded downstream profile therefore gives a R_t^2 value of unity; a low value is indicative of poor quality of fit of the prediction. Note that this parameter represents the goodness of fit of the entire predicted profile; however, it does not provide information of the fit at a particular location or time, for example the goodness of fit at the peak.

There is an alternative measure, or objective criterion, to determine the optimum model parameters. The coefficient of determination, R^2 in Equation 2.29 (Young, 1992), could be used. However, Beven (2000) stated that this parameter would give a greater weight in fitting the peak than fitting lower concentrations. This parameter was not adopted in the analysis undertaken by Guymer et al. (2005), instead R_t^2 was employed as the measure of the goodness of fit. Therefore, R_t^2 was not used in the analysis of the scale manhole data.

To facilitate the analysis of the laboratory data the ADE and ADZ models in conjunction with the parameter optimisation analysis, developed by Dennis (2000), were programmed into MATLAB® (www.mathworks.com). A matrix system (11 x 11) is employed for the iterative searching and calculation processes. The search begins with a given range of values assigned to the parameters. For each pair of the coefficients, a downstream prediction in response to the recorded upstream concentration profile is made using the ADE or ADZ equation and a R_t^2 value is calculated for the predicted downstream profile. On the completion of the matrix calculations, the pair of coefficients which gives the prediction with the best fit to the measured downstream data, i.e. with the highest R_t^2 value, is determined from the 121 calculated R_t^2 values. A new matrix is subsequently created by the program which 'zooms in' towards the best fit coefficients and the process is repeated until the predetermined final resolution of the matrix boundary values is attained. The optimisation procedure is shown diagrammatically in Figure 4.1.
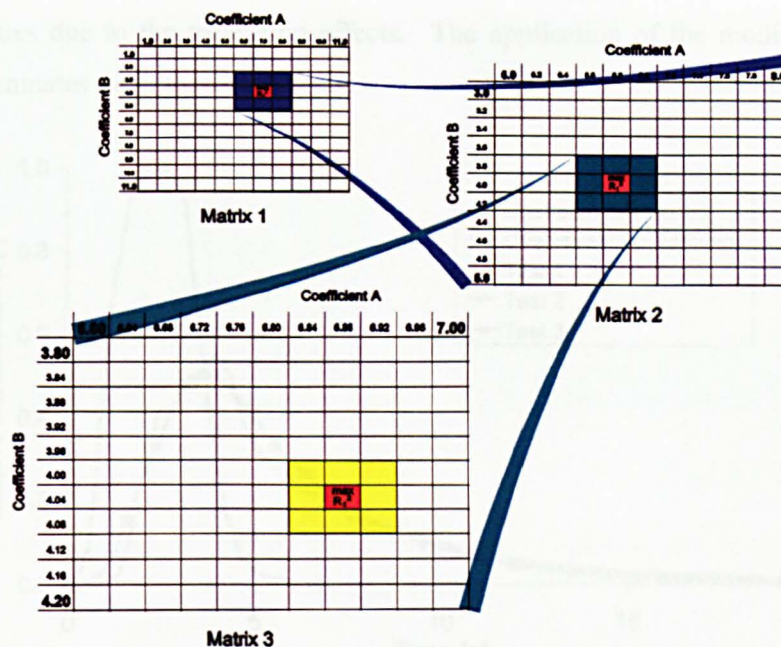
Figure 4.1 – Representation of the matrix optimisation procedure (after Dennis, 2000)

4.2.2 Modification of the Optimisation Procedure for ADZ model

The optimisation procedure for the ADZ model developed by Dennis (2000) was modified prior to the data analysis. The modified procedure adopted the direct variables, α and δ, of the ADZ equation as the ADZ optimisation parameters (Equation 2.22). The variable α describes the dispersion process of a solute travelling through a flow system; and δ describes the advection process. α and δ can be converted to travel time, $\bar{t}$, and reach time delay, τ, which were the optimisation parameters in Dennis (2000) procedure. Further information of the ADZ model can be found in Section 2.4.5.2.2.

There are two reasons for the modification of the earlier optimisation procedure. The original version of the ADZ optimisation procedure, proposed by Dennis (2000), employs travel time and reach time delay as the optimisation parameters. However, it was realised that the truncation effects associated with the use of integer values (determination of δ from $\tau/\Delta t$ for Equation 2.22) result in a non-unique solution. Steps or plateaux of values may lead to predictions with equally good fits. For example, in Figure 4.2, three sets of optimised results were derived for the upstream and downstream profiles using different initial ranges of the matrix (Matrix 1 in Figure 4.1) and the Dennis (2000) procedure. The three downstream predictions are in fact identical. However, careful examination of the results in Table 4.1 shows that the three sets of optimised travel time and reach time delay results vary between the tests. The reason for the same predictions is that the three sets of optimisation data result in the same

α and δ values due to the truncation effects. The application of the modified optimisation procedure eliminates the truncation effects.
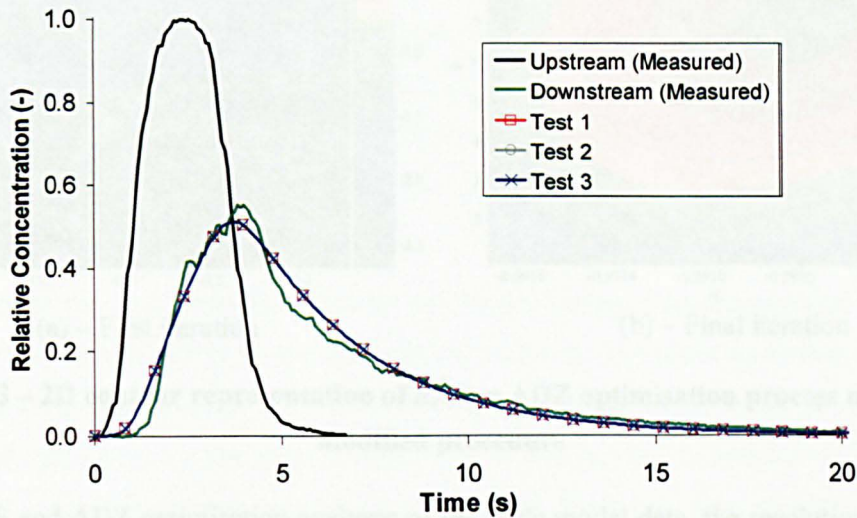
Figure 4.2 – Temporal concentration predictions using the optimised values in Table 4.1

Test	Travel Time (s)	Reach Time Delay (s)	Residence Time (s)	Sampling Time (s)	α (-)	δ (-)	R_t^2 (-)
1	3.1899	0.0236	3.1663	0.02	0.9937	1	0.9855
2	3.1808	0.0145	3.1663	0.02	0.9937	1	0.9855
3	3.1951	0.0288	3.1663	0.02	0.9937	1	0.9855

Table 4.1 – Three sets of optimised results derived at a resolution of 0.0001 s for travel time and reach time delay using Dennis (2000) ADZ optimisation procedure

The second reason for the modification is to increase the speed of the computation by removing the process that converts travel time and reach time delay to α and δ in each calculation of the prediction.

For the modified ADZ optimisation technique to be reliable, it was essential to verify that there was a unique pair of parameters that produced the best fit of the prediction to the measured data (Dennis, 2000). This was achieved by examining the R_t^2 values over the entire matrix and ensuring that there was only a single peak value. Figure 4.3 presents an example of 2D contour representation of R_t^2 in a ADZ optimisation process made by the modified procedure. The contour of R_t^2 was a 11 x 11 matrix, which was generated by 121 combinations of the values of α and δ considered. Figure 4.3a shows the R_t^2 distributions in the first iteration over the given range of the α and δ values; and Figure 4.3b presents the R_t^2 contour in the final iteration. It can be clearly seen that there is a single maxima of R_t^2 given by a α value of -0.9905 and a δ value of 7.

(a) – First iteration (b) – Final iteration
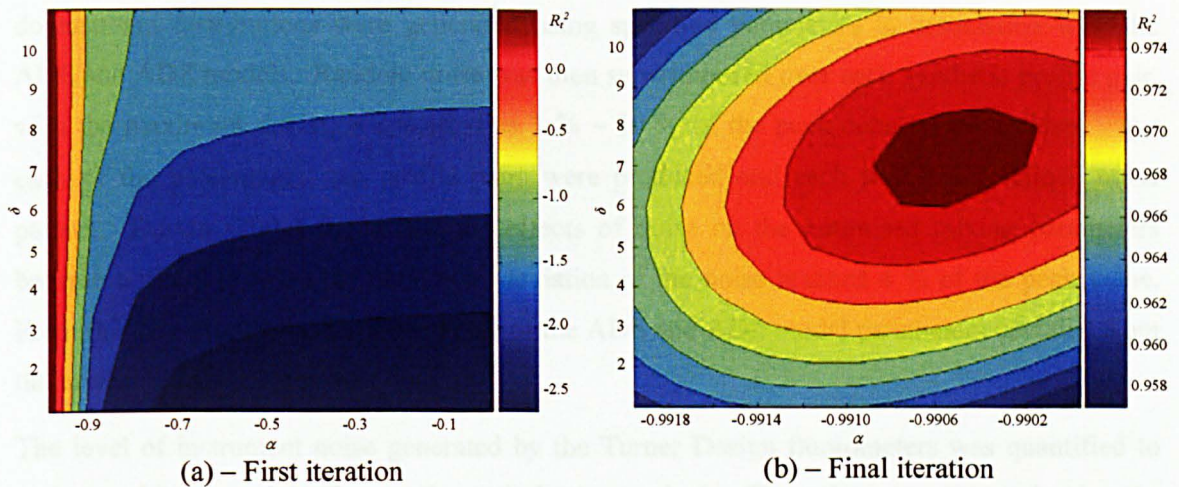
Figure 4.3 – 2D contour representation of R_t^2 in a ADZ optimisation process made by the modified procedure

In the ADE and ADZ optimisation analyses of the scale model data, the resolution adopted for each optimisation parameter is summarised in Table 4.2. The values used in the optimisation procedure revealed the same profile predictions as if the values were one order of magnitude smaller, i.e. higher resolution.

Optimisation Parameter	Resolution
ADE - Travel time, $\bar{t}$	0.0001 s
ADE - Dispersion coefficient, K	0.00001 m^2/s
ADZ – Alpha, α	0.0001 (-)
ADZ – Delta, δ	1 (discrete time step)

Table 4.2 – Resolution values predefined in the optimisation procedure

4.2.3 Effects of Noisy Data

Most tracer data collected in field or laboratory studies consist of actual measurements and, unavoidably, a superimposed disturbance due to random noise. For data with a low signal to noise ratio, the longitudinal dispersion analysis may be less straight-forward as the recorded data may not reveal the true observation and an additional signal filtering may be needed for isolation of the original signal. The optimisation procedure does not distinguish between the signal and noise but uses the resultant profile for the curve fitting exercise. Therefore, the resultant analysis may be influenced by the magnitude and location of the noise within the distribution (Dutton, 2004).

Dutton (2004) conducted a study to examine the effects of noisy data on the ADE and ADZ optimisation analyses based on a Gaussian upstream distribution. In his study, synthetic

downstream distributions were generated using specified parameters in association with the ADE and ADZ models. Random noise was then superimposed over each synthetic profile pair, with the maximum deviation specified as 1 % – 10 % of the peak concentration value. For each of the percentages, ten profile pairs were produced and each pair had a unique noise pattern. Dutton (2004) found that the effects of noise on the optimised mixing parameters became noticeable when the maximum deviation of the noise reached 4 % of the peak value. From this point onwards, the mean value of the ADE and ADZ model parameters deviated from the correct values initially specified.

The level of instrument noise generated by the Turner Design fluorometers was quantified to understand its potential effect on the optimisation analysis. The noise was measured using the background concentration measurements as the variations in the signal would purely correspond to the noise generated by the fluorometer. The investigation examined a number of 30 s background concentration measurements and the noise level was determined from the time-average voltage readings (Figure 4.4). It was noticed that, of the measurements examined, the maximum deviation from the mean values was only ± 0.05 V, which is generally approximately 3 % of the peak value of the measured profiles. Therefore, it is concluded that the effects of noise generated by the fluorometers on the optimised mixing parameters should be insignificant and a signal filter process was not required for the measured manhole data.

There are several approaches that can be adopted to filter or eliminate the random noise from recorded profiles. However, the discussion of these approaches is not included in this thesis, purely because none of the approaches was considered in the data analysis. The discussion can be found in Dutton (2004) and Richter (2003).
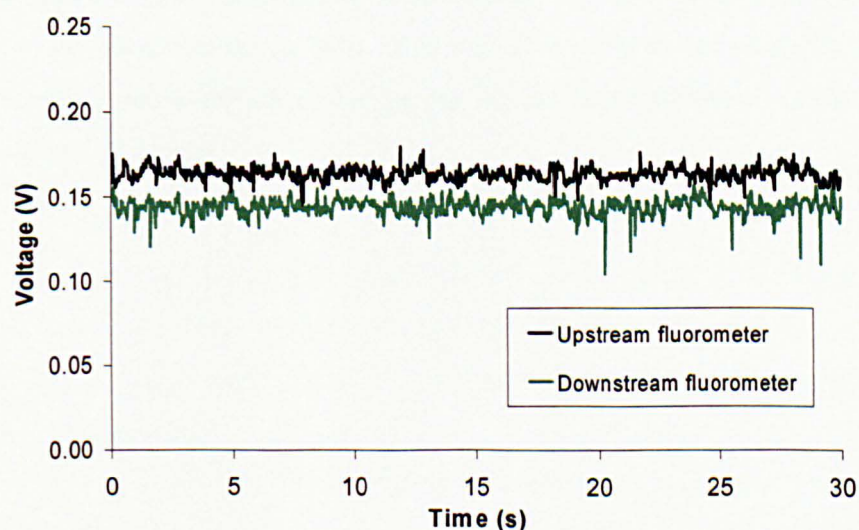
Figure 4.4 – Example of background concentration measurements

4.2.4 Sampling Rate

As reported in Section 3.3.4, the fluorometric data was logged at 50 Hz during the experiments. However, the actual response rate of the fluorometers to the concentration readings was slower than the data logged. 13 Hz is the actual rate for the fluorometers. The recorded data was therefore down-sampled at a rate of 4, giving a sampling rate of 12.5 Hz close to the actual response frequency of the instruments.

4.2.5 Conclusion

The ADZ optimisation procedure has been modified for the data analysis of the straight pipe and scale manhole data to improve precision and computational efficiency. The modified procedure has been tested to show a unique solution for a pair of tracer profiles. The ADE optimisation analysis was demonstrated by Dennis (2000) that it could generate a unique answer.

The effects of noise on the recorded data have been examined and the study shows that these should not impose a significant impact on the derived parameters. The recorded tracer profiles were down-sampled to a rate of 4 to eliminate redundant data and keep the maximum number of real data. A resolution that is insensitive to further refinement of the resolution was set in the optimisation procedure to obtain a unique and precise solution. The model parameters derived for the straight pipe and scale manhole data using the optimisation procedure should be the best solutions, in terms of R_t^2 (Young *et al.*, 1980), that the first order ADE and ADZ models can offer.

The following section presents the ADE and ADZ model results for the straight pipe and scale manhole.

4.3 ADE and ADZ Model Results

The longitudinal dispersion analysis programmed in MATLAB® (www.mathworks.com) generated an output file for each completed analysis. The output file comprised the data filenames, measuring station distance, mass balance factor and the resolution set for the optimisation analysis; all the standard and optimised coefficients were given, along with the R_t^2 value for each case; in addition, the measured profiles and the downstream predictions made using the standard and optimised coefficients were included.

The results presented in this section only consider the optimised model parameters. The reason for this is that the standard parameter values, especially in the manhole cases, gave a poor representation of the measured data. Figure 4.5 and Figure 4.6 provide a comparison between the standard and optimised ADE and ADZ predictions in response to the recorded upstream profile for a low and high surcharge cases. In these figures, the R_t^2 value, which is a measure of goodness of fit to the laboratory measurements (Young et al., 1980), is provided for each prediction. In all of the standard predictions, with the exception of the ADZ standard prediction in the low surcharge case, the dispersion is considerably over-estimated, predicting a peak concentration well below the measured value and a later peak arrival time. In the exceptional case, the ADZ standard prediction produces similar peak concentration value to the recorded, but with some delay of the peak arrival. Note that the raw data of the profiles in Figure 4.5 and Figure 4.6 is provided in Appendix A.

Further discussion of the usefulness of these two models in describing the manhole's mixing characteristics can be found in Section 4.3.4.

This section begins with the presentation of the straight pipe results and followed by the scale manhole data. At the end of this section, an attempted is made to study the effects of scale on the solute transport characteristics by comparing the optimised parameter results between the scale manhole and prototype.
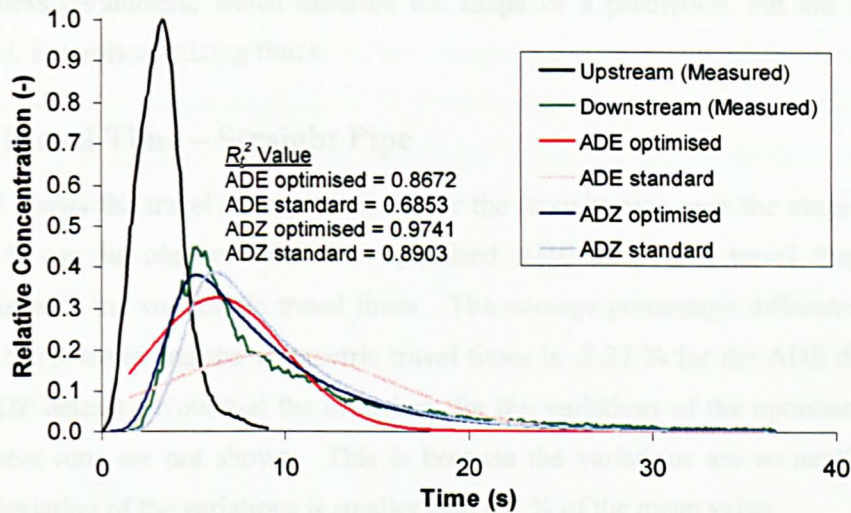
Figure 4.5 – Measured downstream temporal concentration profile (Q = 0.25 l/s; S = 0.417; Pre-threshold) with ADE and ADZ predictions for the scale manhole
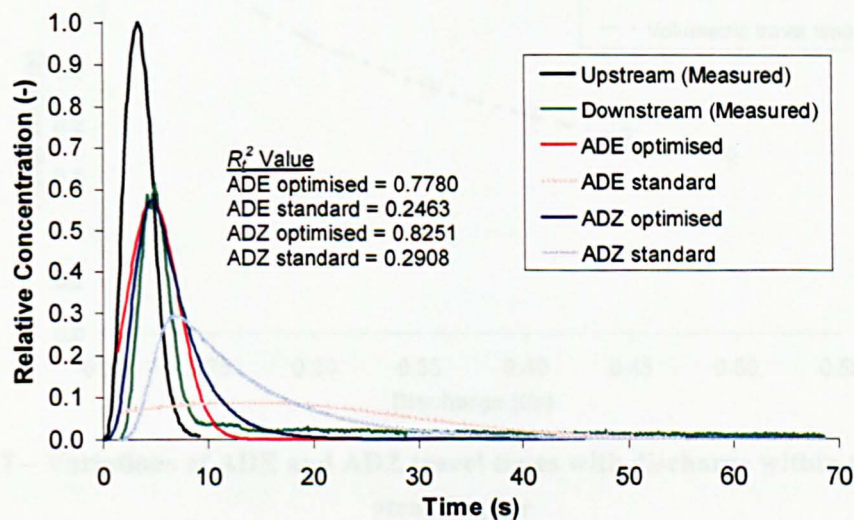
Figure 4.6 – Measured downstream temporal concentration profile (Q = 0.25 l/s; S = 4.167; Post-threshold) with ADE and ADZ predictions for the scale manhole

4.3.1 Straight Pipe

The ADE and ADZ optimised mixing parameters for the 24 mm ID straight pipe are plotted against discharge in Figure 4.7 - Figure 4.10. The error bars in these figures indicate one standard deviation of the variations of the value within repeat runs. For comparative purposes, the volumetric travel times, t_n, i.e. volume over discharge, and the theoretical dispersion coefficients, K_{Taylor}, derived by Taylor (1954) (Equation 2.15 – Equation 2.17), are also presented. The ADZ parameters presented here are travel time and reach time delay, converted from the direct variables, α and δ, of the ADZ equation. The reason for this is that α and δ are

dimensionless parameters, which describe the shape of a prediction, but are not physically meaningful, in terms of mixing times.

4.3.1.1 Travel Time – Straight Pipe

Figure 4.7 shows the travel time predictions for the straight pipe over the range of discharges studied. It can be observed that the optimised ADE and ADZ travel times are highly comparable with the volumetric travel times. The average percentage difference between the estimated travel times and the volumetric travel times is -2.27 % for the ADE dataset; 2.18 % for the ADZ dataset. Note that the error bars for the variations of the optimised travel times within repeat runs are not shown. This is because the variations are so negligible that one standard deviation of the variations is smaller than 0.5 % of the mean value.
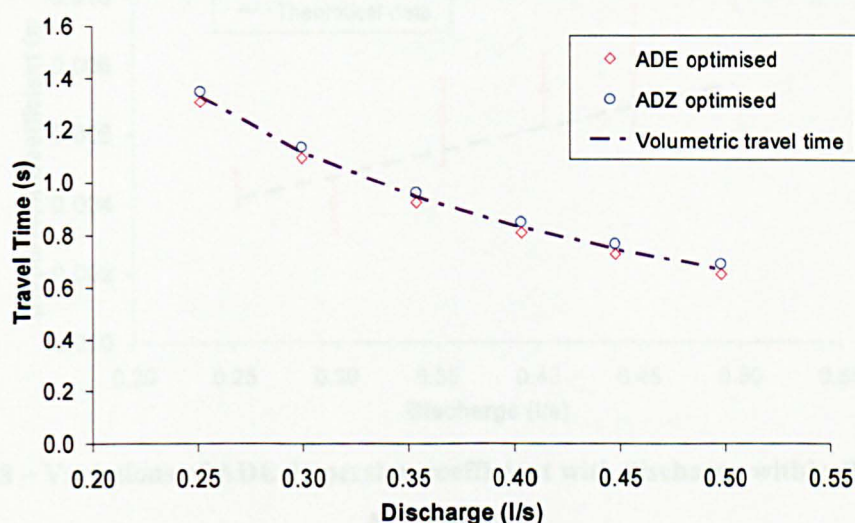
Figure 4.7 – Variations of ADE and ADZ travel times with discharge within the 24 mm ID straight pipe

4.3.1.2 Dispersion Coefficient – Straight Pipe

Variations of the optimised dispersion coefficient with discharge within the straight pipe are presented in Figure 4.8, together with the theoretical dispersion coefficient values. It is evident that the optimised parameter appears to be a linear relationship with discharge, although there is a data point corresponding to a flowrate of 0.3 l/s that deviates from the relationship. No explanation can be offered for this anomaly. The relationship that dispersion coefficient increases with discharge is expected because longitudinal dispersion in straight pipe flows is primarily governed by differential advection and higher discharge would encourage larger velocity gradient across the pipe cross section.

The variations of the value over repeat runs are significantly higher than those of the travel times. For the dispersion coefficient of the straight pipe, one standard deviation of the value within repeat runs was approximately 10 % of the mean value throughout the present laboratory data. This may be explained by that the coefficient values are very small and a small change in the profile shape due to the manual dye injection and instrument noise may result in this variation. The shape of the predicted profile is determined by dispersion coefficient whilst travel time defines the centroid of the profile, which is a function of flowrate in straight pipes. Compared with the Taylor's values, the optimised coefficients seem to be approximately 20 % higher, except the data point corresponding to a discharge of 0.3 l/s.
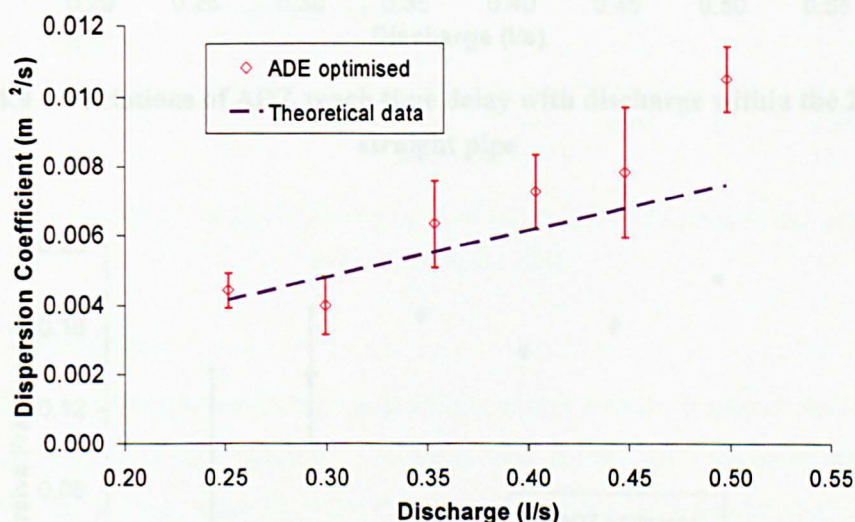
Figure 4.8 – Variations of ADE dispersion coefficient with discharge within the 24 mm ID straight pipe

4.3.1.3 Reach Time Delay and Dispersive Fraction – Straight Pipe

Values of the ADZ reach time delay for the straight pipe are plotted against discharge in Figure 4.9. The data and the error bars representing the variations between repeat tests show an inverse relationship with discharge. However, it is not clearly understood the inverse relationship between the error bar and discharge. The dispersive fraction appears to be directly proportional to discharge in the straight pipe, shown in Figure 4.10. This may be expected because if dispersion coefficient increases with discharge, dispersive fraction should also follow the trend with respect to discharge. The two parameters are indicative of the degree of dispersion in a flow. Because of the reach time delay data, there are noticeable variations between repeat tests at the two lowest discharges in the dispersive fraction dataset.
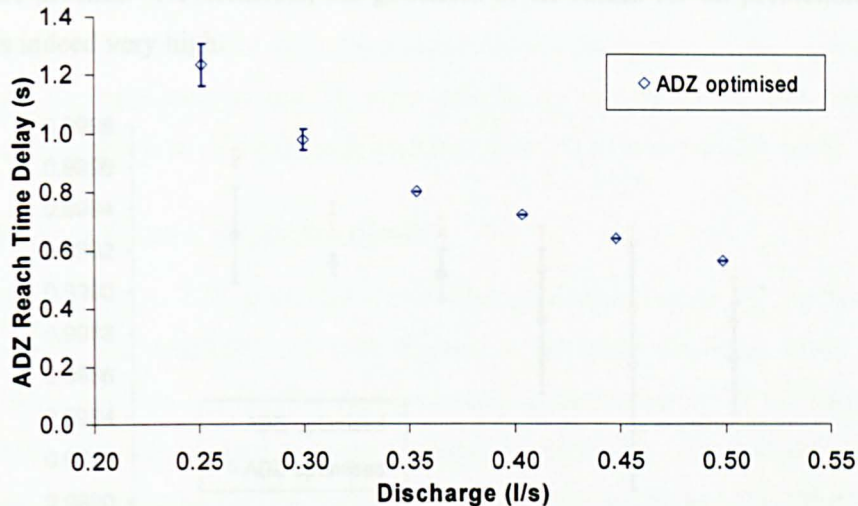
Figure 4.9 – Variations of ADZ reach time delay with discharge within the 24 mm ID straight pipe
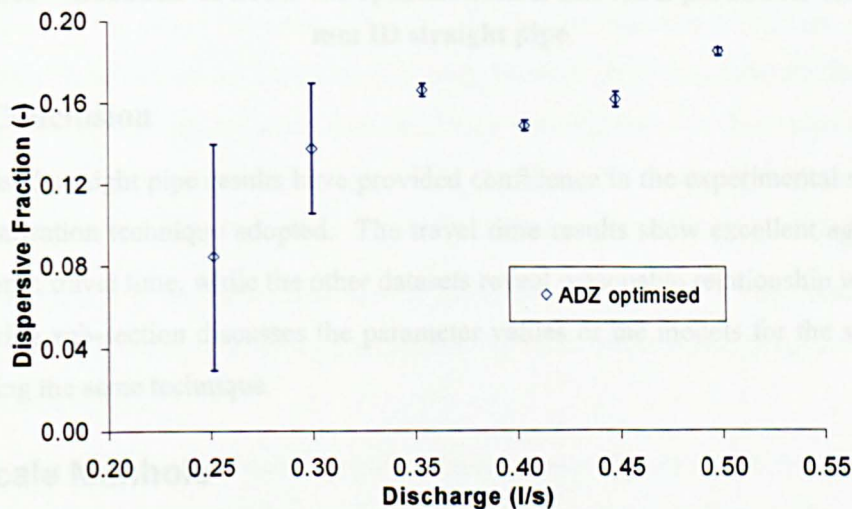
Figure 4.10 – Variations of ADZ dispersive fraction with discharge within the 24 mm ID straight pipe

4.3.1.4 Goodness of Fit – Straight Pipe

The optimised concentration predictions for the straight pipe flow made by the two models display excellent fit to the measured downstream profiles (Figure 4.11). For the profiles analysed, the average R_t^2 value yields 0.9992 and 0.9989 for the ADE and ADZ model predictions respectively. It may be noticed that the goodness of fit, in terms of R_t^2, of the ADE predictions appears to be marginally higher than that of the ADZ predictions. In both models, the goodness of fit slightly decreases as discharge increases; larger variations in the value between repeat runs can be observed at high discharges. This might be caused by fewer data

points in the profiles. Nevertheless, the goodness of fit values for all predictions in the pipe flow case is indeed very high.
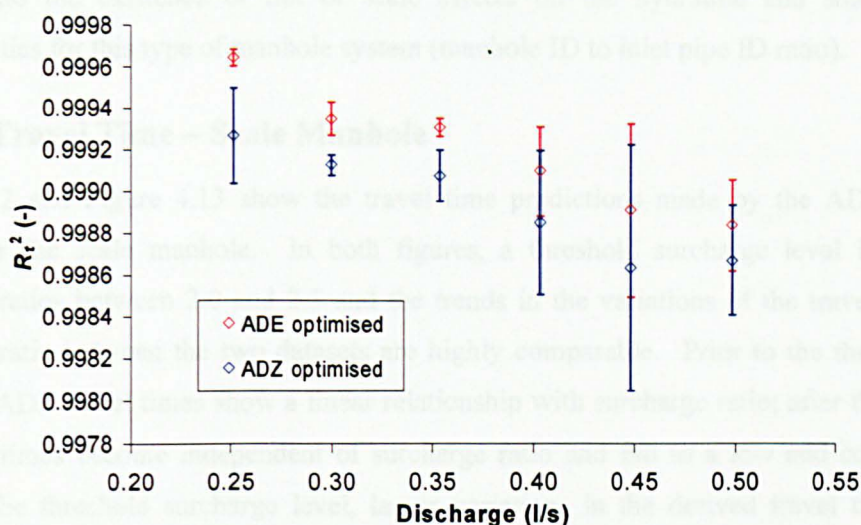
Figure 4.11 – Goodness of fit for the optimised ADE and ADZ parameter sets of the 24 mm ID straight pipe

4.3.1.5 Conclusion

The optimised straight pipe results have provided confidence in the experimental set-up as well as the optimisation technique adopted. The travel time results show excellent agreement with the volumetric travel time, while the other datasets reveal reasonable relationship with discharge. The following sub-section discusses the parameter values of the models for the scale manhole derived using the same technique.

4.3.2 Scale Manhole

Previous research of longitudinal dispersion within the prototype (the 800 mm ID manhole) showed an interesting solute transport characteristic when the tracer data was analysed using the optimisation procedure (Guymer *et al.*, 2005; also see example in Figure 2.19). A threshold surcharge level was identified, at which the travel times indicated a sharp transition between pre- and post-threshold levels; at surcharge levels below the threshold, the travel times increased linearly with surcharge; above the threshold level, the travel times dropped to a low and constant level. This characteristic hydraulic behaviour forms an interesting test for the analysis of the scale manhole model data.

This section presents the optimised mixing parameters for the scale model. To highlight the effects of the manhole, a mid-point from the pre-threshold surcharge depth range, termed mid-point surcharge depth in this thesis, (Surcharge ratio, S, of 1.17) and a mid-point from the post-

threshold dataset (Surcharge ratio, S, of 3.27) are compared with the straight pipe data. Further comparison of the manhole data with the derived mixing parameters of the prototype provides insights into the existence or not of scale effects on the hydraulic and solute transport characteristics for this type of manhole system (manhole ID to inlet pipe ID ratio).

4.3.2.1 Travel Time – Scale Manhole

Figure 4.12 and Figure 4.13 show the travel time predictions made by the ADE and ADZ models for the scale manhole. In both figures, a threshold surcharge level is evident at surcharge ratios between 2.0 and 2.5 and the trends in the variations of the travel times with surcharge ratio between the two datasets are highly comparable. Prior to the threshold, both ADE and ADZ travel times show a linear relationship with surcharge ratio; after the transition, the travel times become independent of surcharge ratio and fall to a low and constant level. Close to the threshold surcharge level, larger variations in the derived travel time between repeat runs can be observed. This may be explained by the hydraulic transition which occurred in the region of the ratios between 2.0 and 2.5. In the transitional region, the hydraulic condition was observed to be unstable, changing between pre- and post-threshold hydraulic patterns; this instability disappeared when surcharge was increased or decreased to a level that was clearly outside of the transitional region. The pre- and post-threshold flow field images can be found in Chapter 5. Both travel time results show an inverse relationship with discharge.

Careful examination of the travel time results suggests that the ADZ travel times for the scale manhole are approximately two times greater than the ADE travel times. Explanation for this is given in Section 4.3.4.2.

To examine the effects of the scale manhole on travel times, the ADE and ADZ travel times of the mid-point surcharge data points corresponding to pre- and post-threshold are plotted with the straight pipe results in Figure 4.14. Similar to the straight pipe data, the mid-point surcharge ADE and ADZ travel times for the scale manhole show an inverse relationship with discharge. Comparison of the straight pipe and the scale manhole data suggests that the effects of the manhole on travel time at pre-threshold are significant. The ADE pre-threshold travel times are approximately eight times the pipe travel times; while the ADZ travel times increase four-fold due to the existence of the manhole. Post-threshold, there is no noticeable difference in the ADE travel time between the manhole and the straight pipe; whereas the ADZ post-threshold values are two times greater than the pipe values. It should be borne in mind that the manhole travel time data plotted against discharge represents the mid-point surcharge points corresponding to the range of pre-threshold and post-threshold surcharge depths considered in

this study. The mid-point surcharge value should not be regarded as the average travel time for a particular hydraulic regime.

Further discussion of the usefulness of the derived parameters is presented in Section 4.3.4.
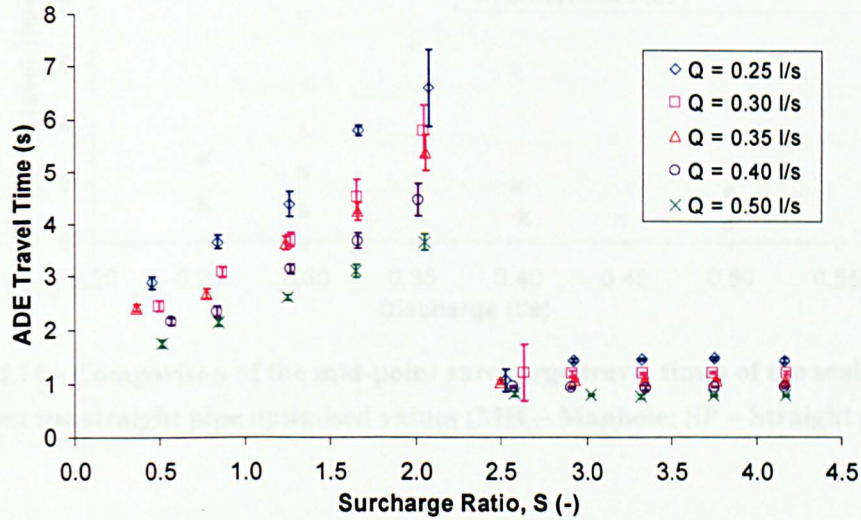
Figure 4.12 - Variations of ADE travel time with surcharge ratio within the scale manhole
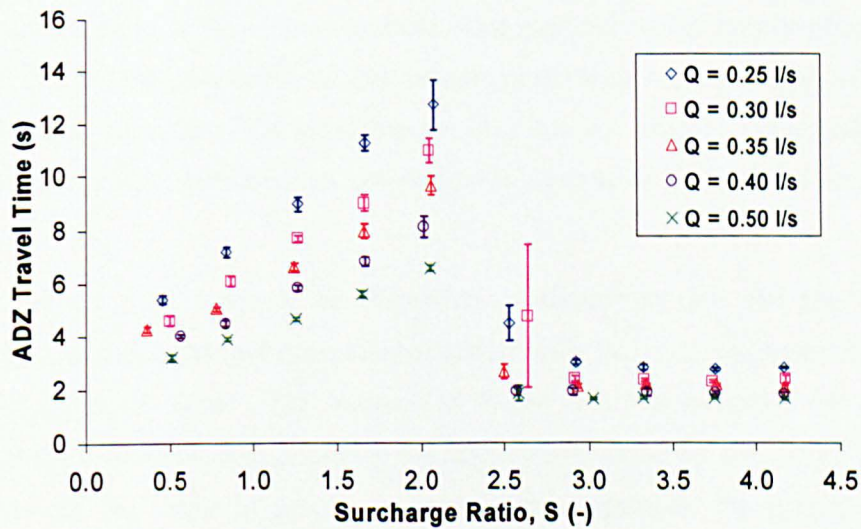
Figure 4.13 - Variations of ADZ travel time with surcharge ratio within the scale manhole
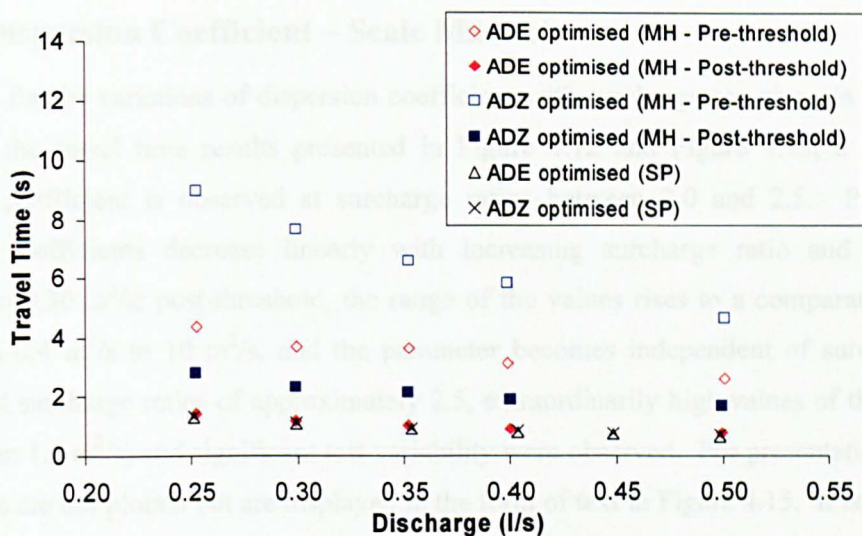
Figure 4.14 - Comparison of the mid-point surcharge travel times of the scale manhole with the straight pipe optimised values (MH – Manhole; SP – Straight pipe)

4.3.2.2 Dispersion Coefficient – Scale Manhole

The results for the variations of dispersion coefficient with surcharge are given in Figure 4.15. Similar to the travel time results presented in Figure 4.12 and Figure 4.13, a transition in dispersion coefficient is observed at surcharge ratios between 2.0 and 2.5. Pre-threshold, dispersion coefficients decrease linearly with increasing surcharge ratio and range from 0.05 m^2/s to 0.30 m^2/s; post-threshold, the range of the values rises to a comparatively higher level, from 0.4 m^2/s to 10 m^2/s, and the parameter becomes independent of surcharge ratio. Note that at surcharge ratios of approximately 2.5, extraordinarily high values of the parameter (greater than 1.6 m^2/s) and significant test variability were observed. For presentation purposes, these points are not plotted but are displayed in the form of text in Figure 4.15. It is thought that these high values are the result of the effects of the transitional hydraulic regime. However, no explanation can be offered as why these values are considerably higher than either the pre- or post-threshold values.

The variations in the coefficient between repeat tracer tests in post-threshold are markedly high in comparison to those under the pre-threshold conditions. The average standard deviation for the pre-threshold coefficients approximates to 10 % of the mean value, whereas this value is doubled, approximately 20 %, in post-threshold. One explanation that may be offered is that the ADE travel time of the post-threshold downstream profiles appears to be approximately three times smaller than the value of the pre-threshold. According to the sensitivity study of the ADE model (Dutton, 2004), larger variations between repeat tests are to be expected for smaller travel times.

The effects of the scale manhole on dispersion coefficient in pre- and post-threshold are quantified by comparing the mid-point surcharge data with the optimised values for the straight pipe, shown in Figure 4.16. The comparison shows that pre-threshold, the trends in the variations of the coefficient with discharge are highly comparable but the coefficient values for the manhole are one order of magnitude greater; post-threshold, the optimised dispersion coefficient (the solid red symbols) varies with discharge in a non-systematic fashion, as opposed to the linear function revealed in the straight pipe data. The post-threshold data is generally two orders of magnitude greater than the straight pipe results. Discussion of the usefulness of the derived scale manhole coefficients is held in Section 4.3.4.
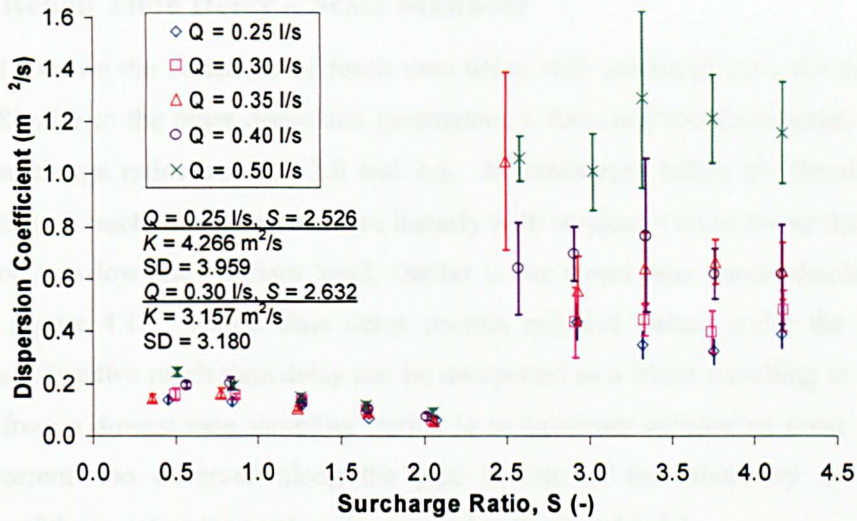
Figure 4.15 – Variations of ADE dispersion coefficient with surcharge ratio within the scale manhole
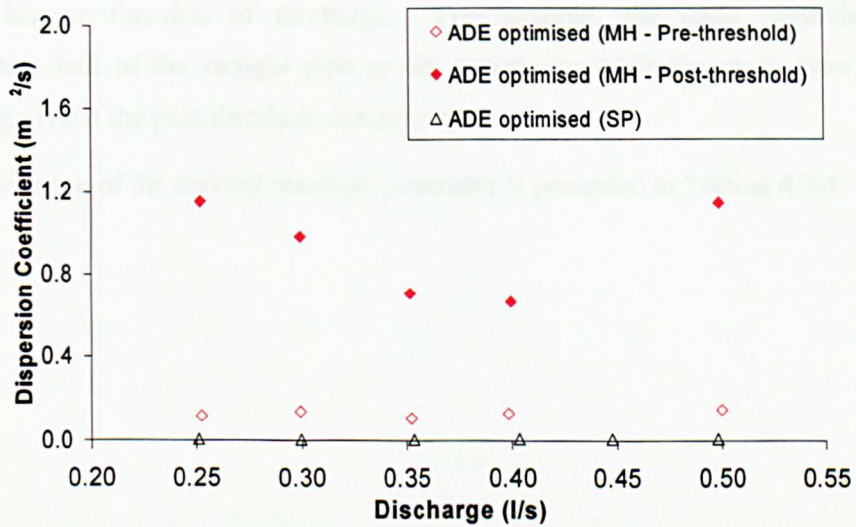
Figure 4.16 – Comparison of the mid-point surcharge dispersion coefficients of the scale manhole with the straight pipe optimised values (MH – Manhole; SP – Straight pipe)

4.3.2.3 Reach Time Delay – Scale Manhole

Figure 4.17 shows the variations of reach time delay with surcharge ratio for the scale model dataset. Similar to the other dispersion parameters, a threshold transition exists in reach time delay at surcharge ratios between 2.0 and 2.5. At surcharges below the threshold surcharge depth, values of reach time delay increase linearly with surcharge ratio; above the threshold, the values drop to a low and constant level, similar to the travel time results displayed in Figure 4.12 and Figure 4.13. Reach time delay reveals negative values under the post-threshold conditions. Negative reach time delay can be interpreted as a tracer travelling in a reverse-flow direction from a downstream sampling station to an upstream monitoring point. However, no reverse current was observed along the pipe section of the laboratory system. Further discussion of the negative time values is provided in Section 4.3.4.2.

Comparison of the mid-point surcharge reach time delay values in pre- and post-threshold and the values for the straight pipe is given in Figure 4.19. All of the three laboratory measurements show an inverse function of discharge. Pre-threshold, the scale manhole values are approximately half of the straight pipe model parameter; while the reach time delay values become negative at the post-threshold conditions.

Further discussion of the derived manhole parameter is presented in Section 4.3.4.
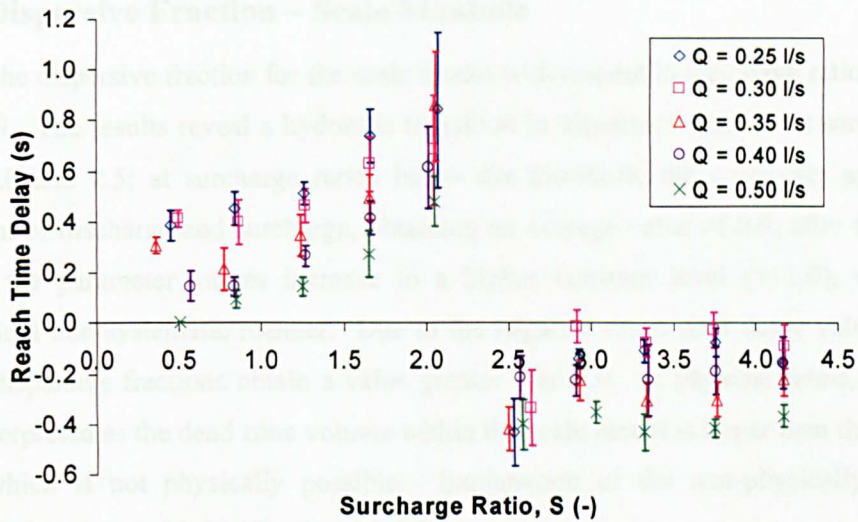
Figure 4.17 – Variations of reach time delay with surcharge ratio within the scale manhole
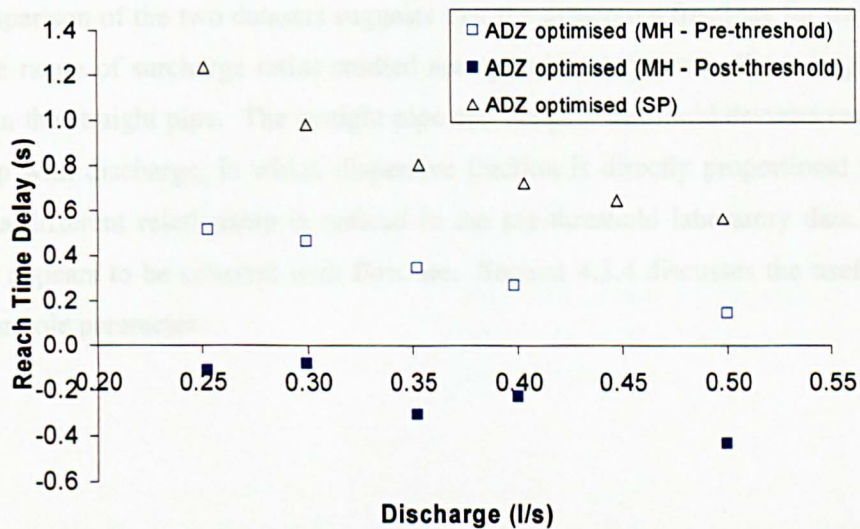
Figure 4.18 - Comparison of mid-point surcharge reach time delay with discharge within the straight pipe and the scale manhole (MH – Manhole; SP – Straight pipe)

4.3.2.4 Dispersive Fraction – Scale Manhole

Values of the dispersive fraction for the scale model with respect to surcharge ratio are given in Figure 4.19. The results reveal a hydraulic transition in dispersive fraction at surcharge ratios between 2.0 and 2.5; at surcharge ratios below the threshold, the parameter appears to be independent of discharge and surcharge, obtaining an average value of 0.9; after the hydraulic transition, the parameter values increase to a higher constant level (> 1.0), varying with discharge in a non-systematic manner. Due to the negative reach time delay values, the post-threshold dispersive fractions obtain a value greater than 1.0. In physical terms, these values may be interpreted as the dead zone volume within the scale model is larger than the total model volume, which is not physically possible. Explanation of the non-physically meaningful parameter values is provided in Section 4.3.4.2.

The mid-point surcharge dispersive fractions are compared with the straight pipe data in Figure 4.20. Comparison of the two datasets suggests that the dispersive fractions for the scale model through the range of surcharge ratios studied are approximately seven times larger than those measured in the straight pipe. The straight pipe and the post-threshold datasets reveal the same relationship with discharge, in which dispersive fraction is directly proportional to discharge. However, a different relationship is noticed in the pre-threshold laboratory data. The model coefficient appears to be constant with flowrate. Section 4.3.4 discusses the usefulness of the derived manhole parameter.
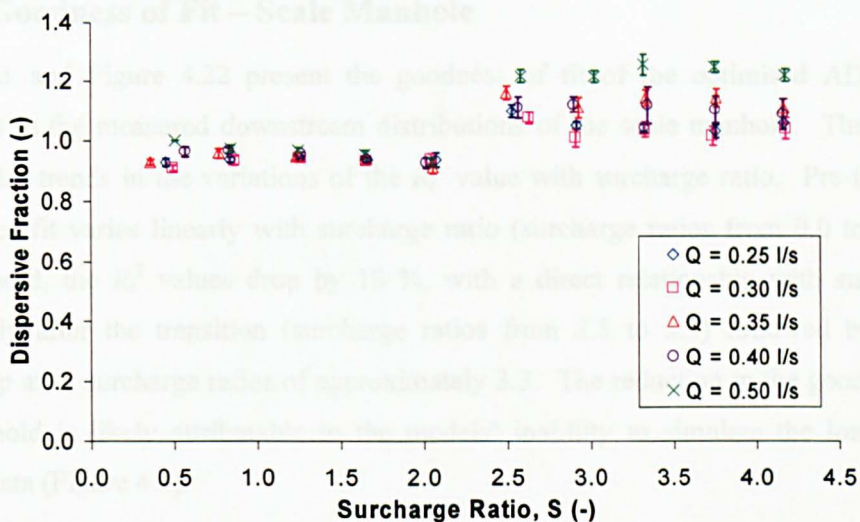
Figure 4.19 – Variations of dispersive fraction with surcharge ratio within the scale manhole
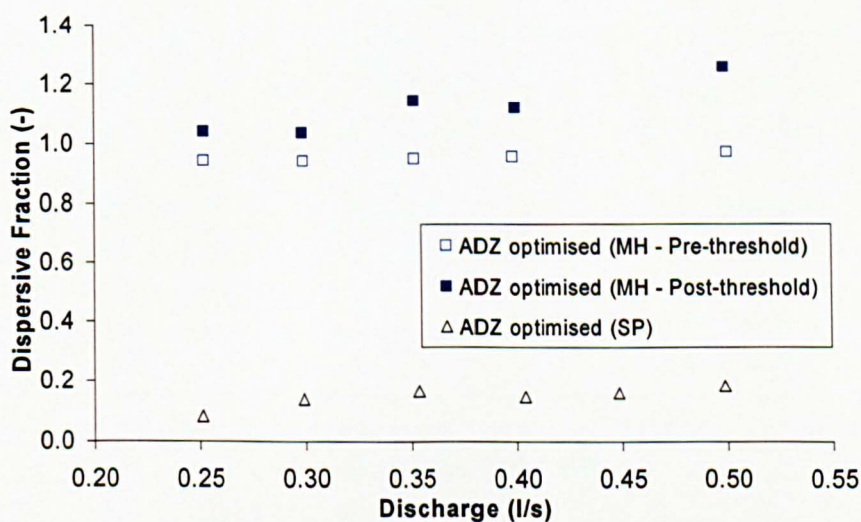
Figure 4.20 - Variations of mid-point surcharge dispersive fraction with discharge within the straight pipe and the scale manhole (MH – Manhole; SP – Straight pipe)

4.3.2.5 Goodness of Fit – Scale Manhole

Figure 4.21 and Figure 4.22 present the goodness of fit of the optimised ADE and ADZ predictions to the measured downstream distributions of the scale manhole. The two figures show similar trends in the variations of the R_t^2 value with surcharge ratio. Pre-threshold, the goodness of fit varies linearly with surcharge ratio (surcharge ratios from 0.0 to 2.0); whilst post-threshold, the R_t^2 values drop by 10 %, with a direct relationship with surcharge ratio immediately after the transition (surcharge ratios from 2.5 to 3.3) followed by an inverse relationship after surcharge ratios of approximately 3.3. The reduction in the goodness of fit in post-threshold is likely attributable to the models' inability to simulate the long tail of the recorded data (Figure 4.5).

Comparing the two solute transport model predictions, the ADZ predictions are generally in better agreement with the observations, especially for the pre-threshold profiles. The reason for this is explained in Section 4.3.4.2.
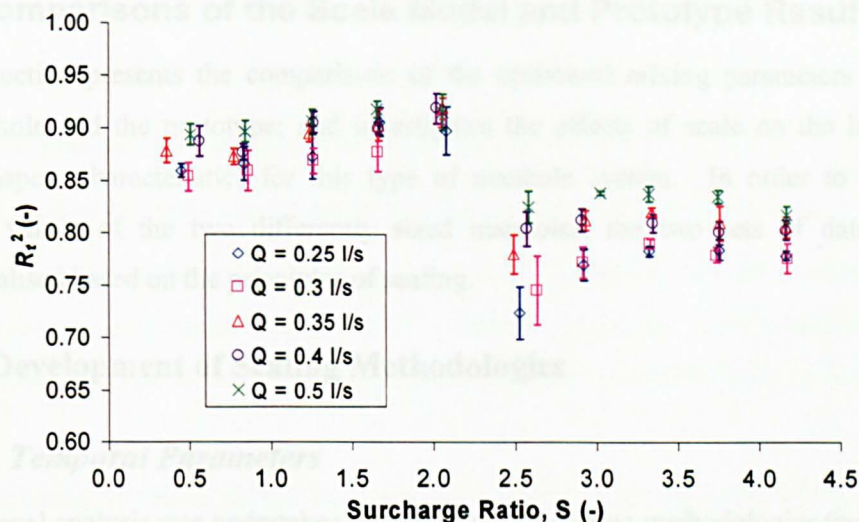
Figure 4.21 – Goodness of fit for the optimised ADE parameter sets of the scale manhole
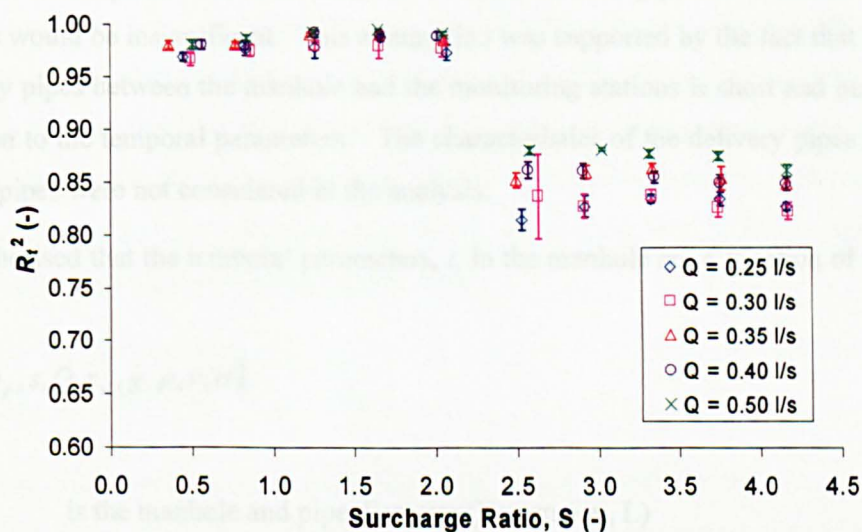
Figure 4.22 – Goodness of fit for the optimised ADZ parameter sets of the scale manhole

4.3.3 Comparisons of the Scale Model and Prototype Results

This sub-section presents the comparisons of the optimised mixing parameters between the scale manhole and the prototype; and investigates the effects of scale on the hydraulic and solute transport characteristics for this type of manhole system. In order to compare the optimised values of the two differently sized manholes, the two sets of data were non-dimensionalised based on the principles of scaling.

4.3.3.1 Development of Scaling Methodologies

4.3.3.1.1 Temporal Parameters

A dimensional analysis was undertaken to determine the scaling methodologies for the temporal parameters, travel time and reach time delay, derived from the ADE and ADZ models. In the analysis, an assumption was made that the effects of the pipe on the derived temporal parameters would be insignificant. This assumption was supported by the fact that the length of the delivery pipes between the manhole and the monitoring stations is short and hence has little contribution to the temporal parameters. The characteristics of the delivery pipes and the flow within the pipes were not considered in the analysis.

It is hypothesised that the temporal parameters, t, in the manhole are a function of the variables below:

$$t = f\left(D, D_p, s, Q, \tau_w, g, \rho, \nu, \sigma\right) \qquad\qquad 4.2$$

where:

D, D_p	is the manhole and pipe diameter (Dimension, L)
s	is the surcharge (Dimension, L)
Q	is the flowrate through the manhole (Dimensions, L^3T^{-1})
τ_w	is the shear stress between the manhole and fluid (Dimensions, $ML^{-1}T^{-2}$)
g	is the gravitational acceleration (Dimensions, LT^{-2})
ρ	is the fluid density (Dimensions, ML^{-3})
ν	is the kinematic viscosity of the fluid (Dimensions, L^2T^{-1})
σ	is the surface tension (Dimension, MT^{-2})

The Buckingham Π theorem was used to solve the dimensional analysis and Q, D and ρ were considered as the repeating variables, or dependent variables. The repeating variables are combined with each other variable to form a dimensionless group. The selection of the repeating variables was based on Douglas *et al.* (1985) and ASCE manuals and reports on engineering practice No. 97 (2000):

1. The number of repeating variables equals the number of primary dimensions in the function;

2. The repeating variables are not dimensionless;

3. No two repeating variables should have the same dimensions;

4. The dependent variables should not form a dimensionless group themselves;

5. The dependent variables must include all the fundamental dimensions involved and should be chosen from different categories of variables (geometry, flow conditions and fluid properties etc.) and at least one should be a geometric variable, such as a representative length;

6. The repeating variables should have a substantial effect on the independent variables, i.e. the terms not identified as being the repeating variables.

The functional relationship between non-dimensional parameters is described in Equation 4.3. The first term on the left hand side of the equation indicates the ratio of the temporal parameters to volumetric travel time (volume over discharge); D_p/D and s/D are the geometric attributes of the manhole system; the third term on the right hand side is Prandtl velocity ratio, defined as the ratio of inertia force to shear force due to a solid boundary; the fourth and fifth terms represent Froude number and Reynolds number respectively; and the last term is Weber number, defined as the ratio of inertia force to surface tension force.

$$\frac{Qt}{D^3} = f\left(\frac{D_p}{D}, \frac{s}{D}, \frac{D^4\tau_w}{\rho Q^2}, \frac{D^5 g}{Q^2}, \frac{Dv}{Q}, \frac{\rho Q^2}{D^3 \sigma} \right) \qquad 4.3$$

According to the principles of scaling, the value of Qt/D^3 will be the same in two similar systems if the value of all dimensionless groups for the two systems on the right hand side of the equation is identical (ASCE manuals and reports on engineering practice No. 97, 2000). The two differently scaled manholes are geometrically similar and were scaled using Froude number similarity. Therefore, similarity of D_p/D, s/D and D^5g/Q^2 terms between the two systems exist. However, it is not possible to satisfy Froude number and Reynolds number similarities simultaneously because each defines unique relationship between the scale ratios of length, time and velocity (and temperature if the flow condition is non-isothermal). In a free surface flow where the governing parameter for the flow is Froude number, the dependence of the flow characteristics on Reynolds number become insignificant once the flow is in the fully turbulent regime. This is because the viscosity effect of the fluid is no longer significant and barely makes an impact on the flow characteristics. Reynolds number may be ignored in Equation 4.3. Similarly for Prandtl velocity ratio and Weber number, when the inertia force of the fluid is large the wall shear stress and surface tension force are insignificant to the

characteristics of the flow. As a result, these two terms may also be neglected in the equation. Equation 4.3 can be simplified and rewritten as in Equation 4.4. The assumptions made in this scaling exercise will be re-assessed in Chapter 7.

$$\frac{Qt}{D^3} = f\left(\frac{D_p}{D}, \frac{s}{D}, \frac{D^5 g}{Q^2}\right) \qquad\qquad 4.4$$

If there is no scale effect in the manhole, the value of the Qt/D^3 will be identical in the two differently sized manhole models. For this reason, all temporal parameters were non-dimensionalised by the volumetric residence time to examine the effects of scale on the temporal model coefficients.

4.3.3.1.2 Dispersion Coefficient

A dimensional analysis was performed to determine the non-dimensionalised factor for scaling dispersion coefficient. The analysis was carried out in a similar fashion as the dimensional analysis for the temporal parameters in Section 4.3.3.1.1. The same assumption was made that the effect of the pipe on the derived coefficient is ignored. Therefore, consideration was not given to the characteristics of the delivery pipes and the flow within the pipes in the analysis.

It is inferred that the dispersion coefficient, K, for the manhole is a function of the variables, shown in Equation 4.5. The Buckingham Π theorem approach was adopted in the analysis. Q, D and ρ were selected as the repeating variables based on the guidelines highlighted above.

$$K = f\left(D, D_p, s, Q, \tau_w, g, \rho, \nu, \sigma\right) \qquad\qquad 4.5$$

Equation 4.6 shows the functional relationship between dimensionless groups derived from this analysis. It can be noticed that the dimensionless groups DK/Q (dispersion coefficient, Equation 4.6) and Qt/D^3 (temporal parameters, Equation 4.3) are a function of the same non-dimensional parameters. Therefore, as in the dimensional analysis for the derived temporal parameters in Section 4.3.3.1.1, Equation 4.6 can be simplified to Equation 4.7. If the scaling law is valid, similarity of the values for the dimensionless group, DK/Q, will exist between the two manhole models.

$$\frac{DK}{Q} = f\left(\frac{D_p}{D}, \frac{s}{D}, \frac{D^4 \tau_w}{\rho Q^2}, \frac{D^5 g}{Q^2}, \frac{D\nu}{Q}, \frac{\rho Q^2}{D^3 \sigma}\right) \qquad\qquad 4.6$$

$$\frac{DK}{Q} = f\left(\frac{D_p}{D}, \frac{s}{D}, \frac{D^5 g}{Q^2}\right) \qquad\qquad 4.7$$

In river mixing research, the dispersion coefficient, K, is usually normalised with respect to mean water depth, h, and bed shear velocity, u^*, allowing the normalised parameters between rivers with different flow conditions to be compared (Rutherford, 1994). The two variables are used because the value of the resultant dimensionless parameter, K/hu^*, can be compared to the theoretical value derived by Elder (1958). Taylor (1954) also used the same dimensionless group, with different definition of the length scale, to derive an empirical value for dispersion coefficient in pipe flows. The length scale was defined as the pipe radius, r.

To date, there is limited research regarding scaling dispersion coefficients in open channel flows and flows in urban drainage structures. The discussion here has led to two possible approaches to non-dimensionalising dispersion coefficient and both approaches seem to have some uncertainty for the use of scaling dispersion coefficient. The first approach considered dimensional analysis in which the result may not be useful if the flow and/or mixing process are not adequately understood so that the variables are not properly identified (ASCE manuals and reports on engineering practice No. 97, 2000). The second approach is usually adopted in open channel and pipe flows for the comparisons of dispersion coefficient. However, the dimensionless group was not derived from the principle of scaling and therefore may not be appropriate to be used for studying the effects of scale in the manhole. In addition, the governing mixing mechanism in the manhole is not driven by the shear stress due to solid boundaries, but is due to the shear layer of the submerged jet in association with the circulation zone. Therefore, it is thought that the first approach which is based on dimensional analysis is more appropriate for the use of scaling dispersion coefficient. Comparison of the non-dimensionalised parameters between the two physical manholes is presented in the following sub-section.

4.3.3.1.3 Dispersive Fraction

Dispersive fraction is a dimensionless parameter and independent of scale. This may be explained by dispersive fraction is the ratio of residence time over travel time and the non-dimensionalisation factors for the two temporal parameters would cancel out each other.

4.3.3.1.4 Froude Number Similarity Discharge

When Froude number similarity is used for scaling models, the discharge should be scaled using Equation 4.8 and Equation 4.9. Using the two equations, the Froude number similarity discharges, hereafter called Froude scaled discharges, of the scale manhole with respect to the prototype are tabulated in Table 4.3.

$$\lambda_L = \frac{L_{model}}{L_{prototype}} \qquad\qquad 4.8$$

$$\lambda_Q = \left(\frac{L_{model}}{L_{prototype}}\right)^{2.5} \qquad\qquad 4.9$$

where:

$L_{model,\ prototype}$ is the dimensions of the scale model and prototype

$\lambda_L,\ \lambda_Q$ is the length scale factor and the discharge scale factor respectively

Discharge considered in the Scale Manhole (l/s)	Froude Scaled Discharge with respect to the Prototype (l/s)	Discharge considered in the Prototype (l/s)
0.25	6.45	1
0.30	7.74	2
0.35	9.03	4
0.40	10.32	6
0.50	12.90	8

Table 4.3 – Discharge conditions considered in the scale manhole and prototype experiments

4.3.3.2 Results

4.3.3.2.1 ADE and ADZ Travel Times

Figure 4.23 presents the effects of normalisation on each set of travel time data and comparisons of the normalised ADE and ADZ travel times for the scale model and the prototype. It is evident that after normalisation, the post-threshold travel times of each dataset collapse onto four different curves, one curve for each set of the post-threshold data. However, in the pre-threshold regime, the figures suggest that the non-dimensionalised prototype travel times vary as a function of discharge; while the scale manhole datasets vary with flowrate in a non-systematic manner.

Comparisons of the non-dimensionalised travel times between the two manholes show that the trends in the variations of the travel times as a function of surcharge ratio are highly comparable; a linear relationship is evident at pre-threshold, while the travel times stay at a low and constant level in the post-threshold regime. In addition, the threshold surcharge levels occur at similar surcharge ratios; in the scale manhole, it appears to exist at a surcharge ratio between 2.0 and 2.5, compared with a surcharge ratio of approximately 2.5 in the prototype. However, more careful examination of Figure 4.23 suggests that the two datasets do not overlap; for example

the discharge datasets of 0.25 l/s (6.45 l/s) and 0.30 l/s (7.74 l/s) for the scale manhole are expected to fit between the discharge datasets of 6 l/s and 8 l/s for the prototype according to the Froudian scaled discharge. The ADE and ADZ travel times for the scale manhole appear to be consistently greater than the values for the prototype. Explanation for the discrepancies in the travel times between the two sets of laboratory data is given in Section 4.3.4.1.

4.3.3.2.2 Dispersion Coefficient

Normalised dispersion coefficients for the two manhole models are compared in Figure 4.24. The non-dimensionalisation with respect to D/Q (Section 4.3.3.1.2) results in non-systematic variations of the normalised parameter with discharge in both the scale manhole and prototype data. This is only with the exception of the prototype post-threshold dataset, in which the normalised parameter increases with discharge.

In both sets of data, it is evident that normalised dispersion coefficients in pre-threshold tend to decrease with increasing surcharge ratio. This relationship appears to continue in the prototype post-threshold data. For the scale model, the normalised parameter rises to a high level after the hydraulic transition. Careful comparison of the two manhole datasets suggests that pre-threshold, the values for the scale manhole are consistently smaller than those for the prototype (Figure 4.24b), except the data corresponding to the lowest surcharge ratios in the scale manhole model. Post-threshold, significant deviation of the two datasets can be observed, with the scale manhole data markedly higher than the prototype results. Further discussion of the comparisons of the parameters between the two manholes is presented in Section 4.3.4.1.

4.3.3.2.3 Reach Time Delay and Dispersive Fraction

Figure 4.25a presents the normalised reach time delay results of the two manhole datasets. It may be noticed that the non-dimensionalisation of the parameters for both manholes leads to a random variation with discharge; for example, in the prototype model, the dataset corresponding to a discharge of 2 l/s is consistently higher than the datasets corresponding to the other discharges for the same manhole. The same dataset is also consistently greater than the scale manhole results. The reason for these is not clearly realised.

The two sets of data (prototype and scale manhole) reveal distinct trends in the variations with surcharge ratio. For the prototype, an inverse relationship between the parameter and surcharge ratio throughout the entire range of surcharge ratios is observed. On the contrary, the scale model parameter shows a linear function with surcharge ratio in pre-threshold. This is with the exception of the data points corresponding to the lowest surcharge ratio ($S \sim 0.5$). Post-threshold, the scale model parameter values stay at a negative and constant level.

Similarly, the results of dispersive fraction for the two differently sized manholes shown in Figure 4.25b are also in poor agreement, in terms of the trend in the variations of dispersive fraction with surcharge ratio.

The following sub-section discusses and investigates the reasons for the discrepancies between the two differently scaled manhole data.
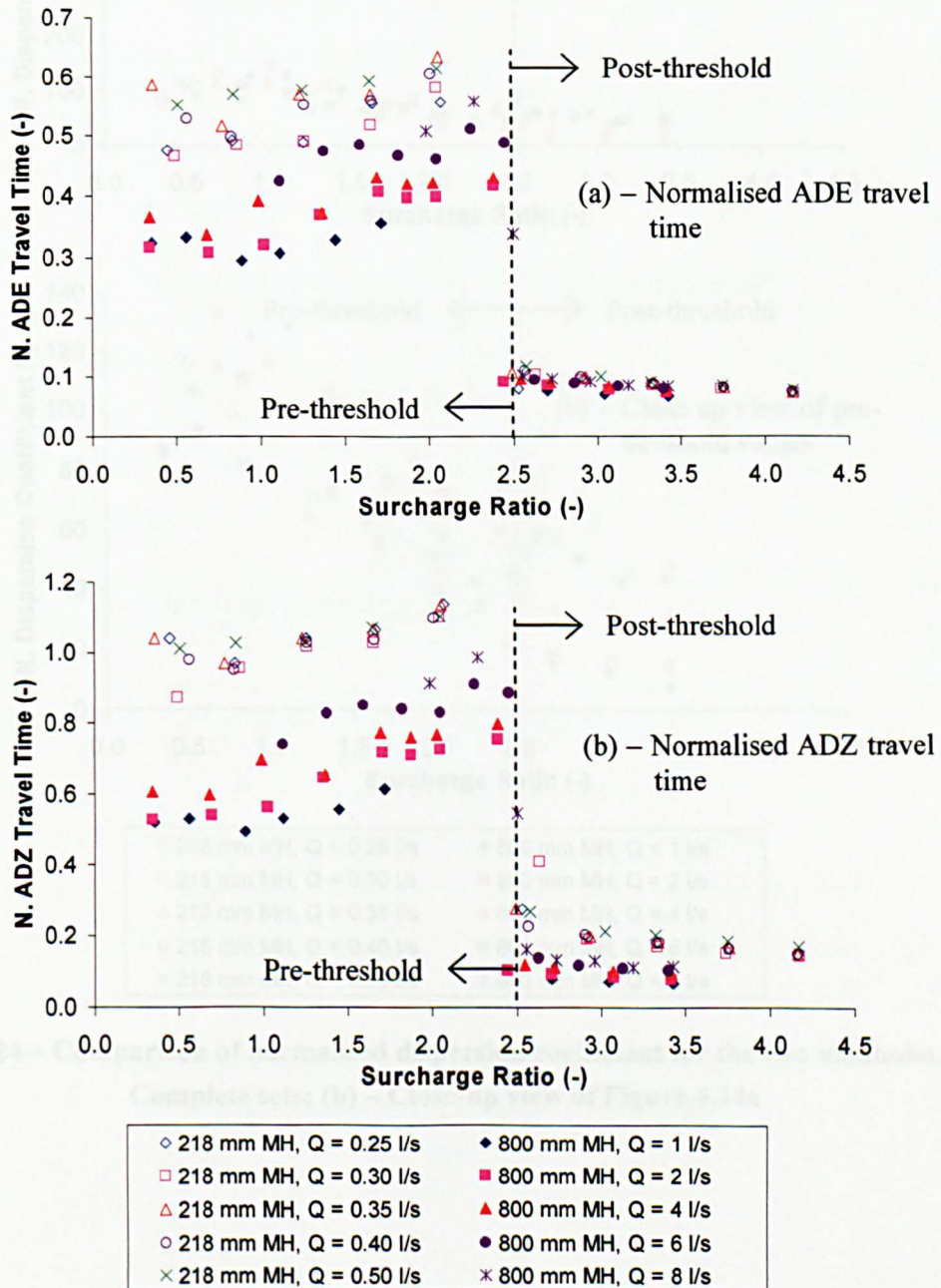
Figure 4.23 – Comparison of normalised travel times for the two manholes: (a) – ADE; (b) - ADZ
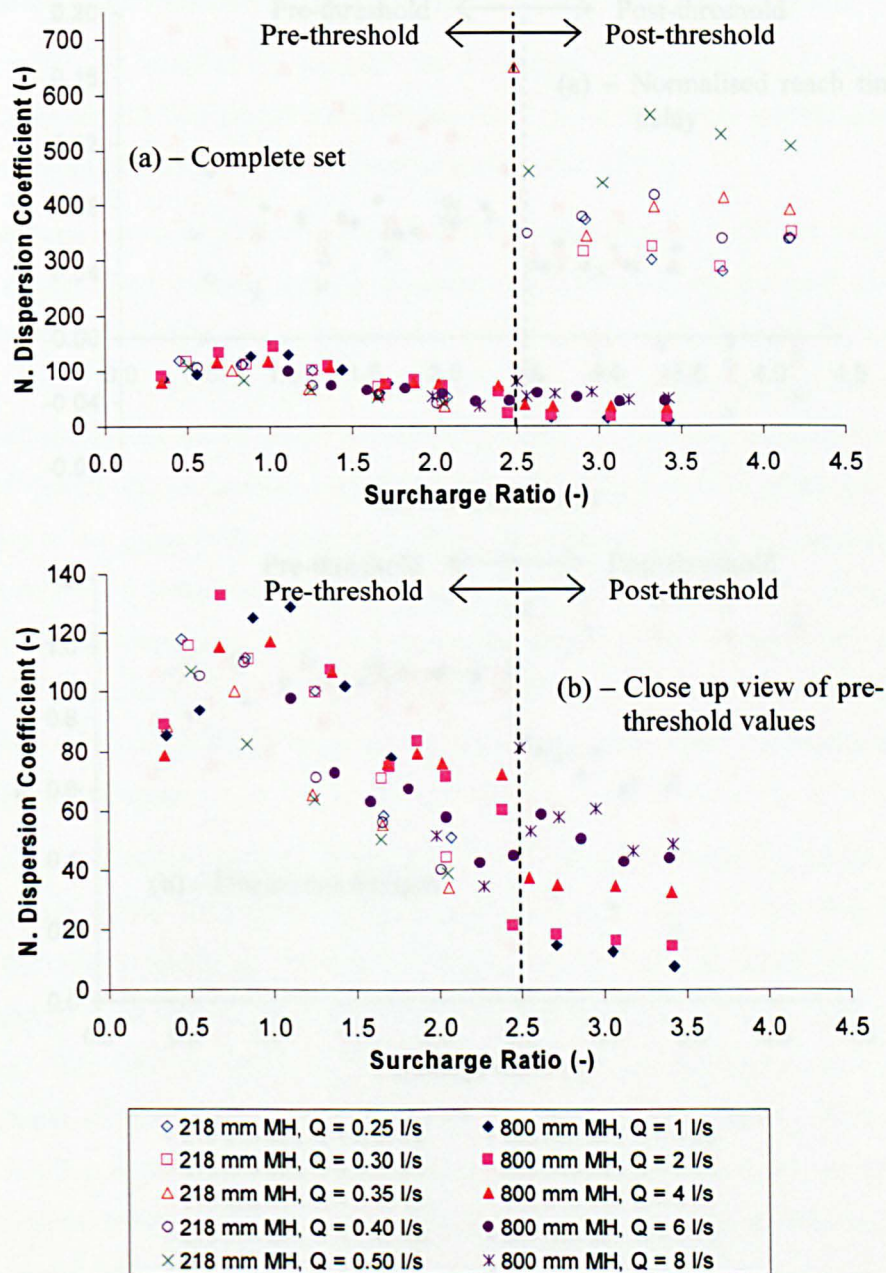
Figure 4.24 – Comparison of normalised dispersion coefficient for the two manholes: (a) – Complete sets; (b) – Close-up view of Figure 4.24a
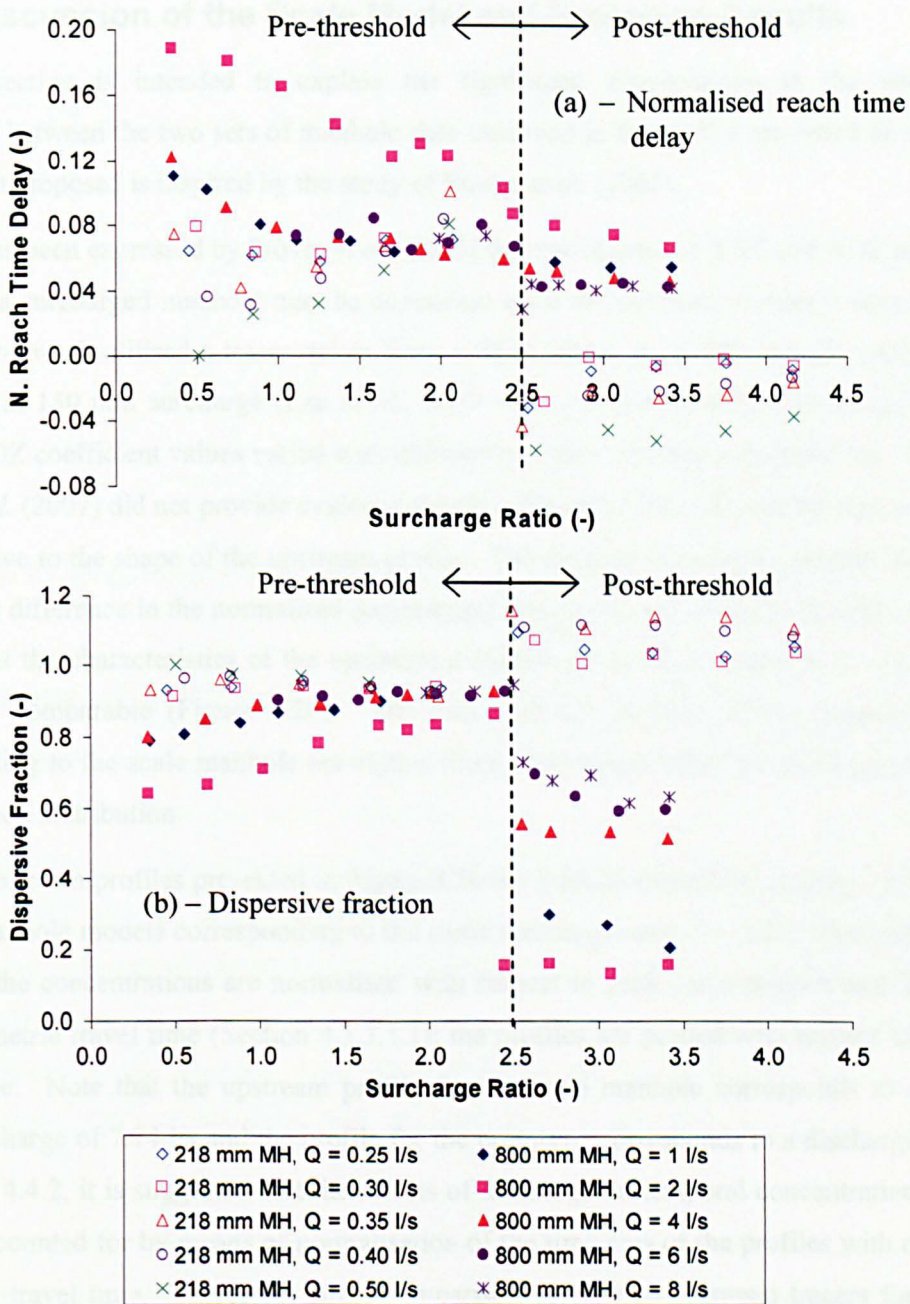
Figure 4.25 – Comparison of dispersion parameters for the two manhole datasets: (a) – Reach time delay; (b) – Dispersive fraction

4.3.4 Discussion of the Scale Model and Prototype Results

This sub-section is intended to explain the significant discrepancies in the normalised parameters between the two sets of manhole data observed in the results presented above. The explanation proposed is inspired by the study of Stovin *et al.* (2007).

Concern has been expressed by Stovin *et al.* (2007) that the optimised ADE and ADZ parameter values for a surcharged manhole may be dependent upon the upstream temporal concentration profile. The work utilised a tracer, taken from a CFD model of an 800 mm ID manhole (the prototype) at 150 mm surcharge (Lau *et al.*, 2007; also see Section 6.2), and proved that the derived ADZ coefficient values varied with differently shaped upstream distributions. However, Stovin *et al.* (2007) did not provide evidence showing the optimised ADE parameters values are also sensitive to the shape of the upstream profile. The findings of a more complete study may explain the difference in the normalised parameters between the two manhole datasets, as it was noticed that the characteristics of the upstream distributions in the two laboratory datasets are not highly comparable (Figure 4.26). The area and the duration of the upstream profile corresponding to the scale manhole are almost three times greater than the prototype upstream concentration distribution.

The two upstream profiles presented in Figure 4.26 are typical normalised upstream profiles for the two manhole models corresponding to the same surcharge ratio, $S \sim 2.05$. For comparative purposes, the concentrations are normalised with respect to peak concentration and the x-axis with volumetric travel time (Section 4.3.3.1.1); the profiles are plotted with respect to the first arrival time. Note that the upstream profile for the scale manhole corresponds to a Froude scaled discharge of 7.74 l/s and the profile for the prototype corresponds to a discharge of 2 l/s. In Section 4.4.2, it is suggested that the effects of discharge on temporal concentration profiles may be accounted for by means of normalisation of the time axis of the profiles with respect to volumetric travel time. Therefore, direct comparison of the two upstream tracers for the two differently sized manholes should be acceptable.
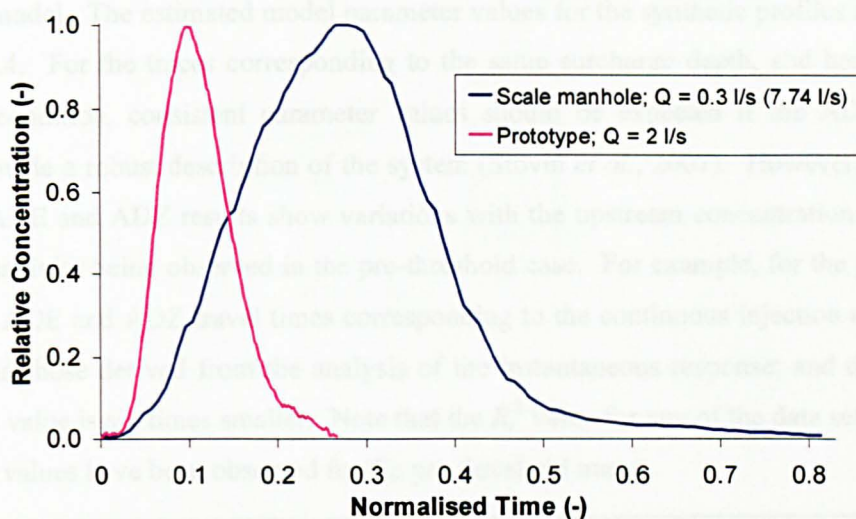
Figure 4.26 – Comparison of normalised upstream temporal concentration distribution of the two manhole models

4.3.4.1 Sensitivity to Upstream Concentration Distribution

The study to examine the effects of upstream concentration distribution on the derived ADE and ADZ optimised parameters has been undertaken using the experimental method published in Stovin *et al.* (2007). The current investigation has extended the scope of the previous study which examined two sample traces, generated from Lau *et al.* (2007) CFD prototype models corresponding to pre-threshold (150 mm) and post-threshold (300 mm) surcharge depths. Lau *et al.* (2007) generated traces in response to an instantaneous pulse for a wide range of surcharge depths using discrete phase modelling and the traces showed reasonably good agreement with published laboratory data. Details of Lau *et al.* (2007)'s work can be found in Section 6.2.

The present study investigated three differently shaped upstream conditions and consideration was given to an instantaneous pulse, a 10 s Gaussian profile (with a mean time of 5 s and a standard deviation of 1.5 s) and a 20 s continuous injection. The CFD simulated trace had been created to represent an instantaneous pulse response and the downstream distribution corresponding to the non-instantaneous upstream profiles was synthesised from the simulated instantaneous response using superposition (e.g. Figure 2.15). The optimisation procedure was applied to the pairs of upstream and downstream concentration distributions for the determination of the ADE and ADZ model parameters. The pre-defined parameter resolution adopted in the analysis is listed in Table 4.2.

Figure 4.27 presents the comparisons of the three synthesised downstream distributions with the optimised ADE and ADZ predictions for the pre- and post-threshold traces of the CFD

prototype model. The estimated model parameter values for the synthetic profiles are displayed in Table 4.4. For the traces corresponding to the same surcharge depth, and hence the same hydraulic condition, consistent parameter values should be expected if the ADE and ADZ models provide a robust description of the system (Stovin *et al.*, 2007). However, it is evident that both ADE and ADZ results show variations with the upstream concentration profile, with greater sensitivity being observed in the pre-threshold case. For example, for the pre-threshold traces, the ADE and ADZ travel times corresponding to the continuous injection are two times greater than those derived from the analysis of the instantaneous response; and the dispersion coefficient value is six times smaller. Note that the R_t^2 value for any of the data sets is not high, but poorer values have been observed for the pre-threshold traces.

		Upstream Conditions		
		Instantaneous	Gaussian	Step
	Pre-threshold			
ADE	Travel Time (s)	9.5021	16.7614	21.3722
	Dispersion Coefficient (m^2/s)	3.7054	1.0025	0.5659
	R_t^2 (-)	0.1733	0.3080	0.7359
ADZ	Travel Time (s)	21.4782	35.9346	51.5345
	Reach Time Delay (s)	7.5	5	-2
	R_t^2 (-)	0.3226	0.4763	0.8597
	Post-threshold			
ADE	Travel Time (s)	8.3075	8.4801	8.5601
	Dispersion Coefficient (m^2/s)	0.0082	0.0204	0.1848
	R_t^2 (-)	0.8191	0.8840	0.8515
ADZ	Travel Time (s)	9.9231	9.5325	10.8322
	Reach Time Delay (s)	7.5	6.75	4.25
	R_t^2 (-)	0.8317	0.9082	0.8601

Table 4.4 – Summary of the ADE and ADZ optimised results corresponding to three different upstream temporal concentration profiles for the CFD prototype models

(a) – Instantaneous injection

(d) – Instantaneous injection

(b) – Gaussian superposition

(e) – Gaussian superposition

(c) – Continuous injection superposition

(f) – Continuous injection superposition

Figure 4.27 – Synthesised responses to three different upstream temporal concentration profiles, compared with optimised ADE and ADZ predictions: (a-c) – Pre-threshold; (d-f) - Post-threshold

The sensitivity study confirms the findings of Stovin *et al*. (2007) that the inferred ADE and ADZ parameter values are sensitive to the shape and duration of the inlet profile. As a result, when the parameter values corresponding to one pair of profiles are utilised to predict the downstream concentration distribution for a different upstream profile, the prediction is poor and the goodness of fit decreases. Figure 4.28 shows the effects of using derived parameter values from the continuous upstream condition to route an instantaneous pulse; and the effect of the reverse process is shown in Figure 4.29. Comparing Figure 4.28 to Figure 4.27a, both the ADE and ADZ predictions in Figure 4.28 show a different peak arrival time and a peak with a

lower magnitude, which result in a larger deviation from the simulated profile and a decrease in the R_t^2 value. Comparison of Figure 4.29 and Figure 4.27c also suggests that the predictions made using the derived parameter values from a different pair of profiles are poor.
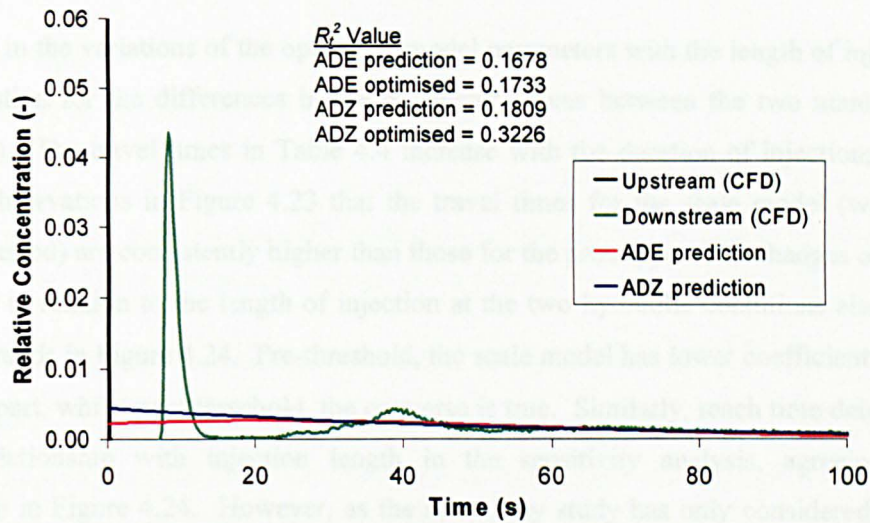
Figure 4.28 – Effect of routing upstream concentration distribution using the parameter sets derived from the continuous injection response
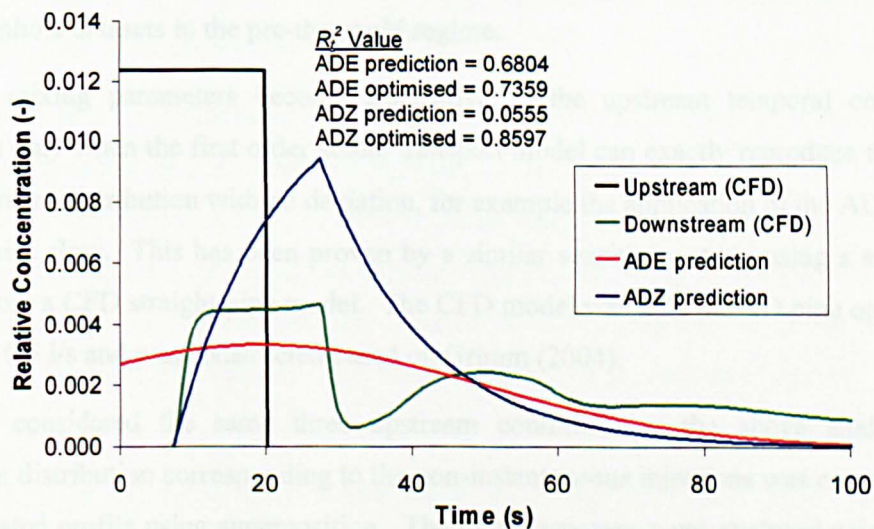
Figure 4.29 – Effect of routing upstream concentration distribution using the parameter sets derived from the instantaneous injection response

In modelling terms, the above results suggest that the parameters derived from a specific upstream profile may strictly only be applicable in situations where the upstream temporal concentration matches that for which they were originally derived (Stovin et al., 2007). The results also imply that the effects of a manhole's geometric scale on the mixing process cannot be studied via the comparisons of the optimised results (shown in Section 4.3.3) due to the

incomparable upstream conditions of the two experimental datasets. Further implication of the above study is that the first order ADE and ADZ models are inappropriate to be used for the description of the mixing characteristics in manholes or in hydraulic structures that these models cannot provide a full description of the mixing process.

The trends in the variations of the optimised model parameters with the length of injection offer an explanation for the differences in the parameter values between the two manhole models (Table 4.4). The travel times in Table 4.4 increase with the duration of injection; this agrees with the observations in Figure 4.23 that the travel times for the scale model (with a longer injection period) are consistently higher than those for the prototype. The changes of dispersion coefficient in relation to the length of injection at the two hydraulic conditions also match the observed trends in Figure 4.24. Pre-threshold, the scale model has lower coefficient values than its counterpart, whilst post-threshold, the converse is true. Similarly, reach time delay shows an inverse relationship with injection length in the sensitivity analysis, agreeing with the observation in Figure 4.24. However, as the sensitivity study has only considered two traces, one from pre-threshold and one from post-threshold, it is not possible to explain the difference in the relationship of the parameters and surcharge ratio between the two manhole datasets. For example, the different trends in the variations of reach time delay with surcharge ratio between the two manhole datasets in the pre-threshold regime.

Optimised mixing parameters become insensitive to the upstream temporal concentration distribution only when the first order solute transport model can exactly reproduce the shape of the downstream distribution with no deviation, for example the application of the ADE model in a straight pipe flow. This has been proven by a similar sensitivity study using a sample trace obtained from a CFD straight pipe model. The CFD model was a 24 mm ID pipe operating at a flowrate of 0.5 l/s and was constructed based on Grimm (2004).

The study considered the same three upstream conditions as the above analysis. The downstream distribution corresponding to the non-instantaneous injections was created from the CFD simulated profile using superposition. The three responses were analysed using the ADE model in association with the optimisation procedure. Table 4.5 shows the results of the optimised mixing parameters and the R_t^2 value for each of the predictions. It is evident that in the straight pipe study, the optimised parameter values show negligible variations with upstream condition. The difference between the optimised values appears to be less than 1 %. All predictions reveal a high R_t^2 value approaching 1.

	Upstream Conditions		
	Instantaneous	Gaussian	Step
ADE			
Travel Time (s)	0.6546	0.6574	0.6563
Dispersion Coefficient (m²/s)	0.0035	0.0034	0.0035
R_t^2	0.9995	1.0000	1.0000

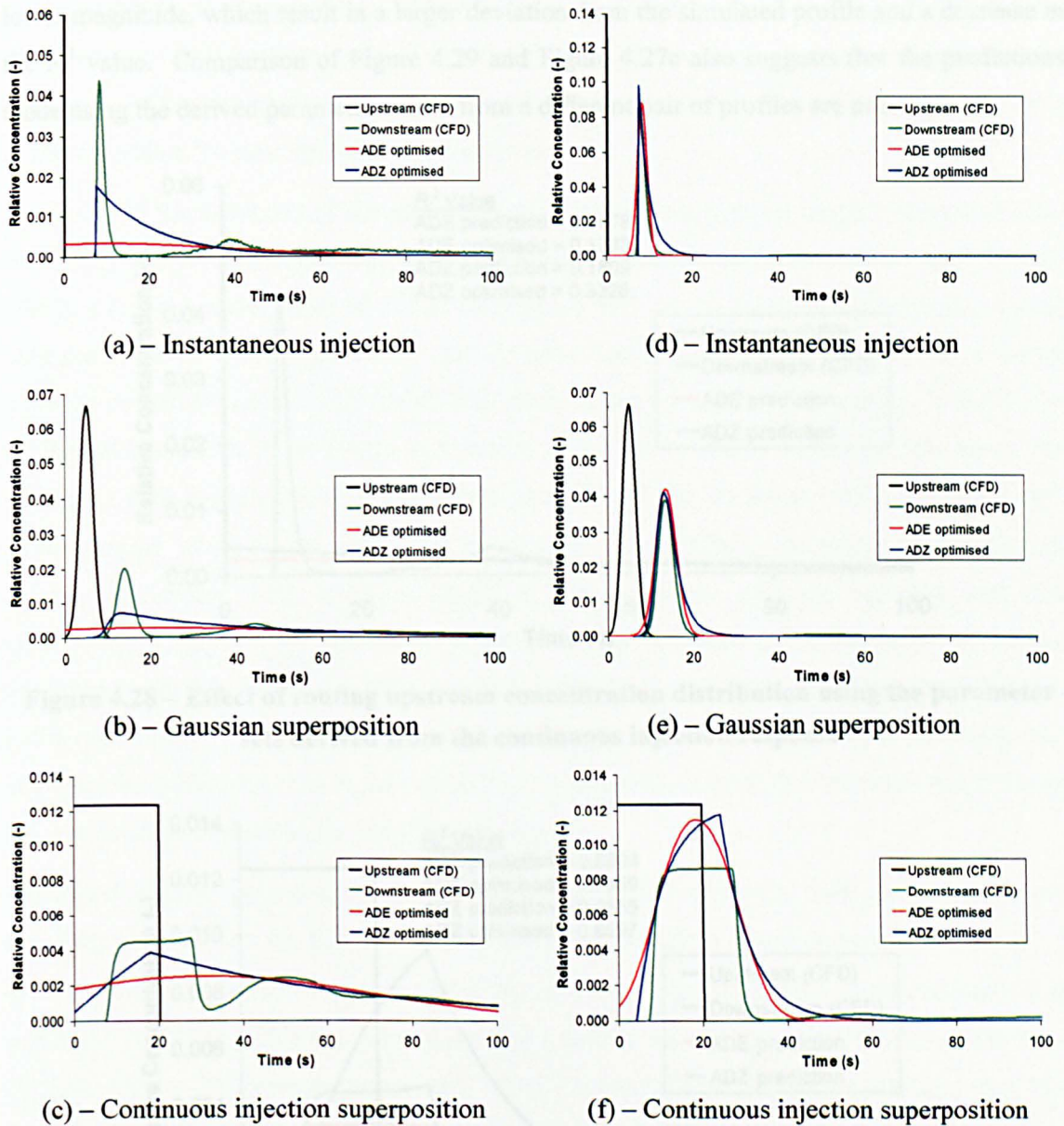**Table 4.5 – Summary of the ADE optimised results corresponding to three different upstream temporal concentration profiles in a straight pipe flow**

4.3.4.2 Meaning of Optimised Mixing Parameters

It is possible that the ADE and ADZ model parameters derived using the optimisation procedure represent the true physical characteristics, such as travel time and dispersion coefficient, of a flow system. This is true only when the solute transport model produces a prediction which exactly coincides with the reference downstream profile. When the prediction does not fit exactly, the best-fit parameter values should be regarded as *model coefficients* that produce the most-alike downstream profile to the reference downstream distribution, providing little information on the physical process.

Since the ADE and ADZ models are not able to describe the entire manhole mixing mechanism in either pre-threshold or post-threshold regimes, i.e. no occurrence where $R_t^2 = 1$, the derived parameters should be regarded as the best-fit *model coefficients* that correspond to the unique upstream conditions. If considering the optimised parameters as *model coefficients* that provide little information on the physical process, negative values in reach time delay obtained from the scale model (Figure 4.17) become acceptable; similarly, it is acceptable that the ADZ travel times for the manholes are consistently greater than the ADE travel times (Figure 4.23).

The difference in the travel time values predicted by the ADE and ADZ models can be explained by the different shapes of downstream distributions generated by the two models (Figure 4.5 and Figure 4.6). The first order ADE model which was originally developed for modelling straight pipe flows produced Gaussian shaped distributions according to the Gaussian upstream conditions, while the ADZ model generated skewed profiles from the Gaussian input which gave a better description of the manhole mixing in pre-threshold. Post-threshold, the ADE and ADZ optimised predictions were more comparable as both models generated Gaussian-like downstream distributions. Nevertheless, since the optimised ADE and ADZ predictions were of different shapes, the centroid position of the predicted profiles differed and

hence the mean travel time would vary. The ADZ travel times are greater than the ADE travel times because the profiles predicted by ADZ are skewed.

4.4 Comparison of the Surcharged Manholes' Tracer Profiles

The optimised travel time results presented in Figure 4.23 suggest that the scale model shows similar hydraulic characteristics to the prototype. The threshold depth occurs at a comparable surcharge ratio, confirming the validity of geometric scaling. However, the mixing characteristics, i.e. the degree and type of mixing, within the two manhole systems were not accurately described by the optimised mixing parameters. This is because the optimised parameters are model coefficients, i.e. providing partial or approximate information on the actual physical processes; and more importantly, they appear to be sensitive to the upstream temporal concentration distributions. The effects of scale on the solute transport characteristics cannot be studied via the comparisons of the optimised ADE and ADZ model parameters.

The fundamental mixing characteristics of a flow system can be revealed by recorded retention time distribution (RTD) and cumulative retention time distribution (CRTD) (Fogler, 1992; Levenspiel, 1972). This is because each form of mixing has its own characteristic shape of curve (Section 2.4.3 and Section 2.4.4.2.1). The present section aims to study the scalability of mixing between the two surcharged manhole, the 218 mm ID manhole and the prototype, using temporal concentration profile (TCP) and cumulative temporal concentration profile (CTCP). In theory, TCP and CTCP differ from RTD and CRTD because the TCP and CTCP are the response to a non-instantaneous upstream distribution, while RTD and CRTD correspond to an instantaneous pulse. Since the length of the upstream distributions in the two manhole studies is short, the TCPs in the two systems could be considered as RTDs and used as a tool to examine mixing characteristics. However, it should be borne in mind that the TCPs and CTCPs of the two manhole systems are not quantitatively comparable due to the different lengths of injection. Instantaneous injection is not physically feasible under laboratory conditions.

4.4.1 Comparison of Temporal Concentration Profiles

Figure 4.30 and Figure 4.31 present the comparisons of the downstream distributions in response to an upstream Gaussian temporal concentration distribution of the two differently sized models. The concentrations are normalised with respect to the peak concentration and the downstream temporal concentration distributions are plotted with respect to the first arrival time. The trends in the variations of downstream distribution shape as a function of surcharge appear to be highly comparable in both manhole models. Normalised with respect to the peak, the distributions show no noticeable difference in the rising limbs. The effects of surcharge on the

distributions become marked in the shape of the falling limb. In all distributions studied, the Gaussian-like profile distorts at some point and follows an approximately linear decay. The comparisons of the downstream distributions suggest that the types of mixing occurring in the two differently scaled manholes at similar surcharge ratios are identical. Note that the upstream concentration distributions for each of the manhole are highly comparable, with a standard deviation of less than 10 % of the mean for the centroid, standard deviation of the profile and maximum concentration (see Appendix A for the raw fluorometric data).
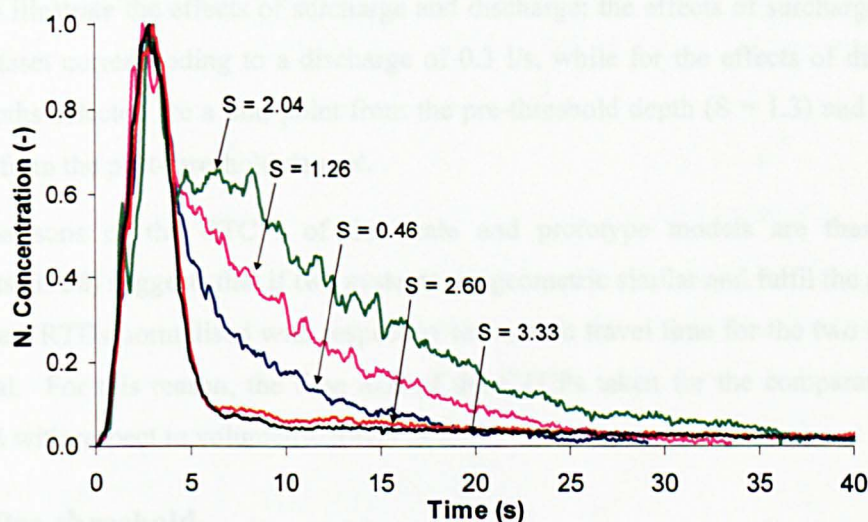

Figure 4.30 – Effects of variations in surcharge on downstream temporal concentration distributions: The scale model operated at 0.3 l/s
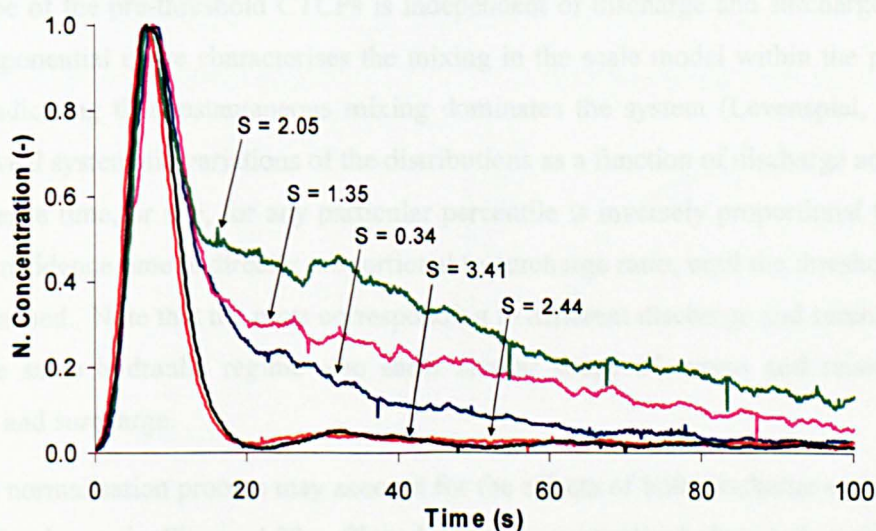

Figure 4.31 – Effects of variations in surcharge on downstream temporal concentration distributions: The prototype operated at 2 l/s (after Guymer *et al.*, 2005)

4.4.2 Comparison of Cumulative Temporal Concentration Profiles

This sub-section examines the effects of discharge and surcharge on solute transport within the scale manhole via the comparisons of cumulative temporal concentration profiles (CTCPs). The CTCPs are presented in a normalised form; the y-axis of the CTCPs are normalised with the total area of the corresponding upstream distribution; and the downstream temporal concentration distributions are plotted with respect to the first arrival time of the upstream concentration distribution. For presentation purposes, in each hydraulic regime, two sets of data are used to illustrate the effects of surcharge and discharge; the effects of surcharge are shown using a dataset corresponding to a discharge of 0.3 l/s, while for the effects of discharge, the sample depths selected are a mid-point from the pre-threshold depth (S = 1.3) and a mid-point (S = 3.33) from the post-threshold dataset.

The comparisons of the CTCPs of the scale and prototype models are then presented. Danckwerts (1958) suggests that if two systems are geometric similar and fulfil the principles of scaling, the CRTDs normalised with respect to volumetric travel time for the two systems will be identical. For this reason, the time axis of the CTCPs taken for the comparative study is normalised with respect to volumetric travel time.

4.4.2.1 Pre-threshold

The effects of discharge and surcharge on the CTCPs in the pre-threshold region are shown in Figure 4.32a and b respectively. Comparisons of the CTCPs in the two figures suggest that the basic shape of the pre-threshold CTCPs is independent of discharge and surcharge conditions. A near-exponential curve characterises the mixing in the scale model within the pre-threshold regime, indicating that instantaneous mixing dominates the system (Levenspiel, 1972). The figures reveal systematic variations of the distributions as a function of discharge and surcharge. The residence time, or age, for any particular percentile is inversely proportional to discharge; while the residence time is directly proportional to surcharge ratio, until the threshold surcharge level is reached. Note that the plots corresponding to different discharge and surcharge datasets within the same hydraulic regime also show similar shape of curves and relationship with discharge and surcharge.

Temporal normalisation process may account for the effects of both discharge and surcharge on the CTCPs shown in Figure 4.32. Plotted with the normalised time axis (with respect to volumetric travel time), the distributions tend to collapse onto a single curve, and no systematic variation arises as a function of discharge or surcharge (Figure 4.33).

Comparisons of the normalised pre-threshold CTCPs of the scale manhole and prototype suggest that the basic shape of the pre-threshold CTCP is independent of manhole scale. Instantaneous mixing dominates in the pre-threshold region for this manhole configuration (manhole ID to pipe ID ratio).

(a) - Discharge

(b) – Surcharge

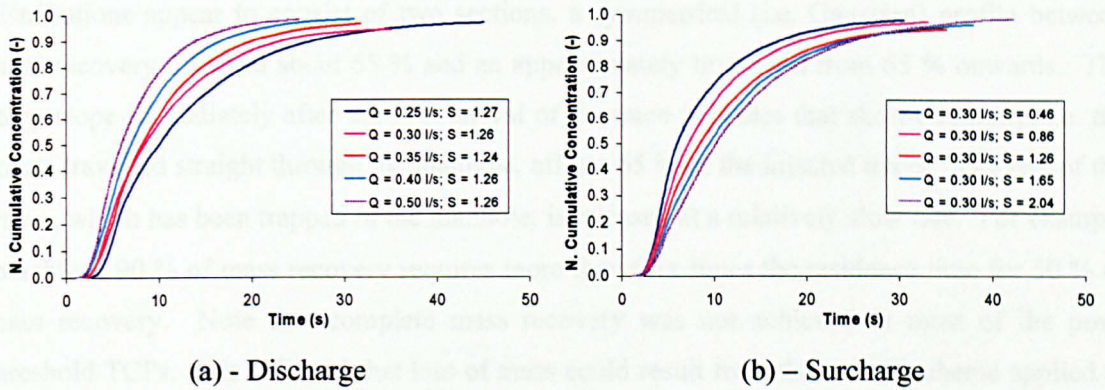**Figure 4.32 – Effects of discharge and surcharge on the cumulative temporal concentration profiles for the scale manhole in the pre-threshold regime**
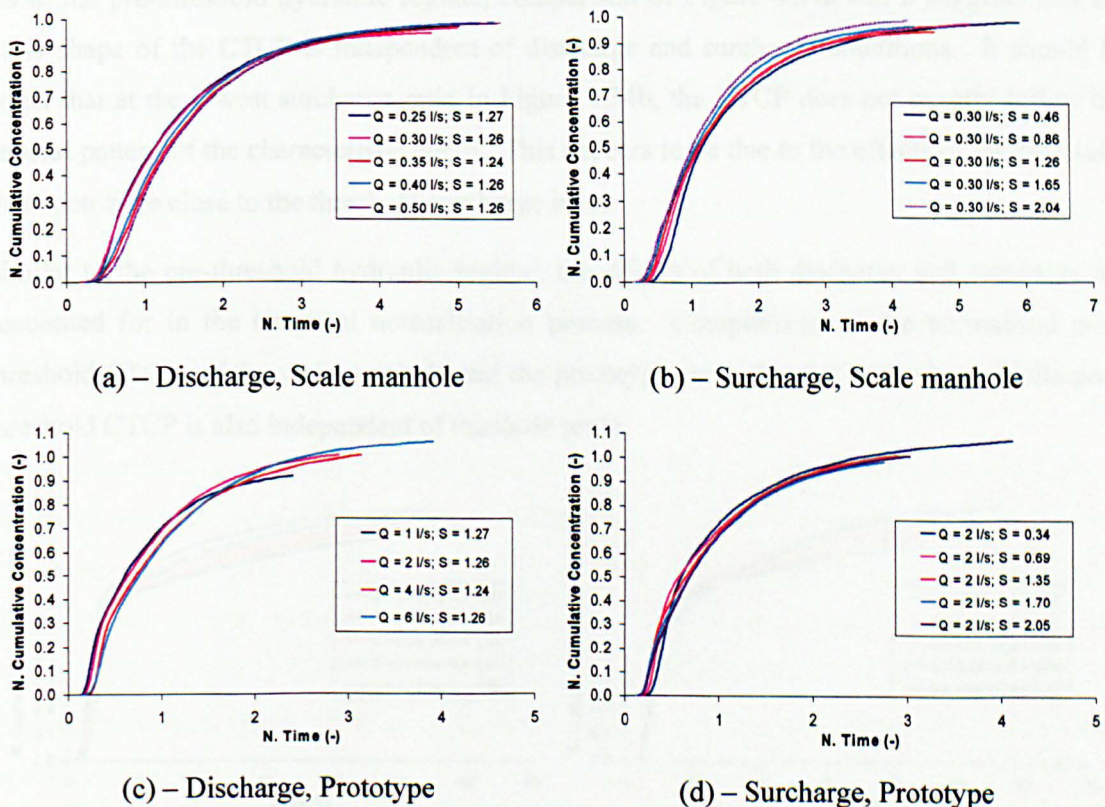

(a) – Discharge, Scale manhole

(b) – Surcharge, Scale manhole

(c) – Discharge, Prototype

(d) – Surcharge, Prototype

Figure 4.33 – Comparisons of pre-threshold cumulative temporal concentration profiles for the manholes

4.4.2.2 Post-threshold

The effects of discharge and surcharge on the CTCPs in the post-threshold region for the scale model are shown in Figure 4.34. Post-threshold, the downstream distributions reflect a different mixing mechanism than in the pre-threshold conditions. The cumulative concentration distributions appear to consist of two sections, a symmetrical (i.e. Gaussian) profile between mass recovery 0 % and about 65 % and an approximately linear tail from 65 % onwards. The steep slope immediately after the first arrival of the trace indicates that short-circuiting, i.e. the solute travelled straight through the manhole, affects 65 % of the injected tracer. The rest of the tracer, which has been trapped in the manhole, is released at a relatively slow rate. For example, to achieve 90 % of mass recovery requires more than four times the residence time for 50 % of mass recovery. Note that complete mass recovery was not achieved in most of the post-threshold TCPs. It is believed that loss of mass could result from the cut-off scheme applied to the profiles and, more probably, the instrument noise of the fluorometers at low concentrations (Section 3.4.2.2).

As in the pre-threshold hydraulic regime, comparison of Figure 4.34a and b suggests that the basic shape of the CTCP is independent of discharge and surcharge conditions. It should be noted that at the lowest surcharge ratio in Figure 4.34b, the CTCP does not exactly follow the general pattern of the characteristic curve. This appears to be due to the effects of the hydraulic transition zone close to the threshold surcharge level.

Similar to the pre-threshold hydraulic regime, the effects of both discharge and surcharge are accounted for in the temporal normalisation process. Comparisons of the normalised post-threshold CTCPs of the scale manhole and the prototype show that the basic shape of the post-threshold CTCP is also independent of manhole scale.

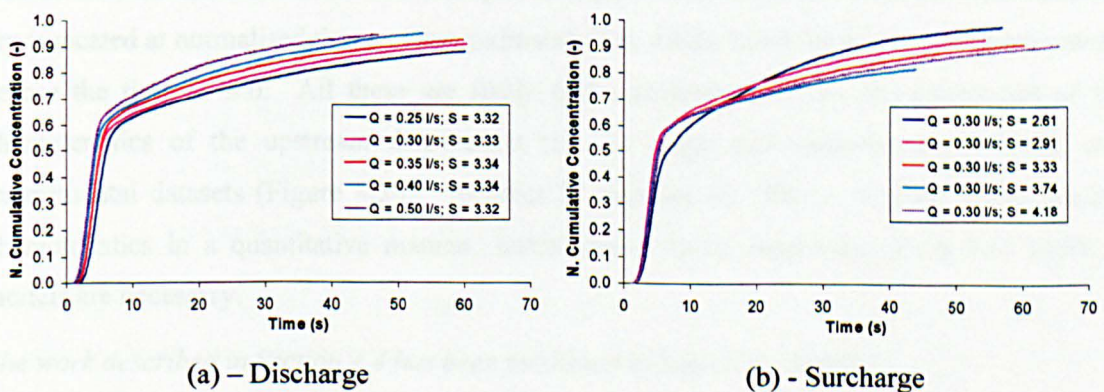(a) – Discharge   (b) - Surcharge

Figure 4.34 – Effects of discharge and surcharge on the cumulative temporal concentration distributions for the scale manhole in the post-threshold regime
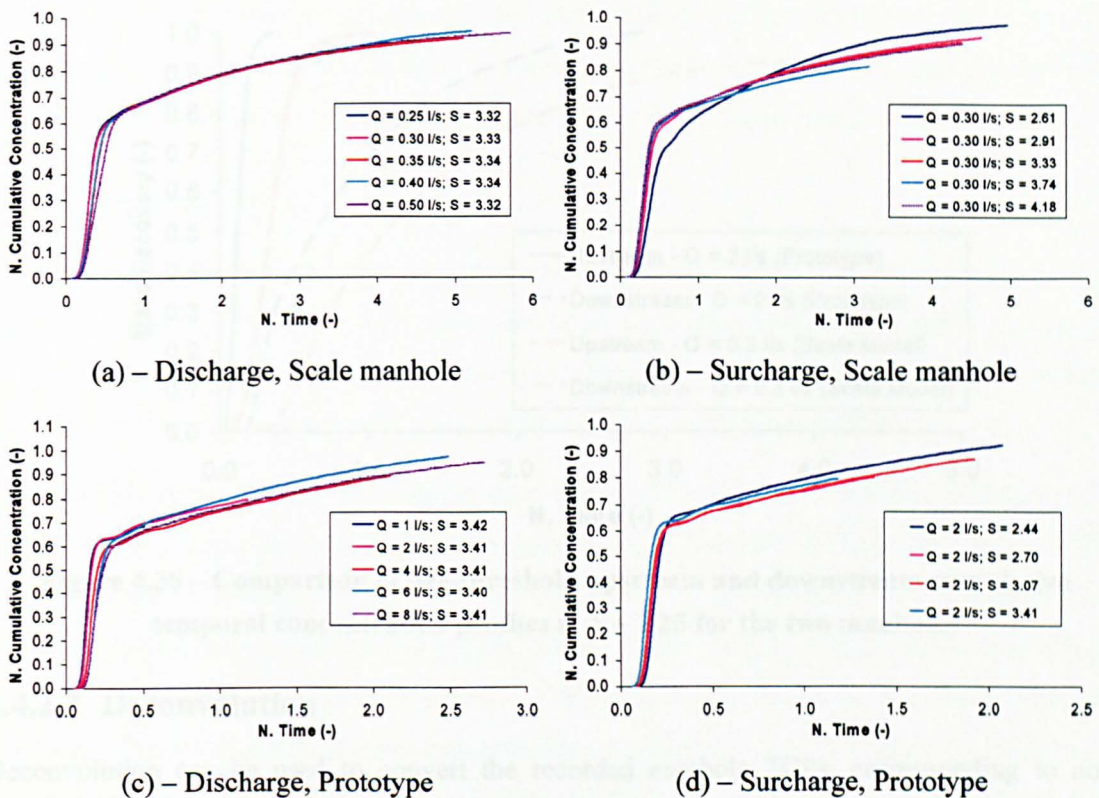
(a) – Discharge, Scale manhole

(b) – Surcharge, Scale manhole

(c) – Discharge, Prototype

(d) – Surcharge, Prototype

Figure 4.35 – Comparisons of post-threshold cumulative temporal concentration profiles for the manholes

The analysis presented above suggests that the solute transport characteristics of the surcharged manhole can be described in terms of just two CTCPs, one for each of the identified hydraulic regimes. However, careful examination of Figure 4.33 and Figure 4.35 shows that the curves obtained from the two different experimental scale models do not exactly coincide. In addition, the cut-off time of the prototype data, in terms of the normalised time, is consistently lower than that of the scale manhole data. For example, in Figure 4.35a the profiles for the scale manhole are truncated at normalised times of approximately 5.0; whilst those for the prototype are cut-off before the time of 3.0. All these are likely to be attributable to the inconsistencies of the characteristics of the upstream distribution (i.e. its shape and duration) between the two experimental datasets (Figure 4.36). In order to examine the effects of scale on the mixing characteristics in a quantitative manner, instantaneous tracer responses of the two manhole models are necessary.

The work described in Section 4.4 has been published in Lau et al. (2008).
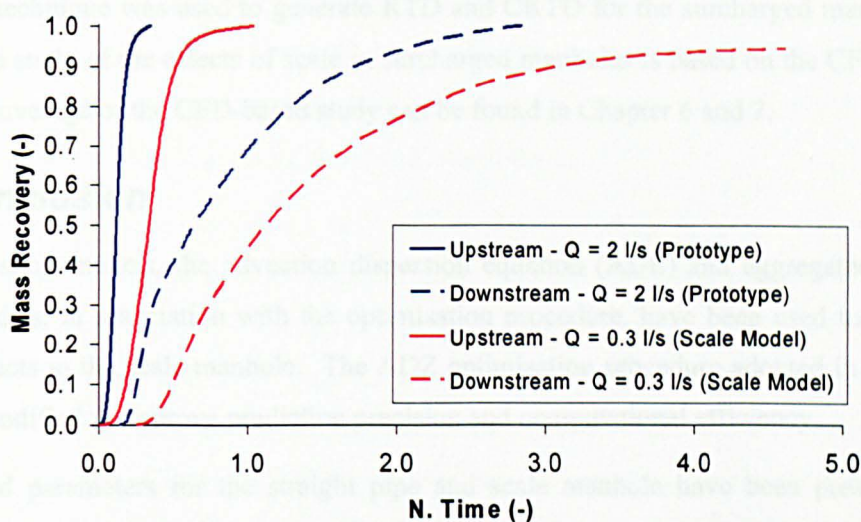
Figure 4.36 – Comparison of pre-threshold upstream and downstream cumulative temporal concentration profiles at $S \sim 1.25$ for the two manholes

4.4.2.3 Deconvolution

Deconvolution can be used to convert the recorded manhole TCPs, corresponding to non-instantaneous upstream profiles, to instantaneous responses. This technique works by reversing the effects of convolution, i.e. superposition, on recorded data. Mathematically, it is the reverse of Equation 4.10. For recorded data which contains noise, signal filtering process may be required in order to restore the original signals for the transfer function, $g(t)$, and the convoluted response, $h(t)$. The accuracy of the estimation of the original response, f, therefore depends upon the accuracy of the restoration of the original signals. Further details regarding deconvolution can be found in Wiener (1949).

$$f * g(t) = h(t) \hspace{5cm} 4.10$$

where:

f	is the original response, i.e. RTD
$g(t)$	is the transfer function, i.e. the upstream condition
$h(t)$	is the convoluted response, i.e. TCP

The deconvolution process was not applied to the experimentally measured manhole tracer data in order to derive their original response, RTD. This was mainly because this signal processing technique is not straightforward, particularly when the convoluted signals and the transfer function inherently contain noise. By comparison, CFD-generated data is readily produced in the form of an instantaneous response. A validated CFD model can produce a good representation of the measured tracer data (see Chapter 6). Therefore, this computational

modelling technique was used to generate RTD and CRTD for the surcharged manholes. The quantitative study of the effects of scale in surcharged manholes is based on the CFD generated profiles. Coverage of the CFD-based study can be found in Chapter 6 and 7.

4.5 Conclusion

Solute transport models, the advection dispersion equation (ADE) and aggregated dead zone (ADZ) models, in association with the optimisation procedure, have been used to analyse the mixing effects in the scale manhole. The ADZ optimisation procedure adopted in the analysis has been modified to improve prediction precision and computational efficiency.

The derived parameters for the straight pipe and scale manhole have been presented. The results for the straight pipe show reasonable agreement with theoretical data, such as travel time and dispersion coefficient. This provided confidence in the laboratory measurements and analytical approach to analysing tracer data. In the scale manhole data, a threshold surcharge level, at which the mixing parameters reveal a sharp transition, has been identified in the scale manhole. The level occurs at surcharge ratios between 2.0 and 2.5. Comparisons of the scale manhole data and the straight pipe results have been presented to highlight the effects of the scale manhole on solute transport characteristics.

Scalability of the laboratory derived manhole parameters has been investigated by comparing the non-dimensionalised optimised parameters of the scale manhole with the prototype. However, the comparisons show large discrepancies in the two experimental datasets. The reason for the discrepancies has been investigated and the investigation suggests that it is attributable to the difference in the injection duration between the upstream concentration distributions. The current study has also highlighted that ADE and ADZ derived parameters for the manholes are not scalable and the results presented can only be strictly applicable in situations where the upstream conditions match that for which the parameters were originally derived. The optimised coefficients do not represent the fundamental mixing characteristics in manholes as the solute transport models fail to exactly describe the manhole mixing in terms of a temporal concentration distribution. It is therefore suggested that the first order ADE and ADZ models are not appropriate to be used for the description of the mixing process in surcharge manholes and in other urban drainage structures that these model cannot provide a full description of the mixing process.

Temporal concentration profile (TCP) and cumulative temporal concentration profile (CTCP) have been considered as a tool to examine the effects of discharge and surcharge on manhole mixing. Two distinct CTCPs, one for each of the two hydraulic regimes, have been observed in the scale model. The pre-threshold CTCP can be characterised by a near-exponential curve.

The curve indicates that the flow under the pre-threshold conditions is dominated by instantaneous mixing; while post-threshold, the CTCP reflects a different mixing mechanism. The form of the curve suggests that the flow regime comprises a short-circuiting flow, affecting approximately 65 % of the incoming flow, and a dead zone.

Scale effects on solute travel time and mixing characteristics have been studied via the comparisons of CTCPs for the two different scaled models. The normalised CTCPs for each manhole collapse onto a single curve for each of the two hydraulic regimes. The normalised curves of the two differently sized manhole models also appear to be similar in terms of profile shape, which suggests that the solute transport characteristics of the surcharged manhole can be summarised in terms of just two CTCPs, one for each of the two identified hydraulic regimes. However, the CTCPs for the two manhole models cannot be used to quantify scale effects due to the influence of the upstream concentration distributions.

New concentration profiles corresponding to an instantaneous pulse for the two manhole models have been generated in computational fluid dynamics (CFD). These instantaneous responses have been used to study the scale effects on the solute transport characteristics in this manhole system (manhole ID to pipe ID ratio). Full details of the generation of the CFD models and the study of the effects of scale can be found in Chapter 6 and 7.

Chapter 5 describes the flow visualisation experiments undertaken in the scale manhole model using the laser induced fluorescence (LIF) and particle image velocimetry (PIV) techniques. The collected flow field results will be employed for the CFD manhole model validation. This is described in Chapter 6.